

All-in-one driver: What do groups 11 and 16 have in common?

by

Jiyoung Lee

A thesis submitted to the graduate faculty

in partial fulfillment of the requirements for the degree of

MASTER OF SCIENCE

Major: Physical Chemistry

Program of Study Committee:

Theresa L. Windus, Major Professor

Mark S. Gordon

James W. Evans

The student author, whose presentation of the scholarship herein was approved by the program of study committee, is solely responsible for the content of this thesis. The Graduate College will ensure this thesis is globally accessible and will not permit alterations after a degree is conferred.

Iowa State University

Ames, Iowa

2018

Copyright © Jiyoung Lee, 2018. All rights reserved.

TABLE OF CONTENTS

	Page
LIST OF FIGURES.....	v
LIST OF TABLES	viii
ACKNOWLEDGMENTS	x
ABSTRACT.....	xi
CHAPTER 1. INTRODUCTION	1
General Overview	1
Theory.....	4
Basis Set	8
References.....	11
CHAPTER 2. SIZE DEPENDENCE OF S-BONDING ON (111) FACETS OF CU NANOCLUSTERS	15
Abstract.....	15
1. Introduction.....	15
2. Computational Details: DFT Analysis via NWChem, GAMESS, and VASP	19
3. Results for Adsorption Energy and Bonding Characterization.....	21
3.1. Variation of Adsorption Energy with Cluster Size.	21
3.2. DOS, COHP, and MO Analysis.....	25
4. Relationship of the S Binding Energy and Shell-structure of Cu Clusters.....	27
5. Discussion and Conclusions	30
Acknowledgments.....	31
References.....	32
Appendix. Effects of Cluster Relaxation and Spin Polarization.....	36
CHAPTER 3. COMPARISON OF S-ADSORPTION ON (111) AND (100) FACETS OF CU NANOCLUSTERS	38
Abstract.....	38
1. Introduction.....	39
2. Computational Details	42
3. Analysis of S Adsorption on Isolated Clusters	43
3.1. Comparison of Different Methods and Functionals	43
3.2. Comparison of 3fh vs 4fh Adsorption Energy vs Cluster Size	45
3.3. Comparison of Bond Length for 3fh vs 4fh Adsorption Sites	49
4. Effects of Broadening the Occupancy Function	50
4.1. Adsorption Energy versus Cluster Size	51
4.2. Site-projected Density of States Analysis.....	52
5. Discussion and Conclusion	54
Acknowledgments.....	56
References.....	56

Appendix A. Modified Adsorption At and Near Steps	58
Appendix B. Dependence of The Adsorption Energy on The Slab Thickness.....	59
CHAPTER 4. STABILIZATION OF X–AU–X COMPLEXES ON THE AU(111) SURFACE: A THEORETICAL INVESTIGATION AND COMPARISON OF X = S, CL, CH ₃ S, AND SIH ₃ S	
S, CL, CH ₃ S, AND SIH ₃ S	62
Abstract.....	62
1. Introduction.....	63
2. Computational Details	64
2.1 Bulk and Surface.....	64
2.2. Gas Phase	67
3. Adsorption of S, Cl, CH ₃ S, and SiH ₃ S on Au(111)	69
3.1. S on Au(111).....	69
3.2. Cl on Au(111).	69
3.3. CH ₃ S on Au(111).	71
3.4. SiH ₃ S on Au(111).....	76
3.5. Effects of Functionals and Dispersion Interactions.....	76
4. AuX ₂ Complexes in The Gas Phase	82
4.1. AuS ₂	83
4.2. AuCl ₂	83
4.3. Au(CH ₃ S) ₂	83
4.4. Au(SiH ₃ S) ₂	84
4.5. Summary	84
5. Discussion	84
Acknowledgments.....	87
References.....	87
CHAPTER 5. STABILITY OF M ₃ S ₃ COMPLEXES ON FCC M(111) SURFACES: M = AU, AG, CU, AND NI.....	
M = AU, AG, CU, AND NI.....	94
Abstract.....	94
1. Introduction.....	95
2. Methodology	99
3. Criteria for Stability of Adsorbed M ₃ S ₃ Complexes	101
4. Results for Energetics of M ₃ S ₃ Complexes.....	104
4.1. Gas-phase Complexes.....	104
4.2. Adsorbed Complexes.....	106
4.3. Analysis of Energetics within the Framework of Hess’s Law	109
5. Discussion and Conclusions	111
Acknowledgments.....	113
References.....	114
CHAPTER 6. QUANTUM CHEMISTRY COMMON DRIVER AND DATABASES (QCDB): NWCHEM INTERFACE	
CHAPTER 6. QUANTUM CHEMISTRY COMMON DRIVER AND DATABASES (QCDB): NWCHEM INTERFACE	118
Abstract.....	118
1. Introduction.....	118
2. NWChem Interface.....	120

2.1. Molecules	121
2.2. Basis Sets	123
2.4. Tasks	126
2.5. Additional Functionalities	127
3. Conclusion	129
Acknowledgements	130
References	130
Appendix A. Interface to NWChem	131
A.1. Installation	131
1) PSI4	131
2) NWChem	131
A.2. NWChem for PSI4 Users	132
A.3. PSI4 for NWChem Users	132
A.4. Basic Rules for NWChem Values	133
1) Array type	133
2) String type, True/False	134
A.5. Capabilities	134
1) Tensor contraction engine (TCE) module	134
A.6. List of Available PSI Variables for NWChem Interface	137
Appendix B. Keywords	139
B.1. Compatible Pure PSI4 Keywords	139
1) Molecule keywords	139
2) Basis set keywords	139
3) Map of DFT functionals	140
B.2. NWChem Input Keywords for the NWChem Interface	140
1) NWChem internal	142
2) SCF Keywords	143
3) DFT Keywords	145
4) MP2 Keywords	147
5) CCSD Keywords	148
6) TCE (Tensor contraction engine) keyword: CI, MBPT, and CC	148
7) TDDFT Keywords	150
8) TASK keywords	151
CHAPTER 7. CONCLUSION	152

LIST OF FIGURES

	Page	
Figure 2.1	Top panels: Various classes of tetrahedral (T_d) clusters. (a) Perfect tetrahedron (class m0), (b) tetrahedron with the bottom apex atom removed (class m1), (c) with all four apex atoms removed (class m4), and (d) with four atoms from each vertex removed (class m16). Bottom panels: clusters with octahedral (O_h) symmetry: (e) perfect octahedron (class Om0), (f) octahedron with the apex atom from each vertex removed (class Om6), and (g) four atoms from each vertex removed (class Om30).....	22
Figure 2.2	Plane-wave DFT results for the adsorption energy of S on Cu clusters on the fcc site closest to the center of a cluster of various sizes and shapes. Lines with various colors connects clusters of various classes shown in Figure 2.1.	23
Figure 2.3	Comparison of the size dependence of E_b on 3fh sites on the m0 clusters calculated using different methods.	24
Figure 2.4	Adsorption energy of S on octahedral Cu clusters on the fcc site closest to the center of a cluster of various sizes and shapes. Lines with various colors connects clusters of various classes shown in Figure 2.1.....	25
Figure 2.5	Site projected density of states (SDOS) of the S on various clusters and a slab.	26
Figure 2.6	COHP of S with the three closest Cu atoms on tetrahedral clusters of various sizes, and on a five layer slab in a (3×3) supercell.....	27
Figure 2.7	Molecular orbitals (MOs) that contribute the most to interactions between S and Cu on Cu_{10} clusters, using GAMESS and MacMolPlt. The energies of MOs relative to the HOMO energy are indicated below the orbitals.....	28
Figure 2.8	(a) $E_b(\text{S})$ (in eV) for S on various adsorption sites of the tetrahedral Cu_{20} cluster. (b) HOMO and LUMO of the clean Cu_{20} cluster, with a S on the fcc and hcp site near the center.....	30
Figure 2.9	Comparison of the size dependence of E_b on fcc sites on the m0 tetrahedral clusters with different assumptions using plane-wave basis sets. Results with fixed substrate and no spin polarization are represented by diamonds, fixed substrate, and with spin polarization are	

	represented by triangles, relaxed substrate with no spin polarization by pluses, and relaxed substrate with spin polarization by asterisks.....	36
Figure 3.1	Adsorption energy of S on 3fh and 4fh sites, with fixed and fully relaxed substrates. The insets show S adsorbed on a 3fh site of an 84-atoms T_d cluster, and a 4fh site of a 91-atom $Oh2$ cluster, with full geometric relaxation. Note the more significant relaxation of the $Oh2$ cluster. The longer horizontal lines show the values of E_b averaging over results for the larger clusters. The shorter horizontal lines represent results obtained from slab calculations. See text for more details. Data for 3fh sites are taken from Ref. 17.....	44
Figure 3.2	Average bond length of S on 3fh and 4fh sites, with fixed and fully relaxed substrates.....	49
Figure 3.3	The adsorption energy E_b as a function of the cluster size, with Gaussian smearing of the occupancy function with widths 0.5 eV and 1.0 eV. The two short horizontal lines represent the corresponding slab geometry calculation results, with frozen substrates.....	52
Figure 3.4	Effects of smearing widths on SDOS for an S atom on a 4fh site in a $Oh2$ cluster with 91 Cu atoms. Here the energies are shown relative to the Fermi energy, in contrast to Fig. 3.5.....	54
Figure 3.5	Site-projected density of states (SDOS) of a S atom on a 3fh site of a T_d cluster with 56 Cu atoms (solid line), and a S atom on a 4fh site of a $Oh2$ cluster with 91 atoms (dashed line). Gaussian smearing of width 1.0 eV is used. Energy is relative to individual atoms, rather than the Fermi energies, which are plotted as two distinct vertical lines. There are two broad peaks for bonding orbitals, from the sulfur s and p electrons respectively.....	55
Figure 3.6	Adsorption energy E_b for S at step edges. The pluses (connected by a black line) are for steps right on the edge, and the asterisks (connected by a red line) are for steps receded from the edge by one row of atoms.....	59
Figure 4.1	Stability as measured by the chemical potential of S of various structures on Au(111) versus the baseline. The black solid line is the baseline energetics of chemisorbed S forming triangular arrays. Representatives of the $\sqrt{3}$ -row (blue line), $\sqrt{7}$ -row (green line), and AuS_2 complexes (red line) are given as insets.....	71
Figure 4.2	Stability as measured by the chemical potential of Cl of various structure on Au(111) versus the baseline, which consists of	

	chemisorbed Cl at 2/3, 1/3, 2/9, and 1/12 ML for this plot (although only two data points are visible). Notations of other structures are similar to those in Figure 4.1.....	71
Figure 4.3	Stability as measured by the chemical potential of CH ₃ S of various structures on Au(111) versus the baseline.	72
Figure 4.4	Energetics of various proposed RS–Au–SR structures at 1/3 ML for CH ₃ S on Au(111). Energetics (in eV) is defined in <i>eq (2)</i> and results are from PBE calculations, averaging over slab thickness <i>L</i> from 4 to 7. <i>k</i> -point grids are (8×14) for (a) and (b), (8×7) for (c), and (6 × 8) for (d). The numbers in parentheses denote the numerical uncertainties of the last digit obtained from the standard deviations of the data of different <i>L</i> divided by 4, the number of samples.....	76
Figure 4.5	Energetics of various proposed RS–Au–SR structures at 1/3 ML for CH ₃ S on Au(111). Energetics (in eV) is defined in <i>eq (2)</i> and results are from PBE calculations, averaging over slab thickness <i>L</i> from 4 to 7. <i>k</i> -point grids are (8×14) for (a) and (b), (8×7) for (c), and (6 × 8) for (d). The numbers in parentheses denote the numerical uncertainties of the last digit obtained from the standard deviations of the data of different <i>L</i> divided by 4, the number of samples.....	77
Figure 4.6	Various metastable, near linear X–Au–X complexes on Au(111), with all configurations obtained from PBE calculations in (3 × 3) supercells with five layer slabs.	79
Figure 5.1	Schematics of the most stable M ₃ S ₃ configuration on the M(111) surface for M = Au, Ag, Cu, and Ni.	97
Figure 6.1	Schematic diagram of quantum chemistry common driver and databases (QCDB).	120
Figure 6.2	Schematic diagram of NWChem and GAMESS interfaces in PSI4.....	120

LIST OF TABLES

	Page
Table 3.1	Adsorption energy E_b (eV) of S on clusters of different shapes and sizes. PAW potentials and plane-wave basis set with energy cutoff of 280 eV are used for VASP. For NWChem, the superscripts a and b denote combinations of LANL2DZ/6-311++G(d,p) and def2-QZVP/def2-QZVPPD for Cu/S, respectively. Geometries of all clusters are from the VASP/PBE optimized structure.....45
Table 3.2	Adsorption energy E_b , average value $\langle E_b \rangle$, and standard deviation δE_b (in eV) for S on Cu(100) and Cu(111) with different slab thicknesses L , all with (2×2) supercells and $(24 \times 24 \times 1)$ k -point grid..... 61
Table 4.1	Chemical potential (eV) for RS–Au–SR complexes with different spacing d along the stripe direction, calculated using PBE and the optB88-vdW functional ^a 73
Table 4.2	Chemical potential (eV) for RS–Au–SR complexes with different spacing d along the stripe direction, calculated using PBE and the optB88-vdW functional ^a 81
Table 4.3	Stability of AuX ₂ complexes and properties of Bulk Au (cohesive energy E_c and lattice constant a_0) with different functionals ^a 82
Table 4.4	Binding energy (eV) of Au–X (X = S, Cl, CH ₃ S, and SiH ₃ S) complexes in the gas phase ^a 85
Table 5.1	Atomization energy $E_{at}(\text{gas})$ of M ₃ S ₃ complexes in the gas phase in eV. ... 105
Table 5.2	Total M-S binding energy $E_{MS}(\text{gas})$ of M-S complex in the gphase in eV..... 106
Table 5.3	Formation energy, $E_{form}(\text{ads})$, and binding energy, $E_{bind}(\text{ads})$, for the adsorbed complex from PBE in eV. 107
Table 5.4	Adsorption energies $E_{ad}(\text{S})$ and $E_{ad}(\text{M}_3\text{S}_3)$ in eV from PBE in both cases with $\theta_S = 3/16$ ML..... 110
Table 5.5	Decomposition of $E_{form}(\text{ads})$ corresponding to Hess’s law using PBE energies in eV..... 110
Table 6.1	List of available methods for energy, gradient, and geometry optimization..... 135

Table 6.2	List of compatible pure PSI4 keywords in the NWChem interface.	140
Table 6.3	List of available DFT functionals through PSI4 keywords.....	141

ACKNOWLEDGMENTS

This work was supported by the U.S. Department of Energy (DOE), Office of Science, Basic Energy Sciences, Chemical Sciences, Geosciences, and Biosciences Division at the Ames Laboratory under contract number DE-AC02-07CH11358. Ames Laboratory is operated for the DOE by Iowa State University. The document number assigned to this thesis is IS-T 3243.

ABSTRACT

This thesis is divided into two parts. The first part describes a theoretical study on the interaction between Group 11 metals and adsorbates (mainly sulfur), accompanied phenomena such as site preference of sulfur adsorbates, and formation of metal-adsorbate complexes using density functional theory (DFT). The second part describes a program development called the quantum chemistry common driver and databases (QCDB), which contributes to the improvement of interoperability for quantum chemistry software.

Site preference of S adsorption on the Cu surfaces. Binding energies of S adsorbed at four-fold-hollow (4fh) sites (provided by Cu(100)) and three-fold-hollow (3fh) sites (provided by Cu(111)) were calculated using Gaussian and plane wave basis sets and compared. From the results, a strong cluster size dependence of S adsorption was observed, especially with relatively small Cu(111) clusters (~300 Cu atoms), which reflects a quantum size effect. Similarly, Cu(100) also shows the size dependence with the smaller clusters, but the site preference of S to 4fh sites over 3fh sites of ~0.6 eV appeared when the number of Cu atoms is more than 280. This energetic preference to 4fh sites was supported by analysis using site projected density of states (DOS) and molecular orbitals (MOs) that show both sites have similar bonding interactions, but the 4fh sites have weaker antibonding interactions.

Formation of AuX₂ (X=S, Cl, CH₃S, SiH₃S) complexes on Au(111) surface. The stabilities of AuX₂ complexes in both gas-phase and adsorbed on the Au(111) surface were investigated using Gaussian and plane wave basis sets. Gaussian basis set results calculated using DFT and coupled-cluster (CC) theory show that the AuX₂ gas-

phase complexes have similar bond strengths regardless of X, while plane wave surface absorption results show that AuS₂ is unstable, AuCl₂ is stable or unstable depending on the functional, and Au(CH₃S)₂ and Au(SiH₃S)₂ are stable on the surface. This is consistent with the experimental observations that AuS₂ cannot be observed while AuCl₂ can be observed sometimes with high coverage of X, and Au(CH₃S)₂ and Au(SiH₃S)₂ are observed even with low coverage of X. This suggests that the interaction between the complex and surface (ligand adsorption energy) is more important than the interaction within the complex (Au-X binding energy) to determine the stability and formation of AuX₂ complex on the Au(111) surface.

Formation of M₃S₃ complexes. Both energetics of the gas-phase M₃S₃ and the adsorbed on metal surfaces are reported and analyzed using Hess's Law. The study of M₃S₃ (M=Ni, Cu, Ag, Au) on metal surfaces (presented in Chapter 5) shows a great agreement between Gaussian and plane-wave basis sets and successfully explains observations (obtained by Scanning Tunneling Microscopy (STM)) of M₃S₃ complexes on the M(111) surface with the reasons why it can be formed under certain experimental conditions. The significant result found in this study is that only Ag has a different behavior than other metals, the formation of Ag₃S₃ is a spontaneous process where excess S that exists at the terrace and metals from kink sites along step edges are extracted.

Quantum Chemistry Common Driver and DataBases (QCDB). Descriptions of the QCDB program are provided including Appendices that give additional details of the program. In this thesis, the focus is on the NWChem interface in PSI4, but the common interface and the fundamental goal of this project are also discussed with the potential applications and future work. The NWChem, GAMESS, and CFOUR interfaces

are successfully built in PSI4 so users now can share their input keywords with PSI4 and easily compare the computed results through the NWChem interface. Currently, QCDB is being separated out from PSI4 and contains the CFOUR, PSI4 and NWChem interface.

CHAPTER 1. INTRODUCTION

General Overview

There is significant interest in phenomena induced by the interaction between non-metal adsorbates and metal surfaces, surface reconstruction, site preference, and formation of certain metal-adsorbate complexes.^{1,2} There are many different combinations of adsorbates and metals, but the current research is mainly focused on chalcogen and group 11 metal surfaces which are known for catalytic ability and many other applications, such as heterogeneous catalysis, surface Raman spectroscopy, and so on.³ This research is a collaboration with Dr. Da-Jiang Liu, Dr. Jeffery S. Boschen, Prof. Patricia A. Thiel, Prof. James W. Evans, and Prof. Theresa L. Windus and was motivated by observations from scanning tunneling microscopy (STM). Specifically, Dr. Da-Jiang Liu and I have performed computations to theoretically interpret various experimental results in the following four studies.

1. Site preference of sulfur (S) adsorption on coinage Cu clusters (tetrahedral (T_d) exposed (111) facets and octahedral (O_h) exposed (100) facets)
2. Stability of AuX_2 complexes ($X = S, Cl, CH_3S, SiH_3S$) on Au(111) surface
3. Stability of M_3S_3 complexes on face centered cubic (fcc) $M(111)$ surfaces ($M = Ni, Cu, Ag, Au$)

The first topic was motivated by the observation that adsorbed S induced reconstruction of the Cu(111) surface, which provides three-fold-hollow (3fh) sites, to end up with S placed on four-fold-hollow (4fh) reconstructed Cu(100) sites.^{4,5} For the theoretical investigations, density functional theory (DFT) was used with two different types of basis sets, plane wave basis sets and Gaussian basis sets, to examine the S adsorbed on Cu(100)

and Cu(111) surfaces. Chapters 2 and 3 present the results of this study. First, a size dependence of S-binding is found up to sizes ~ 300 for Cu(111) nanoclusters. Second, both smaller Cu(100) and Cu(111) nanoclusters show strong variation in energetic site preference, but the 4fh site is preferred over the 3fh site for bigger clusters (above ~ 280 Cu atoms). A great agreement between Gaussian basis set and plane wave basis set is also achieved in this research.

In Chapter 4, the results on stability of AuX_2 complexes on the Au(111) surface are described. According to experimental observations when CH_3S , Cl, or S gas is released on a Au(111) surface, the $\text{Au}(\text{CH}_3\text{S})_2$ complex is formed on the surface even at low coverage of adsorbates,⁶ AuCl_2 sometimes formed at high coverage,⁷ but AuS_2 is not formed at all.⁸ Questioning why the stability of AuX_2 ($\text{X}=\text{S}$, Cl, CH_3S) complexes placed on the surface are so different, the stability of the gas-phase AuX_2 complexes and the complexes on the surface was investigated. Additionally the SiH_3S ligand was also included to understand if electronegativity played a role. As a result, it is found that the bond strength of Au-X is similar in gas-phase regardless of X, while the stability of the complexes is different when they are adsorbed on the surface. The complex adsorbed on the surface with S is less stable than individually chemisorbed S, Cl is either less or more stable depending on DFT functional, and CH_3S and SiH_3S are more stable.

Another interesting metal-chalcogen complex formed on surfaces is $M_3\text{S}_3$ where $M=\text{Ni}$, Cu, Ag, and Au. This research was inspired by STM observations of Ni_3S_3 on Ni(111),⁹ Au_3S_3 on Au(111),¹⁰ and Cu_3S_3 on Cu(111).¹¹ For this topic, computations on $M_3\text{S}_3$ in gas-phase and adsorbed on the surface were performed and the energetic contributions on formation of $M_3\text{S}_3$ on the surface were explained using Hess's law. Chapter 5 provides

results suggesting why certain M_3S_3 clusters can be identified under the conditions (temperature, coverage, etc.) of the reported experiments.

Chapter 6 presents a different topic from the previous research and is related to developing a program called the quantum chemistry common driver and databases (QCDB). QCDB is a common driver that contains built-in interfaces for quantum chemistry programs and allows users to drive computations of any program using a common input. In addition, codes in different programs can interoperate through the driver. For example, users can execute PSI4¹² for geometry optimization but using a theory in a different software package to evaluate the energies and gradients and use analysis existing in another software.

The original idea was started from Prof. David Sherrill and his students by building a CFOUR interface in PSI4.¹³ As the first idea has been successfully tested, the idea was developed to gain more general interoperability between programs, not just limited to CFOUR. To do that, two strategies are taken. First, develop the existing PSI4 driver that already has the CFOUR interface by building interfaces with other programs, particularly NWChem¹⁴ and GAMESS.^{15,16} Then, generalize the driver interfaced with other programs to be applicable for any quantum chemistry program and separate the interface from PSI4 to obtain the QCDB.

To complete the first strategy, NWChem and GAMESS (implemented by Dr. Nuwan De Silva) were interfaced with the PSI4 driver. The overall structure of interfaces is similar to CFOUR (*Figure 6.2.* shows the schematic diagram of this). In Chapter 6, the detail of the NWChem interface is discussed describing how the interface works and also possible potential research and plans for the future.

Theory

Density functional theory (DFT) has been one of the popular computational chemistry methods because of its ability to achieve a good estimation on chemical systems compared to required computational expense. The following description of the theory is a summary, please refer to reference 17 for more detail. Hohenberg and Kohn demonstrated that the molecular energy and molecular properties of non-degenerate ground states can be determined by the electron probability density, ρ , in many electron systems.^{17,18} The Hohenberg and Kohn theorem describes the ground-state molecular energy (E_0), an eigenvalue of the purely electronic Hamiltonian, as the sum of kinetic and potential energies,

$$E_0 = T[\rho] + V_{eN}[\rho] + V_{ee}[\rho] \quad (1)$$

where $T[\rho]$ is the kinetic-energy, $V_{eN}[\rho]$ is the electron-nuclear attraction, and $V_{ee}[\rho]$ is the electron-electron repulsion. The theorem was further developed in the Kohn-Sham method¹⁹⁻²¹ that computes the kinetic energy of the density, an unknown functional (a function of a function) that has to be approximated. The Kohn-Sham kinetic energy ($T_s[\rho]$) can be calculated by the following equations,

$$T_s[\rho] = \sum_{i=1}^N \left\langle \phi_i \left| -\frac{1}{2} \nabla^2 \right| \phi_i \right\rangle \quad (2)$$

where s denotes the reference system of non-interacting N electrons, and ϕ_i is a wave function of electron i . The electron probability density of an atom that has N electrons, $\rho(r)$, is

$$\rho(r) = \sum_{i=1}^N |\phi_i(r)|^2 \quad (3)$$

where r is the distance between an electron i and nuclei, and $|\phi_i(r)|^2$ is the probability of a wave function of electron i . From the Kohn-Sham theorem, each term of equation (1) can be rewritten as follows.

$$T[\rho] = \Delta T[\rho] + T_s[\rho] \quad (4)$$

$$V_{eN}[\rho] = \int \rho(r)v(r)dr \quad (5)$$

$$V_{ee}[\rho] = \Delta V_{ee}[\rho] + \frac{1}{2} \iint \frac{\rho(r_1)\rho(r_2)}{r_{12}} dr_1 dr_2 \quad (6)$$

where $\Delta T[\rho]$ is the difference between the kinetic energy ($T[\rho]$) and the non-interacting kinetic energy ($T_s[\rho]$), and $v(r)$ is the external potential, produced by charges of ‘external’ nuclei, acting on the electrons. The term ‘external’ is defined by the Born-Oppenheimer approximation²¹ where the nuclei are considered fixed objects external to the system of electrons. So the total energy $E[\rho]$ is

$$E[\rho] = \Delta T[\rho] + T_s[\rho] + \int \rho(r)v(r)dr + \Delta V_{ee}[\rho] + \frac{1}{2} \iint \frac{\rho(r_1)\rho(r_2)}{r_{12}} dr_1 dr_2 \quad (7)$$

In equation (7), the two functionals $\Delta T[\rho]$ and $\Delta V_{ee}[\rho]$ are unknown and whose sum is usually defined as an exchange-correlation energy $E_{xc}[\rho]$ in DFT.

Depending on what exchange-correlation approximation is used, DFT functionals can be divided into five types⁵⁴; the local-density approximation (LDA),^{22,23} local spin density approximation (LSDA)^{22,23} generalized-gradient approximation (GGA),²⁴⁻²⁶ meta-GGA,⁴⁹⁻⁵² and hybrid.²⁷ LDA is an approximation that a functional only depends on the electron density at each point in space. LSDA is an extended approximation of LDA to spin-polarized system.

The forms of E_{xc}^{LDA} and E_{xc}^{LSDA} are

$$E_{xc}^{LDA} = \int dr \rho(r)\epsilon_{xc}(\rho) \quad (8)$$

$$E_{xc}^{LSDA}[\rho_{\uparrow}, \rho_{\downarrow}] = \int dr \rho(r)\epsilon_{xc}(\rho_{\uparrow}(r), \rho_{\downarrow}(r)) \quad (9)$$

where ϵ_{xc} is the exchange-correlation energy per electron and $\rho_{\uparrow}, \rho_{\downarrow}$ are spin densities. While E_{xc}^{LDA} and E_{xc}^{LSDA} is a function of ρ and assumes the electron density is almost the same everywhere, the GGA splits E_{xc} into exchange and correlation and includes a gradient of the

density.⁵⁴ Meta-GGA includes orbital kinetic energy density additionally to GGA so their forms of E_{xc} are

$$E_{xc}^{GGA}[\rho_{\uparrow}, \rho_{\downarrow}] = \int dr \rho(r) \varepsilon_{xc}^{GGA}(\rho_{\uparrow}(r), \rho_{\downarrow}(r), \nabla\rho_{\uparrow}(r), \nabla\rho_{\downarrow}(r)) \quad (10)$$

$$E_{xc}^{MGGA}[\rho_{\uparrow}, \rho_{\downarrow}] = \int dr \rho(r) \varepsilon_{xc}^{MGGA}(\rho_{\uparrow}(r), \rho_{\downarrow}(r), \nabla\rho_{\uparrow}(r), \nabla\rho_{\downarrow}(r), \tau_{\uparrow}, \tau_{\downarrow}) \quad (11)$$

$\nabla\rho_{\uparrow}(r), \nabla\rho_{\downarrow}(r)$ stand for gradients of ρ and $\tau_{\uparrow}, \tau_{\downarrow}$ stand for kinetic energy densities. The hybrid functional is an approximation that includes a portion of the exact exchange (E_x^{exact}) from Hartree-Fock (HF) theory, which can improve calculation of properties such as atomization energy, bond length and vibrational frequencies.²⁸ The form is

$$E_{xc}^{hybrid} = E_{xc}^{GGA} + a(E_x^{exact} - E_x^{GGA}) \quad (12)$$

For more detail, please check reference 54.

Since the systems treated in this thesis include transition metals, which can cause expensive computations, DFT is an appropriate method to reduce the computational expense but also to achieve a good quality of accuracy for single reference systems. The functionals used the most in this study are Perdew-Burke-Ernzerhof (PBE)²⁹ and PBE0,³⁰ a hybrid function mixing PBE and HF exchange in a 3 to 1 ratio. Results provided in this thesis show that the PBE functional succeeded in explaining the experimental observations and questions that we had.

Nonetheless, one of the disadvantages of DFT is that it is not systematically improvable. Therefore, one cannot insist on what functional gives the right answer unless benchmark data is available. To cover this issue, coupled-cluster singles and doubles with perturbative triples (CCSD(T)) is extensively used, specifically in Chapter 4, to benchmark results on gas-phase complexes. CCSD(T) is a theory used widely among the many coupled-cluster (CC) methods available because the theory achieves as high accuracy as CCSDT in

many chemical systems, but is computationally less expensive.⁴³ The CC method was introduced by Coester and Kümmel to describe a system that has interactions between particles.¹⁷ The wave function of the CC method is expressed as

$$\psi = e^{\hat{T}} \Phi_0 \quad (13)$$

where ψ is the exact wave function, \hat{T} is the cluster operator, and Φ_0 is the normalized wave function. The cluster operator is the sum of n-particle excitation operators (\hat{T}_1 , \hat{T}_2 , etc) and the exponential operator $e^{\hat{T}}$ is represented as a form of Taylor-series expansion:

$$e^{\hat{T}} = 1 + \hat{T} + \frac{\hat{T}^2}{2!} + \frac{\hat{T}^3}{3!} + \dots \quad (14)$$

The name of the CC method is defined depending on the level of many particle excitation operators are considered. In other words, the cluster operator for the CCSD is

$$\hat{T} = \hat{T}_1 + \hat{T}_2 \quad (15)$$

$$\hat{T}_1 \Phi_0 = \sum_{a=n+1}^{\infty} \sum_{i=1}^n t_i^a \Phi_i^a \quad (16)$$

$$\hat{T}_2 \Phi_0 = \sum_{b=a+1}^{\infty} \sum_{a=n+1}^{\infty} \sum_{j=i+1}^n \sum_{i=1}^{n-1} t_{ij}^{ab} \Phi_{ij}^{ab} \quad (17)$$

where \hat{T}_1 is one-particle excitation operator, \hat{T}_2 is two-particle excitation operator, Φ_i^a is a singly excited Slater determinant, t_i^a is a numerical coefficient that depends on i and a , and Φ_{ij}^{ab} is a doubly excited Slater determinant, t_{ij}^{ab} is a numerical coefficient that depends on i , j and a , b where i and j are occupied spin-orbitals and a and b are unoccupied spin-orbitals. CCSD(T) includes triple excitations additionally calculated by perturbation theory. Details on the theory can be found in reference 44.

To benchmark data, results computed by CCSD(T) with large basis sets (commonly aug-cc-pVNZ basis set where N is D (double), T (triple), Q (quadruple), etc.) were

extrapolated to the complete-basis-set (CBS).⁴⁵ The CBS formula of Halkier et al.³¹ used in the benchmarking can be found in the Computational details of Chapter 4.

Basis Set

A basis set is one of the choices necessary to start a calculation. It is composed of atomic basis functions χ_r which represent electronic wave functions expressing molecular orbitals (MOs) $\phi_i = \sum_i c_{ri}\chi_r$.⁴⁶ To find a relevant basis set for the system that one is interested is challenging as one needs to balance the computational expense and a good estimation of the properties of interest for the system. This section outlines basic information about atomic basis sets.

The Slater-type orbitals (STOs) whose linear combination expresses each atomic orbital (AO) of a molecule are of the form

$$\chi_{nlm}(\zeta, r, \theta, \varphi) = NY_l^m(\theta, \varphi)r^{n-1}e^{-\zeta r} \quad (18)$$

In equation 18, n , l , m stand for the standard quantum numbers, N is a normalization constant, ζ is an orbital exponent, r is a distance between nuclei and an electron, and $Y_l^m(\theta, \varphi)$ are spherical harmonic functions.⁴⁶ The disadvantage of this type of basis set is that it is time consuming to calculate properties for a molecule with more than three or four atoms since it requires the solution of three or four-centered integrals. To fix the problem, Boys³² proposed to use Gaussian-type functions (GTFs), which uses the Gaussian product theorem. Using this approach, three or four-centered integrals can be reduced to one or two centered which improves the speed of calculations. The linear combination of such GTFs is called Gaussian-type orbitals (GTOs).⁴⁶ The form of GTOs is

$$g_{nlm}(\zeta, r, \theta, \varphi) = NY_l^m(\theta, \varphi)r^{2n-2-l}e^{-\zeta r^2} \quad (19)$$

The Gaussian function does not have a cusp at the origin, so it can fail to describe behaviors near the nucleus or properties that depend more on the non-valence regions. GTOs are also poor at describing long-range behaviors (multipole moments, polarizability, etc.)⁵³ because the function diminishes too quickly.¹⁷ In spite of these disadvantages, the GTO basis set is widely used in computational chemistry because it reduces computer time much more than Slater-type functions.

Such STO and GTO basis sets have one basis function on each atomic orbital, the so-called minimal basis set. If a basis set has two basis functions per atomic orbital, it is called a double-zeta (*DZ*) basis set. There are triple-zeta (*TZ*), quadrupole-zeta (*QZ*), and so on depending on the number of basis functions for each atomic orbital. Instead of applying this approach for all atomic orbitals, a split-valence basis set is a basis set where multiple basis functions are used for the valence orbitals, while core orbitals use only one basis function.⁴⁸ The Pople notation for this basis set is *X*-*YZG* (or *X*-*YZWG*, *X*-*YZWVG*, etc.) where *X* is the number of primitive Gaussians of each core atomic orbitals, and *Y* and *Z* are the number of Gaussians of valence orbitals split into two parts. For example, 6-31G means 6 Gaussians are used to represent core atomic orbitals and 3 and 1 Gaussians to represent valence orbitals split into two parts.

Depending on the system, one can also add polarization and diffuse functions. The polarization basis function is to consider the polarized effects (where atomic orbitals want to shift to be more directional) from the other basis function.⁴⁷ For example, a polarized basis function for a basis set with the highest angular momentum of a *p* orbital is expressed by a basis function of a *d* orbital. This basis function is generally denoted as * or P (e.g., 6-31G* meaning addition of a polarization function to 6-31G basis set, *DZP* addition of a

polarization function to a *DZ* basis set). The diffuse function is an extended Gaussian function with small exponent to consider when the wavefunction requires the extra spatial extent. This basis function is needed for molecules such as anions and molecules with lone pair electrons. It is denoted as + or D (e.g., 6-31+G* meaning addition of a diffuse function to 6-31G*, *DZPPD* meaning addition of a diffuse and two polarization basis function to a *DZ* basis set). For more details, check references 46-48.

Since the molecular systems in this thesis include transition metals (Ni, Cu, Ag, and Au), the basis sets need to have a good balance between the computational expense and accuracy. Given that situation, the reasonable basis sets for metals are those that include effective core potentials (ECP). ECP is considered to be useful for a large system to reduce the computational expense by replacing the core electrons with a calculated potential.^{33,34} Since the potential is also calculated considering relativistic effects if they exist, the accuracy, specifically for transition metal systems, would not be reduced either. From this perspective, the selected basis set for metals in this thesis is (LANL2DZ)³⁵⁻³⁷ and for sulfur is 6-311++G(d,p).³⁸⁻⁴⁰ This basis set combination has turned out to be very useful to start calculations (such as finding minima geometries) because it does not request too much computational expense even with large transition metal systems, but is large enough to get the general picture of energetics of the system.

Nevertheless, the basis set combination was not enough to achieve the accuracy that the studies were aiming for, so much larger basis sets needed to be used, def2-*NZVP* for metals⁴¹ and def2-*NZVPPD* ($N=D,T$) for other non-metal atoms.⁴² Both are split-valence type basis sets and P and D (not *D of N*) denotes a set of polarization and diffusion functions, respectively. Using the def2 basis sets with DFT calculations is known to give better results

than using ECP and is recommended for transition-containing systems.³⁴ The basis sets also provide all electron basis sets for *3d* transition metals (such as Cu, Ni) and ECP portion (much smaller than LANL2DZ ECP) to *4d* and *5d* metals (such as Ag, Au) that have strong relativistic effects. Using the larger basis sets, a great agreement was achieved with the results of plane wave basis sets.

References

1. Walen, H.; Liu, D.-J.; Oh, J.; Yang, H. J.; Kim, Y.; Thiel, P. A. *Physical Chemistry Chemical Physics* **2016**, *18* (6), 4891–4901.
2. Walen, H.; Liu, D.-J.; Oh, J.; Lim, H.; Evans, J. W.; Aikens, C. M.; Kim, Y.; Thiel, P. A. *Physical Review B* **2015**, *91* (4).
3. Shen, M.; Liu, D.-J.; Jenks, C. J.; Thiel, P. A. *The Journal of Physical Chemistry C* **2008**, *112*(11), 4281–4290.
4. Foss, M.; Feidenhans'l, R.; Nielsen, M.; Findeisen, E.; Buslaps, T.; Johnson, R.; Besenbacher, F. *Surface Science* **1997**, *388* (1-3), 5–14.
5. Ruan, L.; Stensgaard, I.; Besenbacher, F.; Lægsgaard, E. *Ultramicroscopy* **1992**, 42-44, 498–504.
6. Voznyy, O.; Dubowski, J. J.; Yates, J. T.; Maksymovych, P. *Journal of the American Chemical Society* **2009**, *131* (36), 12989–12993.
7. Zheltov, V. V.; Cherkez, V. V.; Andryushechkin, B. V.; Zhidomirov, G. M.; Kierren, B.; Fagot-Revurat, Y.; Malterre, D.; Eltsov, K. N. *Physical Review B* **2014**, *89* (19).
8. Walen, H.; Liu, D.-J.; Oh, J.; Lim, H.; Evans, J. W.; Kim, Y.; Thiel, P. A. *The Journal of Chemical Physics* **2015**, *143* (1), 014704.
9. Yamada, M.; Hirashima, H.; Kitada, A.; Izumi, K.-I.; Nakamura, J. *Surface Science* **2008**, *602*(9), 1659–1668.
10. Kurokawa, S.; Miyawaki, Y.; Sakai, A. *Japanese Journal of Applied Physics* **2009**, *48* (8).
11. Wahlström, E.; Ekvall, I.; Kihlgren, T.; Olin, H.; Lindgren, S.-Å.; Walldén, L. *Physical Review B* **2001**, *64* (15).

12. Turney, J. M.; Simmonett, A. C.; Parrish, R. M.; Hohenstein, E. G.; Evangelista, F. A.; Fermann, J. T.; Mintz, B. J.; Burns, L. A.; Wilke, J. J.; Abrams, M. L.; Russ, N. J.; Leininger, M. L.; Janssen, C. L.; Seidl, E. T.; Allen, W. D.; Schaefer, H. F.; King, R. A.; Valeev, E. F.; Sherrill, C. D.; Crawford, T. D. *Wiley Interdisciplinary Reviews: Computational Molecular Science* **2011**, 2 (4), 556–565.
13. Parrish, R. M.; Burns, L. A.; Smith, D. G. A.; Simmonett, A. C.; DePrince, A. E.; Hohenstein, E. G.; Bozkaya, U.; Sokolov, A. Y.; Remigio, R. D.; Richard, R. M.; Gonthier, J. F.; James, A. M.; McAlexander, H. R.; Kumar, A.; Saitow, M.; Wang, X.; Pritchard, B. P.; Verma, P.; Schaefer, H. F.; Patkowski, K.; King, R. A.; Valeev, E. F.; Evangelista, F. A.; Turney, J. M.; Crawford, T. D.; Sherrill, C. D. *Journal of Chemical Theory and Computation* **2017**, 13 (7), 3185–3197.
14. Kendall, R. A.; Aprà, E.; Bernholdt, D. E.; Bylaska, E. J.; Dupuis, M.; Fann, G. I.; Harrison, R. J.; Ju, J.; Nichols, J. A.; Nieplocha, J.; Straatsma, T.; Windus, T. L.; Wong, A. T. *Computer Physics Communications* **2000**, 128 (1-2), 260–283.
15. Schmidt, M. W.; Baldrige, K. K.; Boatz, J. A.; Elbert, S. T.; Gordon, M. S.; Jensen, J. H.; Koseki, S.; Matsunaga, N.; Nguyen, K. A.; Su, S.; Windus, T. L.; Dupuis, M.; Montgomery, J. A. *Journal of Computational Chemistry* **1993**, 14 (11), 1347–1363.
16. Gordon, M. S.; Schmidt, M. W. *Theory and Applications of Computational Chemistry* **2005**, 1167–1189, Ch. 41, C. E. Dykstra, G. Frenking, K.S. Kim, G.E. Scuseria, Eds., Elsevier, **2005**.
17. Levine, I. N. *Quantum chemistry*; Pearson Prentice Hall: Upper Saddle River, NJ, 2009.
18. Hohenberg, P.; Kohn, W. *Physical Review* **1964**, 136 (3B).
19. Kohn, W.; Sham, L. J. *Physical Review* **1965**, 140 (4A).
20. Dreizler, R. M.; Gross, E. K. *Density functional theory: an approach to the quantum many body problem*; Springer: Berlin, 1995.
21. Born, M.; Oppenheimer, R. *Annalen der Physik* **1927**, 389 (20), 457–484.
22. Parr, R. G.; Yang, W. *Density-functional theory of atoms and molecules*; Oxford University Press: N.Y., 1989.
23. Dirac, P. A. M. *Mathematical Proceedings of the Cambridge Philosophical Society* **1930**, 26 (03), 376.
24. Perdew, J. P.; Chevary, J. A.; Vosko, S. H.; Jackson, K. A.; Pederson, M. R.; Singh, D. J.; Fiolhais, C. *Physical Review B* **1992**, 46 (11), 6671.
25. Becke, A. D. *Physical Review A* 1988, 38 (6), 3098.

26. Langreth, D. C.; Mehl, M. J. *Physical Review B* **1983**, 28 (4), 1809.
27. Becke, A. D. *The Journal of Chemical Physics* **1993**, 98 (2), 1372.
28. Perdew, J. P.; Ernzerhof, M.; Burke, K. *The Journal of Chemical Physics* **1996**, 105 (22), 9982.
29. Perdew, J. P.; Burke, K.; Ernzerhof, M. *Physical Review Letters* **1997**, 78 (7), 1396.
30. Adamo, C.; Barone, V. *The Journal of Chemical Physics* **1999**, 110 (13), 6158.
31. Halkier, A.; Helgaker, T.; Jørgensen, P.; Klopper, W.; Koch, H.; Olsen, J.; Wilson, A. K. Basis-Set convergence in correlated calculations on Ne, N₂, and H₂O. *Chem. Phys. Lett.* **1998**, 286, 243– 252.
32. Boys, S. F. *Proceedings of the Royal Society A: Mathematical, Physical and Engineering Sciences* **1950**, 200 (1063), 542.
33. Niu, S.; Hall, M. B. *Chemical Review*. **2000**, 100, 353
34. Xu, X.; Truhlar, D. G. *Journal of Chemical Theory and Computation* **2011**, 8 (1), 80.
35. Hay, P. J.; Wadt, W. R. *The Journal of Chemical Physics* **1985**, 82 (1), 270.
36. Wadt, W. R.; Hay, P. J. *The Journal of Chemical Physics* **1985**, 82 (1), 284.
37. Hay, P. J.; Wadt, W. R. *The Journal of Chemical Physics* **1985**, 82 (1), 270.
38. Mclean, A. D.; Chandler, G. S. *The Journal of Chemical Physics* **1980**, 72 (10), 5639.
39. Krishnan, R.; Binkley, J. S.; Seeger, R.; Pople, J. A. *The Journal of Chemical Physics* **1980**, 72(1), 650.
40. Clark, T.; Chandrasekhar, J.; Spitznagel, G. N. W.; Schleyer, P. V. R. *Journal of Computational Chemistry* **1983**, 4 (3), 294.
41. Weigend, F.; Ahlrichs, R. *Physical Chemistry Chemical Physics* **2005**, 7 (18), 3297.
42. Rappoport, D.; Furche, F. *The Journal of Chemical Physics* **2010**, 133 (13), 134105
43. Scuseria, G. E.; Lee, T. J. *The Journal of Chemical Physics* **1990**, 93 (8), 5851–5855.
44. Crawford, T. D.; Schaefer, H. F. *Reviews in Computational Chemistry* **2007**, 33–136.
45. Petersson, G. A.; Bennett, A.; Tensfeldt, T. G.; Al-Laham, M. A.; Shirley, W. A.; Mantzaris, J. *ChemInform* **1988**, 19 (45).

46. Hehre, W. J.; Stewart, R. F.; Pople, J. A. *The Journal of Chemical Physics* **1969**, *51* (6), 2657–2664.
47. Raffenetti, R. C. *The Journal of Chemical Physics* **1973**, *58* (10), 4452–4458.
48. Ditchfield, R.; Hehre, W. J.; Pople, J. A. *The Journal of Chemical Physics* **1971**, *54* (2), 724–728.
49. Kurth, S.; Perdew, J. P.; Blaha, P. *International Journal of Quantum Chemistry* **1999**, *75* (4-5), 889.
50. Perdew, J. P.; Kurth, S.; Zupan Aleš; Blaha, P. *Physical Review Letters* **1999**, *82* (25), 5179–5179.
51. Voorhis, T. V.; Scuseria, G. E. *The Journal of Chemical Physics* **1998**, *109* (2), 400–410.
52. Tao, J.; Perdew, J. P.; Staroverov, V. N.; Scuseria, G. E. *Physical Review Letters* **2003**, *91* (14)
53. Koga, T.; Thakkar, A. J. *Canadian Journal of Chemistry* **1992**, *70* (2), 362–365.
54. Perdew, J. P. *AIP Conference Proceedings* **2001**.

CHAPTER 2. SIZE DEPENDENCE OF S-BONDING ON (111) FACETS OF CU NANOCCLUSERS

A paper published in and reprinted with permission from

The Journal of Physical Chemistry C **2016**, *120(19)*, 10268-10274

Jeffery S. Boschen,^{a,b} Jiyoung Lee,^{a,b} Theresa L. Windus,^{a,b} James W. Evans,^{a,c} and Da-Jiang Liu^{a,*}

^a*Ames Laboratory – USDOE, Iowa State University, Ames, IA 50011, USA*

^b*Department of Chemistry, Iowa State University, Ames, IA 50011, USA*

^c*Department of Physics and Astronomy, Iowa State University, Ames, IA 50011, USA*

**Corresponding author*

Abstract

We demonstrate a strong damped oscillatory size dependence of the adsorption energy for sulfur on the (111) facets of tetrahedral Cu nanoclusters up to sizes of ~300 atoms. This behavior reflects quantum size effects. Consistent results are obtained from density functional theory analyses utilizing either atomic orbital or plane-wave bases and using the same Perdew–Burke–Ernzerhof functional. Behavior is interpreted via molecular orbitals (MO), density of states (DOS), and crystal orbital Hamilton population (COHP) analyses.

1. Introduction

There exist extensive analyses of the size dependence of adsorption properties for CO and other species on selected subsequences of metal nanoclusters.^{1,2} A particular advantage of studies for finite clusters with small to medium sizes is that there is considerable flexibility in available electronic structure methods: from density functional theory (DFT) analysis with atomic orbital basis expansions, plane-wave basis sets, or real- space grid methods,¹⁻³ to higher-level quantum chemistry methods.⁴ These cluster studies are often focused on

extrapolation of behavior determined from precise calculations for smaller sizes [of $n = O(10^1)$ to $O(10^2)$ atoms], not just to the larger-size regime common for supported catalytic nanoparticles [with $n = O(10^2)$ to $O(10^4)$], but beyond to the limit corresponding to extended surfaces [with $n \rightarrow \infty$]. This goal has prompted interest in identifying simple scaling rules for the variation of intrinsic properties, $A(n)$, in the larger size regime. These sometimes have the form $A(n) \approx A(\infty) + cn^{-1/3}$ based on surface area versus volume contributions and associated thermodynamic considerations.¹ However, more complex behavior might be anticipated in some systems even for sizes up to $n = O(10^2)$.^{2,5}

Various adsorbate-cluster systems have been studied previously, including: CO adsorption on (111) facets of Pd^{1,6-8} and Pt,^{1,9,10} O adsorption on (111) facets of Pt,¹¹ CO and O adsorption on (111) facets of Au^{2,5,12} and Pt,³ CO adsorption on (111) facets of Cu,⁴ and S adsorption on various facets of Ni.¹³ These studies often choose sequences of octahedral or cuboctahedral clusters. Our focus in this work is on S adsorption on (111) facets of Cu, motivated in part by recent experiments for S/Cu(111).¹⁴⁻¹⁷ These experiments are in turn motivated by the potential for S to induce surface reconstruction and to form metal–S complexes, which can facilitate rearrangement or destabilization of metal nanostructures by providing alternative mass transport pathways.^{15,17} (As an aside, interest exists in the interaction of sulfur and organosulfur with coinage metals more generally. In addition to reconstruction, complexation, and destabilization, which occur also for Ag and Au,¹⁸⁻²² S can act as a promoter or poison in catalysis,²³ and the S–metal bond also plays a key role in anchoring various molecular ligands particularly on Au(111) surfaces.^{24,25}) In our study, we focus on characterization of S adsorption for sequences of tetrahedral (T_d) Cu clusters with exposed (111) facets, for which one might anticipate rapid convergence in adsorption

behavior to that for extended Cu(111) surfaces, if interactions between the adsorbate and the metal surface are short-ranged.

The majority of DFT studies of adsorption on clusters have utilized localized orbital-based DFT,^{1,6,7,9-11,13} but some have instead used plane-wave DFT with periodic boundary conditions (with one cluster-plus-adsorbate system included in each unit cell).¹² The former has a potential advantage in providing and elucidating a localized orbital based picture of bonding. In this work, we will implement and compare both approaches utilizing the same Perdew–Burke–Ernzerhof (PBE) functional.²⁶ Our results for adsorption energies from both approaches are quite consistent with each other. There are complications for either method with respect to extrapolation of behavior to infinite cluster size, as discussed below. However, this limiting behavior can be accessed independently within the plane-wave DFT approach from calculations using slab rather than cluster geometries for increasing lateral unit cell sizes and appropriately averaging over slab thicknesses to eliminate quantum size effects (see below).²⁷

A key observation of our analysis is a particularly strong size dependence of the adsorption energy of S on the (111) facets of tetrahedral Cu clusters. Specifically, we find a nonmonotonic damped oscillatory variation, which dominates over any $n^{-1/3}$ type scaling behavior, at least for sizes up to $n \approx 300$ atoms. For metal thin films and other nanostructures, it has long been recognized that effectively constraining nearly free electrons in a finite nanoscale region introduces large variations in energies and other properties.²⁸⁻³¹ The effect is quantum in nature and thus is commonly referred to as quantum size effects (QSE). Associated behavior cannot be described by any simple scaling rule, but it can be effectively captured even in free electron models and jellium models. As an aside, although the strong

size dependence due to QSE complicates extrapolation of energetics for bulk systems, it may open possibilities for tuning catalytic and other properties of nanoclusters. Indeed, QSE-modified adsorption properties² and catalytic properties³² of metal nanoclusters have been observed in previous studies.

Another component of our study is to provide chemical insight into the binding strength and variation of S on the Cu nanoclusters. For DFT analysis based on localized orbital basis expansions, one can extract and identify molecular orbitals (MOs) characterizing bonding for smaller Cu clusters, but not necessarily for larger clusters. For plane-wave based DFT, this type of interpretation is not straightforward. However, using crystal orbital Hamilton population (COHP) analysis,³³ we are able to identify both bonding and antibonding MOs from such plane-wave based analyses. There is no one-to-one correspondence between the MOs from finite cluster calculations versus slab geometry calculations. However, by combining several MOs from the cluster calculations for medium to large clusters, a correspondence can be established. This indicates that although the convergence in energetics is slow, a qualitative picture that describes bonding of S and the Cu(111) surface emerges even for relatively small clusters.

We also find that the T_d Cu₂₀, which corresponds to a electronic closed-shell “magic” cluster,³⁴ is generally not favorable for S adsorption. Furthermore, the differences in adsorption energies on different sites are particularly pronounced and have a high correlation with the shapes of the highest occupied MO (HOMO) and lowest unoccupied MO (LUMO).

The paper is organized as follows. In Section 2, computational details are described for DFT calculations using both an atomic basis set (NWChem³⁵ and GAMESS^{36,37}) and a plane-wave basis set (VASP^{38,39}). In Section 3, basic results for the S adsorption energy

versus Cu cluster size are presented for two types of 3-fold hollow (3fh) sites on (111) facets. With regard to cluster geometry, we focus on the Cu(111) surface and consider various truncations of tetrahedral clusters. Results for S adsorption on octahedral clusters are also given. A comparison of energies from different DFT methods and functionals is provided for selected cases. In addition, the site projected density of states (SDOS) of the adsorbed S and crystal orbital Hamilton population (COHP) analysis of its interactions with the Cu cluster are given in Section 3.2. The mechanism of the size dependence is analyzed in Section 4. Further discussion and conclusions are given in Section 5.

2. Computational Details: DFT Analysis via NWChem, GAMESS, and VASP

Plane-wave DFT calculations are performed using the VASP code^{38,39} (version 5.3.5) with the projector augmented-wave (PAW)^{40,41} method. The energy cutoff for plane-wave basis set is 280 eV. For cluster calculations, Gaussian smearing with $\sigma = 0.2$ eV is used as the default. For periodic slab calculations, the Methfessel–Paxton⁴² method with the same σ value is used as the default. All calculations are conducted without spin polarization, except for analysis of the S₂ dimer in vacuum which provides a reference energy for the S species. In *Appendix*, we also show some results from spin polarized calculations.

For cluster calculations with VASP, each cluster is contained in a supercell which is repeated with a simple cubic periodicity. The size of the supercell is so chosen that the closest separation between the edges of periodic images of the cluster is at least 12 Å. Because the periodicity has no physical meaning, a $(1 \times 1 \times 1)$ or Γ point only k -points grid is used. For a slab geometry, the (111) surface is modeled by supercells with shape and size so chosen that along the z direction, the slabs are separated by 12 Å, whereas perpendicular to the z direction, the computational supercell vectors correspond to various multiples of those for the primitive unit cell of the (111) surface.

Our primary interest here is in characterizing and understanding the variation of the S-metal interaction with the size of the cluster, rather than in modeling any particular physical realization of nanocluster geometries (e.g., for supported versus unsupported cases). To facilitate more extensive analysis with respect to both the size range of the clusters and also with respect to different methodologies, the relative positions of atoms in the Cu clusters are fixed at their bulk positions. In other words, the clusters can be thought of as cut from a bulk face-centered cubic (fcc) solid with no relaxation allowed. The lattice constant used is 3.641 Å, obtained from bulk calculations, which corresponded to 2.574 Å for nearest-neighbor Cu–Cu distance. The S atom is allowed to relax upon the frozen substrate, with energy minimization under the criterion that the maximal force is less than 0.02 eV/Å. In *Appendix A*, we show results from calculations with fully relaxed clusters.

The adsorption energy of S on a cluster is calculated using $E_b(\text{S}) = E(\text{S} + \text{cluster}) - E(\text{cluster}) - E(\text{S}_2, \text{gas})/2$, where $E(\text{S} + \text{cluster})$ is the total energy of the cluster plus S adsorbate system, $E(\text{cluster})$ is the energy of the cluster itself, and $E(\text{S}_2, \text{gas})$ is the energy of a S₂ molecule (spin-polarized).

Additional plane-wave VASP-based analyses includes calculation of the site-projected density of states (DOS). Also, the crystal orbital Hamilton population (COHP) analysis is applied to gain some understanding of bond strengths.³³

DFT calculations with an atomic basis set are performed with NWChem³⁵ and GAMESS^{36,37} using PBE²⁶ and PBE0⁴³ functionals. The basis sets used are Los Alamos National Laboratory double- ζ (LANL2DZ) with effective core potentials (ECP's)⁴⁴⁻⁴⁶ for Cu and 6-311++G(d,p) for S.⁴⁷⁻⁴⁹ All basis sets are taken from the EMSL basis set exchange Web site.⁵⁰ The geometries for the calculations were those from the planewave DFT

calculations. The multiplicity of a cluster is either a singlet for an even number of Cu or a doublet for an odd number. The S₂ dimer energy was calculated in a triplet state with a restricted open-shell. Molecular orbitals were analyzed using MacMolplt.⁵¹

3. Results for Adsorption Energy and Bonding Characterization

3.1. Variation of Adsorption Energy with Cluster Size.

Clusters with tetrahedral (T_d) symmetry are a natural choice for the study of adsorption on (111) surfaces. *Figure 2.1(a–d)* shows several examples of the T_d clusters considered. One subclass denoted by m0 corresponds to perfect tetrahedra bounded by four equilateral triangular surfaces. Another class m1 represents T_d clusters with the apex atom at the bottom removed. Clusters with an atom removed from each vertex (a total of four removed), are denoted by m4, and clusters with 4 atoms removed from each vertex (a total of 16 removed) are denoted by m16. Below, $N_{Cu} = n$ will denote the number of Cu atoms in the cluster. We then calculate the adsorption energy of S on clusters of various sizes in these classes. For extended (111) surfaces of fcc crystals, there are two types of 3-fold hollow (3fh) sites. The first type corresponds to a site where atoms would reside when extending the bulk fcc lattice, and is thus named fcc site. Directly beneath an fcc site, one finds a hollow site in the second layer, and an atom in the third layer. The second type has an atom directly beneath it in the second layer, and a hollow site in the third layer. They are called hcp site, because the top three layers mimic the stacking sequence of hexagonal close packed crystals.

We first consider S adsorption at fcc sites. Note that for m0 clusters, only in cases where the number of layers is a multiple of three (corresponding to $n = 10, 56, 165, \dots$) does the center of each face correspond to an fcc site. *Figure 2.2* shows results from our plane-wave DFT analysis using VASP for the adsorption energy E_b on fcc sites that are closest to the center for various clusters. Very large variations in E_b are observed for all types of

clusters. The variation has a damped oscillatory form and with near constant period when plotted against $n^{1/3}$ which reflects the linear dimension of the cluster recalling that $n = N_{Cu}$ is the number of Cu atoms in the cluster. The oscillation amplitude remains significant (around 0.3 eV) even for clusters as large as 200 atoms.

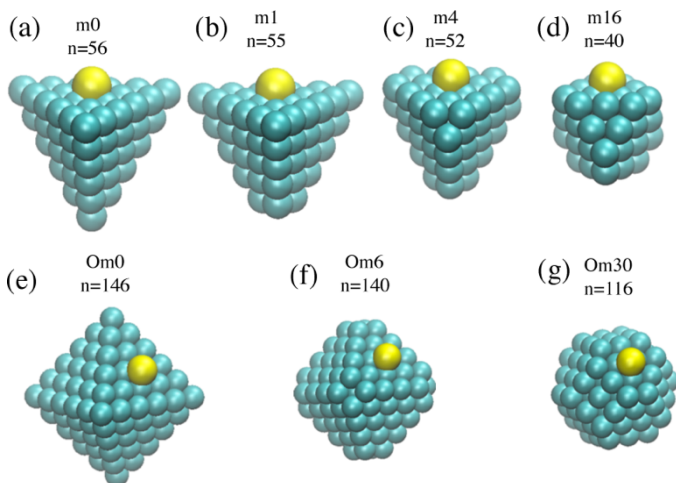


Figure 2.1 Top panels: Various classes of tetrahedral (T_d) clusters. (a) Perfect tetrahedron (class m_0), (b) tetrahedron with the bottom apex atom removed (class m_1), (c) with all four apex atoms removed (class m_4), and (d) with four atoms from each vertex removed (class m_{16}). Bottom panels: clusters with octahedral (O_h) symmetry: (e) perfect octahedron (class Om_0), (f) octahedron with the apex atom from each vertex removed (class Om_6), and (g) four atoms from each vertex removed (class Om_{30}).

Another observation from *Figure 2.2* is that for clusters that are smaller than $n = 20$, which consists of four layers of Cu for the m_0 cluster, just removing one apex atom from the bottom of the cluster significantly affects the adsorption energy. This suggests that the electronic interaction between S and the cluster is highly nonlocal. Only for clusters that are larger than 200 does the choice of truncation at the cluster corners far away from the S atoms have a minimal effect on the adsorption energy.

There are some advantages in using atomic versus plane-wave basis sets for cluster calculations, since the latter suffers from several artifacts, such as periodicity, thermal smearing of the occupancy function, and so forth. Therefore, we also perform multiple sets of

calculations with an atomic basis set using NWChem and GAMESS. For these sets of calculation, we consider only m0 clusters (untruncated tetrahedrons). For clusters with $n = 4, 35, 120$, the adsorption sites at the facet centers are hcp sites. For all other clusters, the adsorption site is the fcc site at or closest to the center. Results for the S adsorption energy from these analyses are compared with each other and with the results obtained from the plane-wave analysis in *Figure 2.3*.

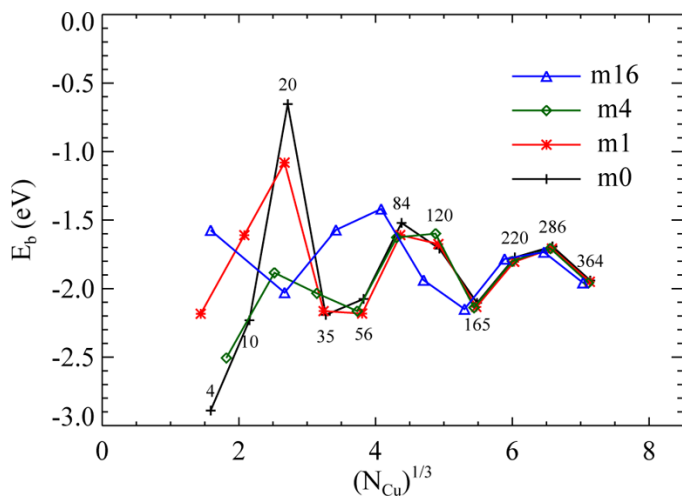


Figure 2.2 Plane-wave DFT results for the adsorption energy of S on Cu clusters on the fcc site closest to the center of a cluster of various sizes and shapes. Lines with various colors connects clusters of various classes shown in Figure 2.1.

The results for adsorption energy from these various methods of calculation generally agree quite well with each other. Not surprisingly, GAMESS-PBE and NWChem-PBE calculations agree with each other perfectly because they use both the same basis set and functionals. Results from atomic basis sets for E_b generally predict stronger binding than the plane-wave VASP results. We have also performed calculations with the hybrid PBE0 functional⁴³ using NWChem. Results are generally consistent with the PBE functional, with slightly stronger binding for $n = 4, 10, \text{ and } 84$, and weaker binding for $n = 20, 35, \text{ and } 56$.

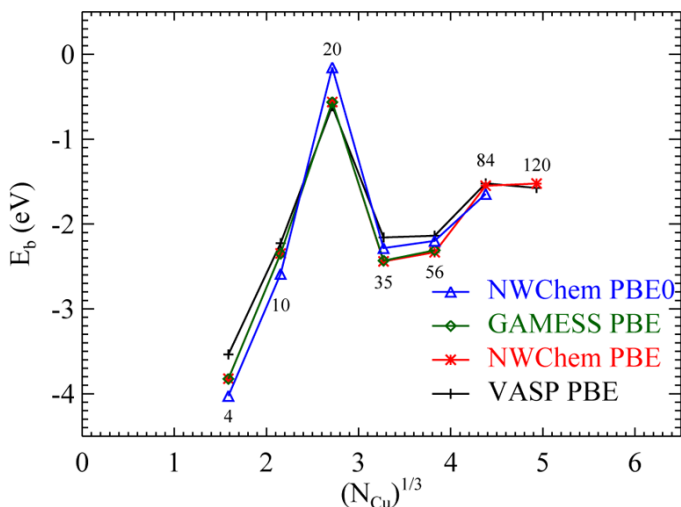


Figure 2.3 Comparison of the size dependence of E_b on 3fh sites on the m_0 clusters calculated using different methods.

All adsorption energies reported in this paper neglect zero point energies (ZPE).

Using frozen substrates, we estimate ZPE to be 0.041, 0.036, 0.033, 0.041, and 0.040 eV for the first five data points in *Figure 2.3*, which shows a slight compensatory effect in the sense that ZPE is higher in clusters with stronger bonding. However, it is insignificant compared with the overall oscillations in E_b .

Finally, for comparison with the above analysis of S adsorption on clusters with tetrahedral symmetry, we more briefly consider the case of octahedral symmetry restricting our considerations to plane-wave DFT analysis. Analogous to above, we consider different classes of geometries corresponding to a perfect octahedron (Om0), clusters with one Cu atoms removed from each vertex (Om6), and clusters with 5 Cu atoms removed from each vertex (Om30). See *Figure 2.1*. Results for the S adsorption energies are shown in *Figure 2.4*. For untruncated Om0 clusters, compared with results for untruncated tetrahedral clusters, the variations for small to medium clusters are not as dramatic. With the exception of the Om6 $n = 13$ cluster, no exceptionally large deviation from the bulk value are observed. On the other hand, the expectation that more compact clusters converge faster is not universally

true. There is still a variance of 0.4 eV for Om30 clusters, which are the most compact, for $n > 200$. This indicates that the oscillation is intrinsic regardless of the geometric shape of the cluster.

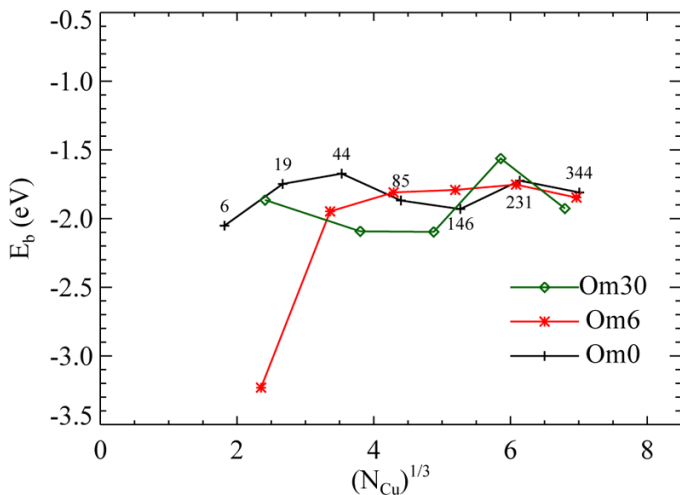


Figure 2.4 Adsorption energy of S on octahedral Cu clusters on the fcc site closest to the center of a cluster of various sizes and shapes. Lines with various colors connects clusters of various classes shown in Figure 2.1.

3.2. DOS, COHP, and MO Analysis.

Figure 2.5 shows the site- projected density of states (SDOS) of the S adatom on various m0 clusters from plane-wave DFT VASP calculations. To avoid complications arising from different symmetries, we focus on clusters for which the adsorption site at the center of the facets are 3fh sites. Specifically, these include hcp sites for $n = 4, 35, 120$, and fcc sites for $n = 10, 56, 165$. Plots are shifted vertically so that various SDOS curves are distinguishable, and the energies are shifted according to the Fermi energy E_F . Also plotted at the bottom is the SDOS of the S adatom calculated using the slab geometry. Not shown on this plot is a very low lying peak centered around 12.7 eV below the Fermi level. Two distinct regions of significant SDOS can be observed. The first region is between 3 and 5 eV below E_F . The second region is closer to the Fermi level. Significant size variations persist for all clusters shown in this plot. Although some degree of convergence can be argued to

emerge for the lower region, the region closer to the Fermi level shows no sign of convergence as cluster size increases.

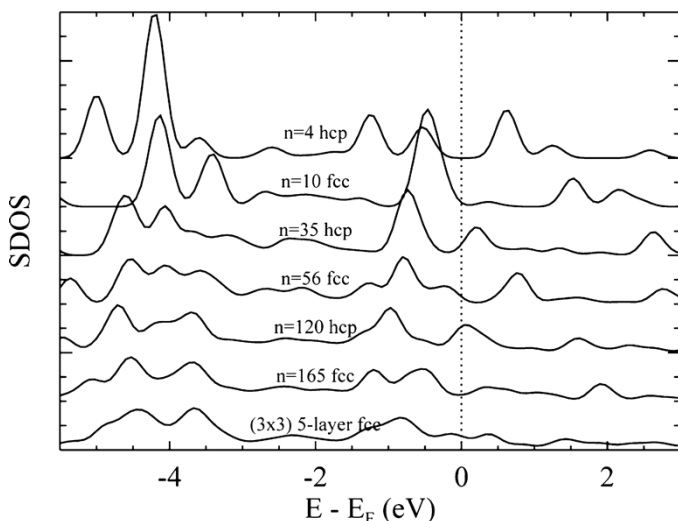


Figure 2.5 Site projected density of states (SDOS) of the S on various clusters and a slab.

For plane-wave DFT calculations, the nature of the binding of S with the cluster can be more clearly demonstrated by crystal orbital Hamilton population (COHP) analysis.³³ Results of a COHP analysis for S on the same set of clusters analyzed in *Figure 2.5* are plotted in *Figure 2.6*. Negative (positive) COHP values, corresponding to higher (lower) portions of curves in *Figure 2.6*, suggest bonding (antibonding) interactions. It is clear from this analysis that the orbitals around -4.5 eV below E_F are mostly bonding, whereas the orbitals close to E_F are mostly antibonding. Similar to the SDOS analysis, we find slow convergence of the bonding orbitals with increasing cluster size, and no sign of convergence for the antibonding orbitals.

Figure 2.7 shows three families of MOs that represent the three most visible peaks for S on the fcc site of Cu_{10} clusters, for both SDOS and COHP. The first set of three MOs have energy 3.88 to 3.80 eV below the HOMO energy. The interactions are binding and can be mostly characterized by $\text{Cu}(s)\text{--S}(p)$. The second set of MOs are at 3.10 to 3.13 eV below the HOMO energy. They are also attractive and can be mostly characterized by $\text{Cu}(d)\text{--S}(p)$. The

third set is antibonding, including the HOMO and two other MO that lies 0.21 eV below the HOMO energy. They can be mostly characterized by $\text{Cu}(s)\text{--S}(p)$. The character of some of the MOs can be more easily seen if one views the Cu cluster as a whole. If one compares *1a* with *3a*, the phases of the $S p_z$ orbital are the same, whereas the phases of the orbitals encompassing the Cu cluster are reversed. Similar observations can be made for *1b* and *3b* as well as *1c* and *3c*. Thus, the $\text{Cu}(d)\text{--S}(p)$ couplings are mostly bonding, whereas $\text{Cu}(s)$ and $\text{S}(p)$ couplings contribute both to bonding and antibonding.

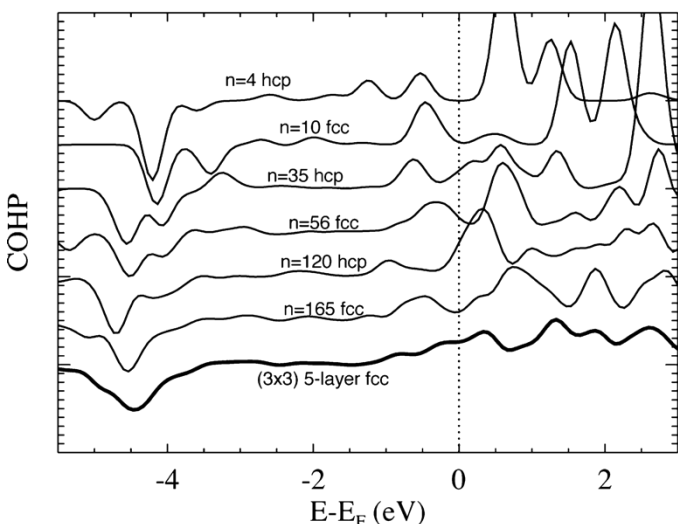


Figure 2.6 COHP of S with the three closest Cu atoms on tetrahedral clusters of various sizes, and on a five layer slab in a (3×3) supercell.

4. Relationship of the S Binding Energy and Shell-structure of Cu Clusters

The oscillatory behavior in E_b is most likely due to the quantum confinement in nanoclusters.^{28,29} Previous studies related to QSE generally focused on the energetics and stabilities of pure metal clusters^{28,29} or thin films.^{30,31} DFT studies of a deformable jellium model by Reimann et al.³⁴ found the first shells at $n = 2, 8, 20, 40, 70,$ and 112 for clusters with tetrahedral deformations. For univalent metal clusters such as Cu, tetrahedral clusters of those sizes are expected to have a closed-shell electronic structure, as far as the s electron is concerned. Perfect tetrahedrons, which correspond to the m0 class of clusters in *Figure 2.1*,

can be considered to exhibit geometric “magic” numbers, $n = 4, 10, 20, 35, 56, \dots$. The case of $n = 20$ is especially interesting, as it is a magic number for both electronic and geometric structures.

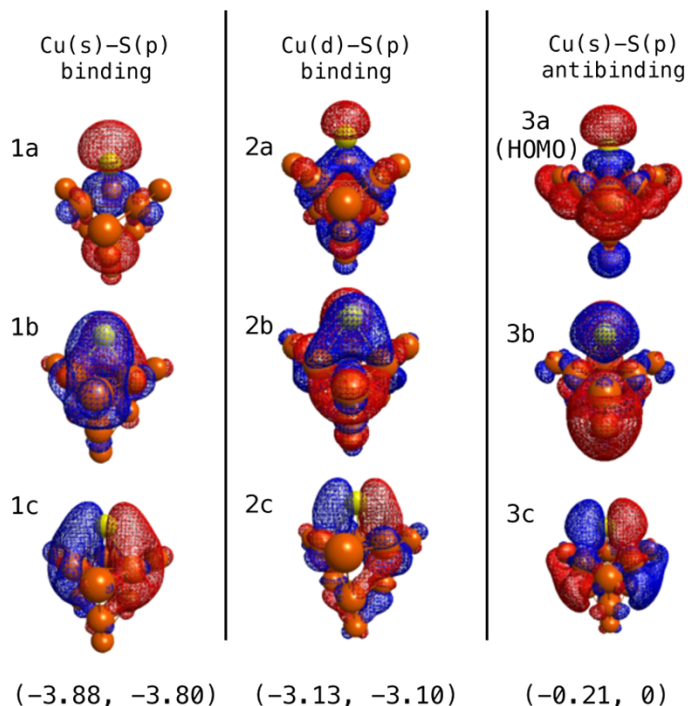


Figure 2.7 Molecular orbitals (MOs) that contribute the most to interactions between S and Cu on Cu_{10} clusters, using GAMESS and MacMolPlt. The energies of MOs relative to the HOMO energy are indicated below the orbitals.

As Figure 2.2 shows, adsorption of S on the fcc site near the center of the face of a $n = 20$ tetrahedral cluster is especially weak. This is perhaps not surprising, considering that it is often argued that the closed-shell clusters should have a low chemical reactivity. This is analogous to the low reactivity of noble gases, their atomic counterparts. Indeed, Au_{20} clusters are found⁵² to possess a tetrahedral structure, with an exceptionally large gap between the highest occupied molecular orbital (HOMO) and lowest unoccupied molecular orbital (LUMO). We find a similarly large HUMO-LUMO gap (1.22 eV from VASP, 1.34 eV from NWChem) for the tetragonal Cu_{20} cluster. The next largest gap for the T_d m0 class clusters with $10 < n < 364$ is about five times smaller at $n = 120$ (0.27 eV from VASP, 0.24

eV from NWChem). As far as we know, no previous experimental or theoretical study^{53,54} has shown the tetrahedral Cu₂₀ being more stable than other competing structures. On the other hand, Ag nanocrystals have been shown to form spontaneously as stacking-fault tetrahedrons in Ag(111) films.⁵⁵

To obtain a more comprehensive picture of the interaction between S and the Cu₂₀ tetrahedral cluster, we explore the adsorption energy as a function of adsorption site location on the (111) facet. Results are shown in *Figure 2.8a*. There are two types of hcp sites: the ones closer to the center (hcp) and the ones near the corners (hcp1). For fcc sites, only the ones near the center (fcc) are 3-fold coordinated. Moving further away from the center results in fcc sites that are on the edge. Adsorption energies on all sites are less negative than the converged large cluster limit (around -1.75 eV). This is consistent with the conjecture of lower reactivity of closed-shell systems. However, the fcc sites in the middle are exceptionally unstable sites. In fact, the fcc site on the edge is more favorable toward S adsorption, in contrast to the general picture that S prefer higher coordinated adsorption sites. Further insights can be obtained from a molecular orbital analysis. *Figure 2.8b* shows the isodensity plot for the HOMO and LUMO of the clean Cu₂₀ cluster and the cluster with S on the fcc and hcp sites near the center. For the clean cluster, the electron density of the HOMO is concentrated near the edges, and the LUMO density is concentrated at the corners. The HOMO and LUMO of the S-adsorbed clusters reflect coupling of the $p_{x,y}$ and p_z orbitals and the HOMO of the Cu₂₀ cluster. The fcc site is close to a nodal point of both the HOMO and LUMO of the clean cluster, whereas the other adsorption sites are located in regions of higher electron density. Thus, the shape of the frontier orbitals of the clean cluster correlates with the strength of the binding.

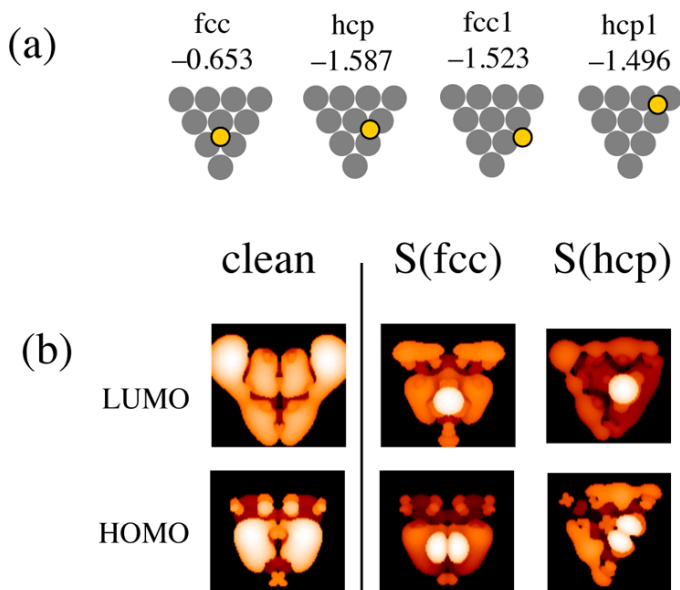


Figure 2.8 (a) $E_b(S)$ (in eV) for S on various adsorption sites of the tetrahedral Cu_{20} cluster. (b) HOMO and LUMO of the clean Cu_{20} cluster, with a S on the fcc and hcp site near the center.

5. Discussion and Conclusions

We systematically calculate the interaction of S on 3fh sites of Cu clusters with tetrahedral geometry of various sizes and find strong oscillation in the adsorption energy, persisting to the largest clusters calculated (up to 364 atoms). There is good agreement between results obtained from plane-wave and atomic orbital basis set calculations. Strong oscillations in the adsorption energy have their origin in the shell structure of the Cu cluster due to quantum confinement. Furthermore, for the “magic” Cu_{20} cluster with closed-shell electronic structure, a large HOMO–LUMO gap gives rise to both an overall weaker binding, and particularly weak binding at certain 3fh sites near the (111) facet center.

Although extensive DFT studies of chemisorption on metal clusters exist, results presented here are still somewhat surprising. It is generally expected that quantum size effects (QSE) for chemisorption are significant when the energy levels are discrete with gaps on the order of several electronvolts near the Fermi level; therefore, they should diminish for

clusters on the order of several hundred atoms.² However, we find that at least for the particular system of S on tetrahedral Cu clusters, the expectation of reaching thermodynamic scaling regime for clusters of a few hundred atoms is not justified. Using the more compact octahedral clusters reduces the variation with size to some extent, but significant oscillatory behavior still exists. This variation is not due to the discrete nature of MOs in finite clusters, which is a narrower interpretation of QSE. As shown in Section 3.2, a DOS and COHP description of the interaction between S and Cu clusters already emerges for clusters of 35 atoms. Larsen et al.⁵ calculated and analyzed the electronic structure of Au clusters up to 200 atoms using real-space DFT with optimized structures (up to 60 with DFT, and up to 200 with effective medium theory). They also calculated the chemisorption energy of O, F, and H/Li on cuboctahedral clusters. Results for O should be more directly comparable with S. In this analysis, adsorption on clusters with $n = 34, 58, 92,$ and $138,$ which correspond to closed-shell magic numbers, are particularly unfavorable. Our results are consistent with their observation that closed-shell clusters are less favorable for chemisorption but also reveal much larger variation of the adsorption energy for different adsorption site locations for closed-shell clusters.

Acknowledgments

This work was supported by the U.S. Department of Energy (U.S. DOE), Office of Basic Energy Sciences, Division of Chemical Sciences, Geosciences, and Biosciences through the Ames Laboratory Chemical Physics program. We acknowledge use of NERSC computational resources. The work was performed at Ames Laboratory, which is operated for the U.S. DOE by Iowa State University under Contract No. DE-AC02-07CH11358.

References

1. Soini, T. M.; Rösch, N. Size-dependent properties of transition metal clusters: from molecules to crystals and surfaces - computational studies with the program PARAGAUSS. *Phys. Chem. Chem. Phys.* **2015**, *17*, 28463–28483.
2. Kleis, J.; Greeley, J.; Romero, N. A.; Morozov, V. A.; Falsig, H.; Larsen, A. H.; Lu, J.; Mortensen, J. J.; Dułak, M.; Thygesen, K. S.; et al. Finite Size Effects in Chemical Bonding: From Small Clusters to Solids. *Catal. Lett.* **2011**, *141*, 1067–1071.
3. Li, L.; Larsen, A. H.; Romero, N. A.; Morozov, V. A.; Glinsvad, C.; Abild-Pedersen, F.; Greeley, J.; Jacobsen, K. W.; Nørskov, J. K. Investigation of Catalytic Finite-Size-Effects of Platinum Metal Clusters. *J. Phys. Chem. Lett.* **2013**, *4*, 222–226.
4. Hu, Q.-M.; Reuter, K.; Scheffler, M. Towards an exact treatment of exchange and correlation in materials: application to the “CO adsorption puzzle” and other systems. *Phys. Rev. Lett.* **2007**, *98*, 176103.
5. Larsen, A. H.; Kleis, J.; Thygesen, K. S.; Nørskov, J. K.; Jacobsen, K. W. Electronic shell structure and chemisorption on gold nanoparticles. *Phys. Rev. B: Condens. Matter Mater. Phys.* **2011**, *84*, 245429.
6. Yudanov, I. V.; Genest, A.; Schauer mann, S.; Freund, H.-J.; Rösch, N. Size Dependence of the Adsorption Energy of CO on Metal Nanoparticles: A DFT Search for the Minimum Value. *Nano Lett.* **2012**, *12*, 2134–2139.
7. Yudanov, I. V.; Metzner, M.; Genest, A.; Rösch, N. Size- Dependence of Adsorption Properties of Metal Nanoparticles: A Density Functional Study on Palladium Nanoclusters. *J. Phys. Chem. C* **2008**, *112*, 20269–20275.
8. Yudanov, I. V.; Sahnoun, R.; Neyman, K. M.; Rösch, N. Metal nanoparticles as models of single crystal surfaces and supported catalysts: Density functional study of size effects for CO/Pd(111). *J. Chem. Phys.* **2002**, *117*, 9887–9896.
9. Soini, T. M.; Krüger, S.; Rösch, N. The DFT+Umol method and its application to the adsorption of CO on platinum model clusters. *J. Chem. Phys.* **2014**, *140*, 174709.
10. Huang, Y.-W.; Lee, S.-L. Hybrid DFT and hyper-GGA DFT studies of the CO adsorption on Pt nanoclusters: Effects of the cluster size and better CO LUMO description. *Chem. Phys. Lett.* **2010**, *492*, 98– 102.
11. Jacob, T.; Muller, R. P.; Goddard, W. A., III Chemisorption of atomic oxygen on Pt(111) from DFT studies of Pt-clusters. *J. Phys. Chem. B* **2003**, *107*, 9465–9476.
12. Xie, Y.-P.; Gong, X.-G. First-principles studies for CO and O₂ on gold nanocluster. *J. Chem. Phys.* **2010**, *132*, 244302.

13. Ackermann, L.; Rösch, N. Chemisorption of sulfur on nickel: A study of cluster convergence in the linear combination of Gaussian-type orbitals local density functional approach. *J. Chem. Phys.* **1994**, *100*, 6578–6590.
14. Wahlström, E.; Ekvall, I.; Kihlgren, T.; Olin, H.; Lindgren, S.-Å.; Walldén, L. Low-temperature structure of S/Cu(111). *Phys. Rev. B: Condens. Matter Mater. Phys.* **2001**, *64*, 155406.
15. Ling, W. L.; Bartelt, N. C.; Pohl, K.; de la Figuera, J.; Hwang, R. Q.; McCarty, K. F. Enhanced Self-Diffusion on Cu(111) by Trace Amounts of S: Chemical-Reaction-Limited Kinetics. *Phys. Rev. Lett.* **2004**, *93*, 166101.
16. Liu, D.-J.; Walen, H.; Oh, J.; Lim, H.; Evans, J. W.; Kim, Y.; Thiel, P. A. Search for the Structure of a Sulfur-Induced Reconstruction on Cu(111). *J. Phys. Chem. C* **2014**, *118*, 29218–29223.
17. Walen, H.; Liu, D.-J.; Oh, J.; Lim, H.; Evans, J. W.; Aikens, C. M.; Kim, Y.; Thiel, P. A. Cu₂S₃ complex on Cu(111) as a candidate for mass transport enhancement. *Phys. Rev. B: Condens. Matter Mater. Phys.* **2015**, *91*, 045426.
18. Shen, M.; Liu, D.-J.; Jenks, C. J.; Thiel, P. A.; Evans, J. W. Accelerated coarsening of Ag adatom islands on Ag(111) due to trace amounts of S: Mass-transport mediated by Ag-S complexes. *J. Chem. Phys.* **2009**, *130*, 094701.
19. Russell, S. M.; Kim, Y.; Liu, D.-J.; Evans, J. W.; Thiel, P. A. Communication: Structure, formation, and equilibration of ensembles of Ag-S complexes on an Ag surface. *J. Chem. Phys.* **2013**, *138*, 071101.
20. Walen, H.; Liu, D.-J.; Oh, J.; Yang, H. J.; Kim, Y.; Thiel, P. A. Long-range Displacive Reconstruction of Au(110) Triggered by Low Coverage of Sulfur. *J. Phys. Chem. C* **2015**, *119*, 21000–20010.
21. Biener, M. M.; Biener, J.; Friend, C. M. Sulfur-induced mobilization of Au surface atoms on Au(111) studied by real-time STM. *Surf. Sci.* **2007**, *601*, 1659–1667.
22. Maksymovych, P.; Voznyy, O.; Dougherty, D. B.; Sorescu, D. C., Jr.; Yates, J. T. Gold adatom as a key structural component in self-assembled monolayers of organosulfur molecules on Au(111). *Prog. Surf. Sci.* **2010**, *85*, 206–240.
23. Bailie, J. E.; Hutchings, G. J. Promotion by sulfur of gold catalysts for crotyl alcohol formation from crotonaldehyde hydrogenation. *Chem. Commun.* **1999**, *21*, 2151–2152.
24. Vericat, C.; Vela, M. E.; Benitez, G.; Carro, P.; Salvarezza, R. C. Self-assembled monolayers of thiols and dithiols on gold: new challenges for a well-known system. *Chem. Soc. Rev.* **2010**, *39*, 1805–1834.

25. Häkkinen, H. The gold-sulfur interface at the nanoscale. *Nat. Chem.* **2012**, *4*, 443–455.
26. Perdew, J. P.; Burke, K.; Ernzerhof, M. Generalized Gradient Approximation Made Simple. *Phys. Rev. Lett.* **1996**, *77*, 3865–3868., Erratum-ibid. 1997, **78**, 1396.
27. Liu, D.-J. Density functional analysis of key energetics in metal homoepitaxy: quantum size effects in periodic slab calculations. *Phys. Rev. B: Condens. Matter Mater. Phys.* **2010**, *81*, 035415.
28. de Heer, W. A. The Physics of simple metal clusters: experimental aspects and simple models. *Rev. Mod. Phys.* **1993**, *65*, 611–676.
29. Brack, M. The physics of simple metal clusters: self-consistent jellium model and semiclassical approaches. *Rev. Mod. Phys.* **1993**, *65*, 677–732.
30. Schulte, F. K. A Theory of thin metal films: electron density, potentials and work function. *Surf. Sci.* **1976**, *55*, 427–444.
31. Miller, T.; Chou, M. Y.; Chiang, T.-C. Phase Relations Associated with One-Dimensional Shell Effects in Thin Metal Films. *Phys. Rev. Lett.* **2009**, *102*, 236803.
32. Lopez-Acevedo, O.; Kacprzak, K. A.; Akola, J.; Häkkinen, H. Quantum size effects in ambient CO oxidation catalysed by ligand-protected gold clusters. *Nat. Chem.* **2010**, *2*, 329–334.
33. Dronskowski, R.; Blöchl, P. E. Crystal Orbital Hamilton Populations(COHP). Energy-Resolved Visualization of Chemical Bonding in Solids Based on Density-Functional Calculations. *J. Phys. Chem.* **1993**, *97*, 8617–8624.
34. Reimann, S. M.; Koskinen, M.; Häkkinen, H.; Lindelof, P. E.; Manninen, M. Magic triangular and tetrahedral clusters. *Phys. Rev. B: Condens. Matter Mater. Phys.* **1997**, *56*, 12147–12150.
35. Valiev, M.; Bylaska, E.; Govind, N.; Kowalski, K.; Straatsma, T.; van Dam, H.; Wang, D.; Nieplocha, J.; Apra, E.; Windus, T.; et al. NWChem: a comprehensive and scalable open-source solution for large scale molecular simulations. *Comput. Phys. Commun.* **2010**, *181*, 1477–1489.
36. Schmidt, M. W.; Baldridge, K. K.; Boatz, J. A.; Elbert, S. T.; Gordon, M. S.; Jensen, J. H.; Koseki, S.; Matsunaga, N.; Nguyen, K. A.; Su, S.; et al. *J. Comput. Chem.* **1993**, *14*, 1347–1363.
37. Gordon, M. S.; Schmidt, M. W. In *Theory and Applications of Computational Chemistry, the first forty years*; Dykstra, C. E., Frenking, G., Kim, K. S., Scuseria, G. E., Eds.; Elsevier: Amsterdam, 2005; pp 1167– 1189.

38. Kresse, G.; Hafner, J. Ab initio molecular dynamics for liquid metals. *Phys. Rev. B: Condens. Matter Mater. Phys.* **1993**, *47*, R558–R561.
39. Kresse, G.; Furthmüller, J. Efficiency of ab-initio total energy calculations for metals and semiconductors using a plane-wave basis set. *Comput. Mater. Sci.* **1996**, *6*, 15–50.
40. Blöchl, P. E. Projector augmented-wave method. *Phys. Rev. B: Condens. Matter Mater. Phys.* **1994**, *50*, 17953–17979.
41. Kresse, G.; Joubert, D. From ultrasoft pseudopotentials to the projector augmented-wave method. *Phys. Rev. B: Condens. Matter Mater. Phys.* **1999**, *59*, 1758–1775.
42. Methfessel, M.; Paxton, A. T. High-precision sampling for Brillouin-zone integration in metals. *Phys. Rev. B: Condens. Matter Mater. Phys.* **1989**, *40*, 3616–3621.
43. Adamo, C.; Barone, V. Toward reliable density functional methods without adjustable parameters: The PBE0 model. *J. Chem. Phys.* **1999**, *110*, 6158–6170.
44. Hay, P. J.; Wadt, W. R. *Ab initio* effective core potentials for molecular calculations. Potentials for the transition metals atoms Sc to Hg. *J. Chem. Phys.* **1985**, *82*, 270–283.
45. Wadt, W. R.; Hay, P. J. *Ab initio* effective core potentials for molecular calculations. Potentials for the main group elements Na to Bi. *J. Chem. Phys.* **1985**, *82*, 284–298.
46. Hay, P. J.; Wadt, W. R. *Ab initio* effective core potentials for molecular calculations. Potentials for K to Au including the outermost core orbitals. *J. Chem. Phys.* **1985**, *82*, 299–310.
47. McLean, A. D.; Chandler, G. S. Contracted Gaussian basis sets for molecular calculations. I. Second row atoms, $Z = 11$ –18. *J. Chem. Phys.* **1980**, *72*, 5639–5648.
48. Krishnan, R.; Binkley, J. S.; Seeger, R.; Pople, J. A. Self-consistent molecular orbital methods. XX. A basis set for correlated wave functions. *J. Chem. Phys.* **1980**, *72*, 650–654.
49. Clark, T.; Chandrasekhar, J.; Spitznagel, G. W.; von Ragué Schleyer, P. Efficient diffuse function-augmented basis sets for anion calculations. III. The 3-21+G basis set for first-row elements, Li-F. *J. Comput. Chem.* **1983**, *4*, 294–301.
50. Schuchardt, K.; Didier, B.; Elsethagen, T.; Sun, L.; Gurumoorthi, V.; Chase, J.; Li, J.; Windus, T. L. Basis set exchange: a community database for computational sciences. *J. Chem. Inf. Model.* **2007**, *47*, 1045–1052.
51. Bode, B. M.; Gordon, M. S. *J. Mol. Graphics Modell.* **1998**, *16*, 133–138.

52. Li, J.; Li, X.; Zhai, H.-J.; Wang, L.-S. Au₂₀: a tetrahedral cluster. *Science* **2003**, *299*, 864–867.
53. Kabir, M.; Mookerjee, A.; Bhattacharya, A. K. Structure and stability of copper clusters: A tight-binding molecular dynamics study. *Phys. Rev. A: At., Mol., Opt. Phys.* **2004**, *69*, 043203.
54. Calaminici, P.; Pérez-Romero, M.; Vázquez-Pérez, J. M.; Köster, A. M. On the ground state structure of neutral Cu_n (*n*=12, 14, 16, 18, 20) clusters. *Comput. Theor. Chem.* **2013**, *1021*, 41–48.
55. Schouteden, K.; Haesendonck, C. V. Lateral Quantization of Two-dimensional Electron States by Embedded Ag Nanocrystals. *Phys. Rev. Lett.* **2012**, *108*, 076806.

Appendix. Effects of Cluster Relaxation and Spin Polarization

In order to reveal the generic feature of the size dependence of S-binding, we assume that the Cu atoms are fixed at their bulk positions. There can be questions as to what extent substrate relaxation can affect the results. We also calculate the S adsorption energy $E_b(S)$ assuming the substrate cluster can fully relax, by comparing the energies of a fully relaxed S-adsorbed cluster, and a fully relaxed clean cluster. The comparison with fixed substrate is given in *Figure 2.9*.

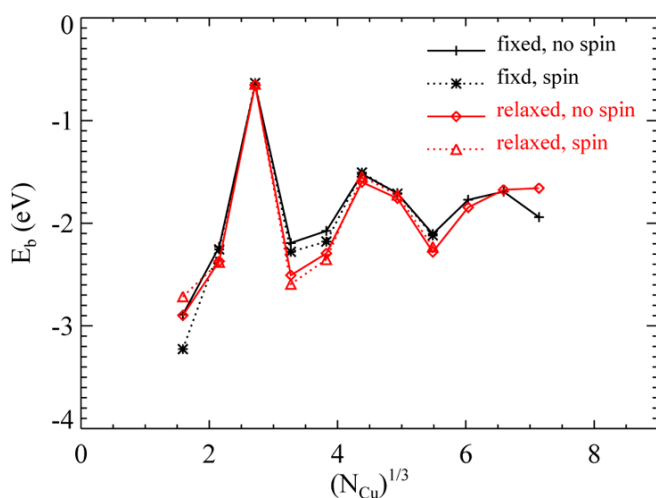


Figure 2.9 Comparison of the size dependence of E_b on fcc sites on the m0 tetrahedral clusters with different assumptions using plane-wave basis sets. Results with fixed substrate and no spin polarization are represented by diamonds, fixed substrate, and with spin polarization are represented by triangles, relaxed substrate with no spin polarization by pluses, and relaxed substrate with spin polarization by asterisks.

Also the VASP results presented in the main text are obtained without spin polarization (except for the S_2 dimer). For small clusters, the ground state may have nonzero magnetic moment. Results with spin polarization are also given in *Figure 2.9*, denoted by dotted lines, for both fixed and relaxed substrate. For small clusters, there are some differences due to different spin states, but the differences are small and generally decrease as the clusters grow larger. The comparison suggests the general feature of the size dependence is very robust.

CHAPTER 3. COMPARISON OF S-ADSORPTION ON (111) AND (100) FACETS OF CU NANOCCLUSERS

A paper published in and reprinted with permission from

The Journal of Chemical Physics **2016**, *145*, 164312

Jeffery S. Boschen,^{a,b} Jiyoung Lee,^{a,b} Theresa L. Windus,^{a,b} James W. Evans,^{a,d} Patricia A. Thiel,^{a,b,c} and Da-Jiang Liu^{a,*}

^a*Ames Laboratory – USDOE, Iowa State University, Ames, IA 50011, USA*

^b*Department of Chemistry, Iowa State University, Ames, IA 50011, USA*

^c*Department of Materials Science & Engineering, Iowa State University, Ames, IA 50011, USA*

^d*Department of Physics and Astronomy, Iowa State University, Ames, IA 50011, USA*

**Corresponding author*

Abstract

In order to gain insight into the nature of chemical bonding of sulfur atoms on coinage metal surfaces, we compare the adsorption energy and structural parameters for sulfur at four-fold hollow (4fh) sites on (100) facets and at three-fold hollow (3fh) sites on (111) facets of Cu nanoclusters. Consistent results are obtained from localized atomic orbital and plane-wave based density functional theory using the same functionals. PBE and its hybrid counterpart (PBE0 or HSE06) also give similar results. 4fh sites are preferred over 3fh sites with stronger bonding by ~ 0.6 eV for nanocluster sizes above ~ 280 atoms. However, for smaller sizes there are strong variations in the binding strength and the extent of the binding site preference. We show that suitable averaging over clusters of different sizes, or smearing the occupancy of orbitals, provide useful strategies to aid assessment of the behavior in extended surface systems. From site-projected density of states analysis using the smearing technique, we show that S adsorbed on a 4fh site has similar bonding interactions with the substrate as that on a 3fh site, but with much weaker antibonding interactions.

1. Introduction

The favored site of a surface adsorbate, and the reasons for that site preference, are among the most fundamental types of insight into any surface chemical system. In that vein, early studies of sulfur (S) adsorption on and reconstruction of Cu(111) surfaces indicated a particular stability of structural motifs where a S adatom resides on the four-fold-hollow (4fh) site of a planar square Cu₄ unit. This, in turn, suggested an energetic preference for adsorption of S at more highly coordinated 4fh sites versus lower-coordinated 3fh sites on Cu surfaces.¹ More recent density functional theory (DFT) analysis indicated that reconstructions for the S/Cu(111) system can be stabilized by such motifs.² Along this line, a comprehensive integrated experimental and DFT analysis of step edge decoration and reconstruction for S on stepped Cu(111) surfaces consistently indicated a preference for S at 4fh sites. Specifically, (111) micro-faceted steps, which do not present natural 4fh sites, underwent a complex S-induced reconstruction in which Cu atoms shift from their original sites and thereby form a Cu atom base which enables S adsorption at 4fh-type sites.³

As an aside, S on other metal(111) surfaces appear to exhibit a similar behavior. S-induced reconstructions on Ni(111) have been observed to incorporate presumed stable Ni₄S units.⁴ Ag-S complexes which form on Ag(111) at low temperature, including Ag₁₆S₁₃ and larger elongated complexes, consist of overlapping units of Ag₁₆S₁₃, also incorporate prominent Ag₄S motifs.⁵

The determination and comparison of the binding energies for S on extended (100) and (111) surfaces of Cu is most naturally performed with plane-wave DFT analysis utilizing a slab geometry with periodic boundary conditions. Stabilities of both chemisorbed sulfur atoms and Cu-S complexes have been studied using this method.⁶⁻⁸ A series of calculations with increasing lateral unit cell size with one adsorbate per unit cell enables estimation of the

behavior in the limit of zero coverage (or infinite cell size). Unfortunately, such slab calculations often exhibit a surprisingly strong dependence of energetics on the choice of slab thickness, i.e., they can suffer somewhat slow convergence to a limiting behavior for infinite thickness (corresponding to the semi-infinite surface system of interest). It has been proposed that appropriate averaging of results over slab thicknesses can eliminate such quantum size effects (and also k -points and/or basis sets convergence issues).^{8,9} We return to this theme below.

In this contribution, to provide a more extensive analysis of the adsorption site dependence of S bonding than the above type of slab calculations, we consider the behavior for sequences of square pyramidal nanoclusters with exposed base (100) facets, as well as tetrahedral nanoclusters with exposed (111) facets. As an aside, such analysis is potentially also relevant for characterization of chemisorption on supported metal nanoclusters. For sufficiently large clusters above ~ 280 atoms, we find a consistently strong preference for binding at 4fh sites on (100) facets versus 3fh sites on (111) facets by ~ 0.6 eV. However, highly accurate DFT calculations show variations in binding of around 0.4 eV for clusters as large as 200 Cu atoms. Furthermore, there is no sign of the often-anticipated¹⁰ simple exponential decay in the size dependence of the adsorption energy, even for systems with linear size as large as 3 nm. As a consequence, this brings into question a picture of the S–Cu chemical bond as being local in nature.

The above observations highlight two related challenges in understanding these adsorption systems. As emphasized above, adsorption energetics for clusters of finite size (or for slabs of finite thickness) can exhibit strong deviations from the behavior on extended surfaces. This derives in part from the lack of localization in chemical bonding which in turn

complicates the characterization of such bonding, including the understanding of the difference in bonding between 3fh and 4fh adsorption sites. Actually, it has been long recognized, but perhaps under-appreciated, that locality arises from cancellation of different phases of the Bloch states in extended systems.¹¹⁻¹³ This type of cancellation should not be expected to occur for calculations performed on a single cluster with simple geometric shape, even with hundreds of atoms, as coherent interference can occur between electron waves scattering from the different cluster surfaces. Elimination of the strong size dependence and associated enhancement of localization should occur by introducing some type of randomization into the system, e.g., by incorporating random defects, or by introducing rough surfaces. Below, we describe two strategies to mimic such randomization which we propose will reduce the size-dependence of energetics, thus making binding strength and site preference better match those for the extended semi-infinite surface.

Suitably averaging over the energetics of clusters of different sizes is one way to introduce the cancellation effect described above. We find that by averaging results for a range of cluster sizes, N_{Cu} measured in atoms (roughly speaking in the range from $N_{\text{Cu}} = 100$ to 400), one can achieve essentially the same adsorption energies using finite clusters as those from slab geometry calculations.

A more efficient method to assess the behavior in extended surfaces is to utilize partial (fractional) occupancies, which are implemented in many DFT codes, to smear out the effect of the Fermi (HOMO) energy. In Sec. 4, we explore the effects of broadening the occupancy function and show that much faster convergence to energetics for the semi-infinite surface system can be achieved by judiciously choosing the broadening parameter. Furthermore, comparing the density of states (DOS's) projected onto the adsorbate using the

broadened occupancy, the role of antibonding orbitals is clarified, thus facilitating understanding of the difference in adsorption energy between the 3fh and 4fh sites.

Section 2 briefly summarizes the computational methods used in this paper. The main results comparing S binding on (111) and (100) facets of clusters of various sizes and averaging over large cluster sizes are presented in Sec. 3. Results obtained by broadening the occupancy function, and the associated understanding of the difference in bonding at 3fh and 4fh sites, are presented in Sec. 4. Further discussion and conclusions are provided in Sec. 5.

2. Computational Details

DFT calculations are performed using both plane-wave (VASP^{14,15} version 5.4.1) and Gaussian (NWChem¹⁶) basis sets. More technical details can be found in a previous paper.¹⁷ All calculations are without spin polarization, except for the S₂ dimer in vacuum. PBE¹⁸ functionals are used in VASP and NWChem calculations. The hybrid PBE0 functional¹⁹ is also used in NWChem calculations, and its screened version (HSE06²⁰) is used in VASP calculations. For VASP calculations, the PAW potentials for Cu and S that are optimized for the PBE functional are used.²¹ The cutoff energy for the plane-wave basis set is 280 eV. For NWChem, basis sets are Los Alamos National Laboratory double zeta with effective core potential (LANL2DZ ECP) for Cu²² and 6-311++G(d,p) for S.²³⁻²⁵ Some results are also checked with the larger basis sets def2-QZVP and def2-QZVPPD.^{26,27}

Calculations of S adsorption are performed using VASP for both slab and cluster geometries. For slab calculations, surfaces are simulated by periodic slabs of various thicknesses separated by 1.2 nm of vacuum. Supercells are chosen so that two of the basis vectors are that of superlattices of Cu(100) or Cu(111) surface, and the third is perpendicular to the slab surface. For clusters, orthorhombic supercells are used so that each supercell

contains one Cu cluster, separated by 1.2 nm of vacuum in all three directions. NWChem calculations are performed for clusters only, but with open boundaries.

3. Analysis of S Adsorption on Isolated Clusters

All clusters considered in this paper are formed by truncation of bulk fcc Cu. One can regard them as being constructed by starting from a single atom and then adding various numbers of layers with suitable structure and increasing areas. The S atom will be adsorbed near the center of the last largest layer added. Two classes of clusters are thereby constructed. To mimic adsorption on a (111) surface, we add hexagonally close-packed equilateral triangular layers with side lengths 2, 3, up to l (in atoms). This generates a series of clusters of tetrahedral (T_d) symmetry. The number of Cu atoms N_{Cu} in a cluster can be written as $N_{\text{Cu}} = l(l+1)(l+2)/6$. For $l = 3m + k$, where $m \geq 0$ and $0 \leq k \leq 2$ are integers, the center of the facet is a fcc site, hcp site, or top site, if $k = 0, 1$, or 2 , respectively. For the 3fh site, we choose the center fcc and hcp sites when $k = 0$ and 1 , and the fcc site closest to the center when $k = 2$.

To mimic adsorption on the (100) surface, we instead add square layers with side lengths 2, 3, up to l (in atoms). The clusters thus generated can be viewed as octahedral clusters cut in half, thereby denoted as O_h^2 clusters and $N_{\text{Cu}} = l(l+1)(2l+1)/6$. Only for $l = 2m$, the center of the top layer is a 4fh site, so for $l = 2m+1$ we choose the 4fh site closest to the center. Examples of clusters of both 3fh and 4fh sites are shown as insets in *Figure. 3.1*.

3.1. Comparison of Different Methods and Functionals

Table. 3.1 shows results of the adsorption energy, E_b determined with different methods and exchange-correlation functionals. The adsorption energy E_b is calculated by $E_b = E(\text{S} + \text{Cu}_n) - E(\text{Cu}_n) - E(\text{S}_2)/2$, where $E(\text{S} + \text{Cu}_n)$ is the total energy of the Cu cluster with a single S atom adsorbed, $E(\text{Cu}_n)$ is the total energy of the Cu cluster itself, and $E(\text{S}_2)$ is the

energy of a S_2 molecule in vacuum. For VASP calculations, the Gaussian smearing of width 0.02 eV is used. There is no smearing in NWChem calculations. Using the same PBE exchange-correlation functional, the difference between E_b obtained from plane-wave and Gaussian basis sets is generally within 0.10 eV, i.e., there is excellent agreement between the two approaches. This validation process is important, since medium to large size metal clusters are not the natural environment for either plane-wave or atomic basis set DFT codes. The agreement between the two different methods gives confidence that results presented below do not reflect numerical artifacts.

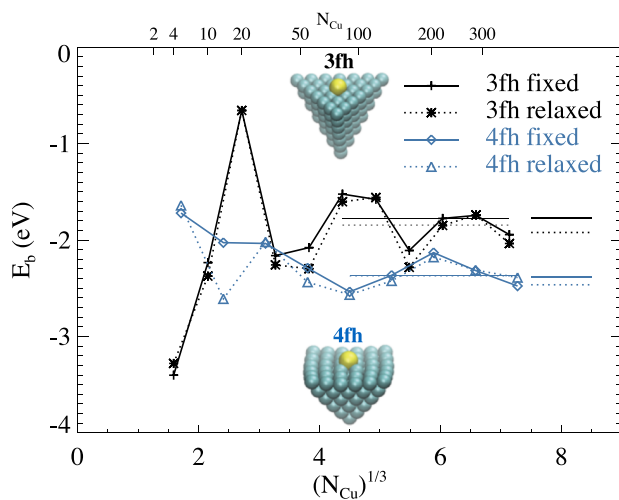


Figure 3.1 Adsorption energy of S on 3fh and 4fh sites, with fixed and fully relaxed substrates. The insets show S adsorbed on a 3fh site of an 84-atoms T_d cluster, and a 4fh site of a 91-atom O_h^2 cluster, with full geometric relaxation. Note the more significant relaxation of the O_h^2 cluster. The longer horizontal lines show the values of E_b averaging over results for the larger clusters. The shorter horizontal lines represent results obtained from slab calculations. See text for more details. Data for 3fh sites are taken from Ref. 17.

Results using the PBE0 and HSE06 functionals also generally agree well with the PBE results, the difference usually being within 0.1 eV. However, there are certain clusters (e.g., 30-atom O_h^2 , 20-atom T_d) where the difference is significantly larger. Also the consistency of results for PBE0 obtained with different Gaussian basis sets is not as good as

for PBE. The largest differences in the Gaussian basis sets show up in the 5-atom O_h^2 cluster and the 20-atom T_d cluster.

Table 3.1 Adsorption energy E_b (eV) of S on clusters of different shapes and sizes. PAW potentials and plane-wave basis set with energy cutoff of 280 eV are used for VASP. For NWChem, the superscripts a and b denote combinations of LANL2DZ/6-311++G(d,p) and def2-QZVP/def2-QZVPPD for Cu/S, respectively. Geometries of all clusters are from the VASP/PBE optimized structure.

N_{Cu}	PBE			HSE06		PBE0
	VASP	NW ^a	NW ^b	VASP	NW ^a	NW ^b
S on 4fh sites, O_h^2 clusters						
5	-1.717	-1.827	-1.872	-1.885	-2.048	-2.356
14	-2.001	-1.921	-2.054	-1.989	-2.018	-2.094
30	-2.001	-1.934	-2.146	-1.969	-2.311	-2.239
55	-2.322	-2.361		-2.357	-2.480	
91	-2.626	-2.554			-2.487	
S on 3fh sites, O_h^2 clusters						
4	-3.537	-3.825	-3.909	-3.931	-4.026	-4.081
10	-2.231	-2.349	-2.328	-2.403	-2.587	-2.555
20	-0.611	-0.564	-0.662	-0.350	-0.155	-0.425
35	-2.327	-2.442		-2.347	-2.417	
56	-2.160	-2.335		-2.261	-2.330	
84	-1.489	-1.551		-1.493	-1.647	

3.2. Comparison of 3fh vs 4fh Adsorption Energy vs Cluster Size

Figure 3.1 shows the adsorption energy E_b of S on 3fh sites on T_d clusters and 4fh sites on O_h^2 clusters of various sizes from VASP calculations. Two sets of data are calculated for each geometry. The first set, represented by solid lines in *Figure 3.1*, has the Cu atoms in

the cluster fixed at their bulk positions, allowing only the S atom to relax. The second set, represented by dotted lines, allows all atoms to relax. Results are obtained using the plane-wave basis set.

The somewhat surprising result in *Figure 3.1* is that not only is there a very large size dependence in E_b , but also the preference for 4fh over 3fh only emerges for very large clusters. For $N_{\text{Cu}} < 100$, E_b is very sensitive to the cluster size, and the variation with N_{Cu} dominates over any site preference. Even for $N_{\text{Cu}} > 100$, E_b can be very close for the two types of adsorption sites for clusters of similar sizes, although the preference towards 4fh sites does emerge as a trend.

Results with the fully relaxed clusters are mostly in line with the counterparts for a fixed substrate. For some of the smaller O_h^2 clusters, however, larger deviations are observed. This can be explained by the observation that the exposed (100) surface is much less thermodynamically stable and will sometimes reconstruct from the pristine (100) structure. Also for O_h^2 clusters, sometimes the clean and S-adsorbed clusters can relax into different shapes. For these occasions, we choose the more stable S-adsorbed configuration as the starting point and redo the calculation for the metal cluster with an S atom removed. In most cases, relaxation lowers the value of E_b slightly, although some exceptions can be found for S on 4fh sites of O_h^2 clusters.

As indicated in Sec. 1, by suitably averaging binding energies over a range of (larger) cluster sizes, one might be able to efficiently assess the adsorption behavior on extended surfaces. In general, binding energy displays quasi-periodic variation as a function of *linear* cluster size, which arises from the interference of the cluster boundaries and the electronic wave functions. Thus, it is natural and appropriate to average over a number of periods in

order to extract a limiting large-size behavior. We note that the period depends on the cluster geometry and indeed is different for our analysis of binding at 3fh versus 4fh sites. For 3fh sites, averaging over N_{Cu} from 84 to 364 which corresponds to roughly two periods of oscillation yields $E_b = -1.78 \pm 0.04$ eV for unrelaxed substrates and -1.84 ± 0.05 eV for relaxed substrates. The errors are estimated using the standard deviations of the data divided by the number of samples, thus reflecting the general expectation that by averaging a larger range of cluster sizes, one can better approach the limiting behavior. For 4fh sites, averaging over N_{Cu} from 91 to 385 which corresponds to roughly one period of oscillation yields $E_b = -2.36 \pm 0.03$ eV for unrelaxed substrates and -2.37 ± 0.03 eV for relaxed substrates. These results are shown in *Figure 3.1* as horizontal solid lines running through data points that are used for the averaging.

We also calculate independently the S adsorption energy using a periodic slab geometry. For the (100) surface, large oscillations in E_b as a function of the slab thickness are found. These are due to the 2D quantum confinement effect. *Appendix B* illustrates these effects through an analysis with (2×2) supercells (1/4 ML S coverage). To obtain bulk adsorption energies, we average over DFT results for slab thicknesses from 7 to 12 layers and obtain $E_b = -2.400 \pm 0.002$ eV with $\theta_S = 1/16$ ML for an unrelaxed substrate and $E_b = -2.468 \pm 0.006$ eV with $\theta_S = 1/20$ ML for a relaxed substrate. For the (111) surface, less thickness dependence is found, and we calculate the bulk adsorption energy by averaging slab thicknesses from 4 to 7 layers to obtain $E_b = -1.778 \pm 0.003$ eV with $\theta_S = 1/12$ ML for an unrelaxed substrate and $E_b = -1.926 \pm 0.004$ eV with $\theta_S = 1/16$ ML for a relaxed substrate. At the right side of *Figure 3.1*, we show the calculated E_b for fcc sites on Cu(111) and 4fh sites on Cu(100) with the periodic slab geometry. Consistent with the trend established for

large Cu clusters, S adsorption on the 4fh site is stronger than the 3fh site in the slab geometry calculations. Note that with averaging, the cluster results are completely consistent with the slab results for unrelaxed substrates, while some deviations exist for relaxed substrates.

Note that here we focus on 3fh and 4fh sites. For S on extended Cu surfaces, other adsorption sites are significantly less favorable. DFT-PBE calculations show that the adsorption of a sulfur atom on a bridge site is 0.95 eV weaker than the 4fh site on the Cu(100) surface. Adsorption on a top site is even less favorable, being 1.54 eV weaker than the fcc site on the Cu(111) surface. Thus bridge sites and top sites have negligible population.

We conclude this subsection with some remarks about the averaging procedure. In the free electron picture, the quasi-periodic behavior of E_b arises from interference of the wave functions reflected by cluster or slab boundaries. If one can make the linear size l of the system a continuous variable, e.g., using a jellium model, then E_b and other physical quantities can be described as piece-wise continuous curves, with periodicity $\lambda_F/2$ for $l \rightarrow \infty$,²⁸ where λ_F is the Fermi wavelength. For the averaging procedure to be effective, the phases of the data points on this oscillatory curve should be incoherent, or in other words, more or less evenly distributed among the hills and valleys of the curve. If this condition is satisfied, then the average will not be very sensitive to the range of sizes used and also approach the limiting value rather quickly. We find that this is generally true for the systems studied here. However, there are systems, e.g., (110) surfaces of coinage metals, where the phase incoherence requirement is not met.²⁹ In this case, the averaging procedure is not very

effective in eliminating the quantum size effect, even averaging over slabs of up to 12 layers.³⁰

3.3. Comparison of Bond Length for 3fh vs 4fh Adsorption Sites

Figure 3.2 shows the bond length between S and its nearest-neighbor Cu atoms from VASP for the of configurations as those in Figure. 3.1. Unlike the energy, the respective S–Cu bond lengths for S at the 3fh and 4fh sites converge rather quickly, basically reaching their bulk limits for $N_{\text{Cu}} > 100$. Furthermore, the bond length for S on 3fh sites is about 3% shorter than on 4fh sites. The convergence to the bulk value, as plotted at the right side of the figure, is also quite apparent. The asymptotic value of 0.229 nm for Cu–S bond length at the 4fh site is slightly larger than the 0.226 nm value obtained from an experimental photoemission study.³¹ This is consistent with the general level of accuracy of DFT/PBE.

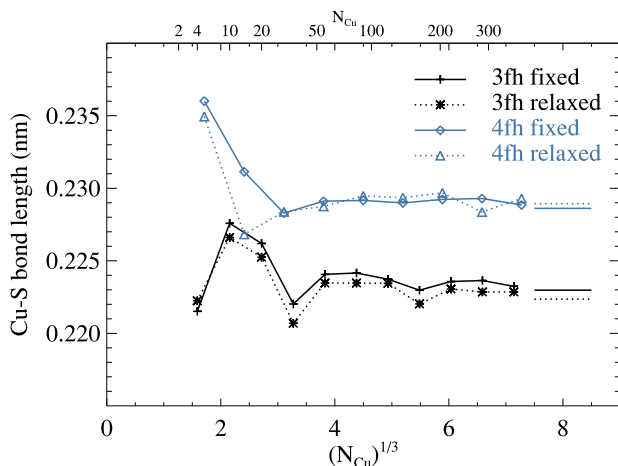


Figure 3.2 Average bond length of S on 3fh and 4fh sites, with fixed and fully relaxed substrates.

It is interesting to note that the bond length predicted by optimization of the S with a fixed substrate using the Gaussian basis sets of LANL2DZ (Cu) and 6-311++G(d,p) (S) is about 3.5% longer than the VASP prediction. This is likely due to the shortcomings of the 6-311++G(d,p) basis set for treating S. Using def2-QZVPPD for S instead predicts bond-

lengths which are only 0.5% longer than the VASP values. However, a combination of LANL2DZ and def2-QZVPPD results in an unbalanced description of the system, with a much larger basis set on S than on Cu, which causes overbinding. A combination of def2-QZVP (Cu) and def2-QZVPPD (S) gives good agreement with VASP results for both adsorption energy and bond lengths (see *Table 3.1*).

4. Effects of Broadening the Occupancy Function

As shown in Sec. 3, for an isolated cluster, quantum confinement of electrons introduces a correction to the large-size limit of the adsorption energy that does not decay exponentially with the system size. We also find that removing one or more atoms from the corners of a cluster can change the adsorption energy by as much as 0.4 eV for a cluster of about 100 atoms.¹⁷ As mentioned in Sec. 1, these features reflect a lack of locality of chemical bonding in metallic solids. In our case, the clusters consist of a few flat surfaces (together with some edges and corners), which can create coherent interference in the wave functions. Again, localization and thus minimization of size effects come from cancellation of the phase of Bloch waves which can be produced by introducing randomness into the system. Our proposal here is that by introducing such effects to reduce size dependence, we can more efficiently assess the energetics of the semi-infinite extended surface system. Further validation of this idea is provided below.

Specifically, in this section, we explore the technique of partial (or fractional) occupancy that has been implemented in many DFT codes as a way to introduce the above-mentioned phase cancellation. In real solid systems, the probability of occupancy of energy levels for electrons approaches that of a step function, but it is often more efficient numerically in solid state electronic calculations to broaden the step function (or, more exactly, the Fermi-Dirac distribution).³² The key physics is that the position of the Fermi

level, relative to the electronic band structure, is sensitive to the system size.²⁸ By adding noise to the exact position of the Fermi level, one can simulate randomness in a system. The smearing method, by broadening the occupancy function, adds uncertainty to the Fermi level and is thus a natural way to simulate “noisy” Fermi levels.

4.1. Adsorption Energy versus Cluster Size

Figure 3.3 shows E_b calculated for unrelaxed metal substrates with Gaussian smearing but deliberately choosing a larger smearing width σ than the default value 0.2 eV used in *Fig. 3.1*. The size dependence is greatly reduced, and the convergence to the limiting large-size value of $E_b = -1.78$ (-2.39) eV for 3fh (4fh) sites is more apparent. The larger the σ values, the smaller the extent of size dependence. The dramatic reduction in size dependence is consistent with the above stated proposal that enhanced smearing mimics the introduction of randomization to the system which in turn enhances localization. Ideally, the more readily assessed limiting large-size behavior evident from this analysis provides an efficient assessment of binding on a semi-infinite extended surface.

One caveat is that with large σ , the detailed form of the smearing becomes relevant. Using the Methfessel-Paxton (MP) scheme,³² for which the occupancy function approaches a step function faster than for Gaussian smearing as σ decreases, leads to somewhat different results for large σ . For example, using the first-order MP with $\sigma = 1.0$ eV, E_b on 4fh sites in O_h^2 clusters converges to -2.25 eV versus the -2.37 to -2.40 values obtained using the other three methods (averaging different cluster sizes, slab geometries, and Gaussian smearing with $\sigma = 1.0$ eV). For 3fh sites, the MP smearing with $\sigma = 1.0$ eV yields $E_b = -1.63$ eV, versus the -1.78 eV value obtained using the other methods. We conclude that Gaussian smearing is more appropriate for our purposes here.

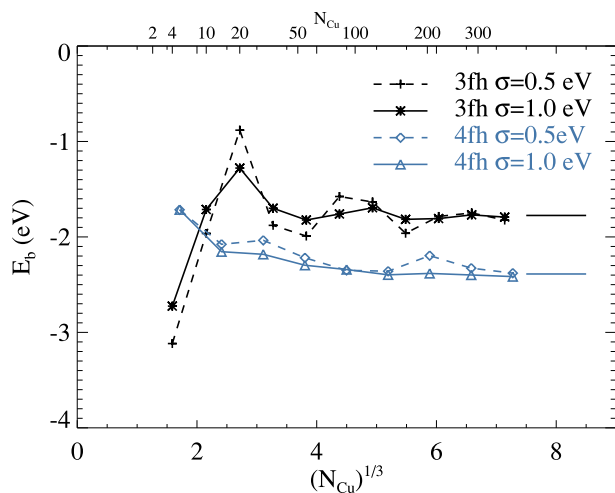


Figure 3.3 The adsorption energy E_b as a function of the cluster size, with Gaussian smearing of the occupancy function with widths 0.5 eV and 1.0 eV. The two short horizontal lines represent the corresponding slab geometry calculation results, with frozen substrates.

Strictly speaking, even with Gaussian smearing, different σ values will lead to a different limiting behavior, and the physically relevant value should correspond to the limit of $\sigma \rightarrow 0$. With slab geometries and a relatively small (2×2) supercell, we find that between $\sigma = 0.2$ and 1.0 eV, the values of E_b for S/Cu(100) do deviate, but the differences are relatively small (about 0.025 eV). For S/Cu(111), on the other hand, the change due to σ is within numerical uncertainties. The optimal choice of the form and width of the smearing function is an open question at this stage.

4.2. Site-projected Density of States Analysis

Perhaps more important than potentially providing a more efficient method to estimate E_b for S on extended Cu surfaces from cluster calculations, we can also use the smearing of the occupancy function to elucidate the difference between the bonding of S in 3fh and 4fh sites. One way to visualize interactions between S and a cluster is through plotting the site-projected density of states (SDOS's) of individual atoms. *Figure 3.4* shows the SDOS localized on the S on the center 4fh site of a 91-atom O_h^2 cluster, obtained using

Gaussian smearing of different widths σ . With a small σ , the SDOS consists of many sharp spikes, each of which corresponds to one or more molecular orbitals. (As an aside, analogous sharp spikes appear in the SDOS for slab calculations.) The highly complex SDOS, especially near the Fermi level, is directly responsible for the large size dependence of binding seen in Sec. 3.1. It also makes it more difficult to obtain an intuitive picture of chemical bonding. By widening the smearing, a smoother SDOS can be achieved, which facilitates interpretation of bonding. It is significant to note that Feibelman⁶ also used Gaussian-smearing of the DOS to obtain insights into Cu–S clusters on Cu(111) surfaces. In his case, the DOS was projected onto Cu atoms and his analysis used slab (rather than cluster) geometries.

The solid line in *Fig. 3.5* shows the SDOS of a S atom on the 3fh site of a T_d cluster with 56 Cu atoms, with Gaussian smearing of 1.0 eV. Analysis of the electronic structures using the crystal orbital Hamilton population (COHP) method³³ shows that the peaks near -17 and -8 eV are mostly bonding, and the peak near -5 eV is mostly antibonding. (Note that in *Fig. 3.5* the energy is relative to the reference configurations of individual atoms, rather than the Fermi energy as is the usual practice in solid state physics as in *Fig. 3.4*. This is done in order to make the comparison between S on different adsorption sites more transparent.) The dashed line is for an S atom on a 4fh site of the (100) face of a O_h^2 cluster with 91 Cu atoms. Compared with S on the 3fh site, the main difference in the SDOS is that the antibonding states are more spread out. This results in a higher Fermi energy, E_F , which in turn forces the bonding state deeper below the Fermi level, thus increasing the strength of binding. Thus the difference between S adsorption on the 4fh site and the 3fh site can be understood intuitively in the following way: on a 4fh site, with more neighboring Cu atoms,

the S does not have to be as close to the Cu atoms as on the 3fh to maximize the bonding coupling between the S and Cu orbitals. This in turn leads to much smaller antibonding coupling between the S and Cu atoms, which is due to the faster decay of the antibonding interactions as the separation increases. Note that the linear sizes l for the two types of clusters shown in *Fig. 3.5* are the same, and there can be less perfect matches when choosing different clusters. Nevertheless, the qualitative picture remains the same.

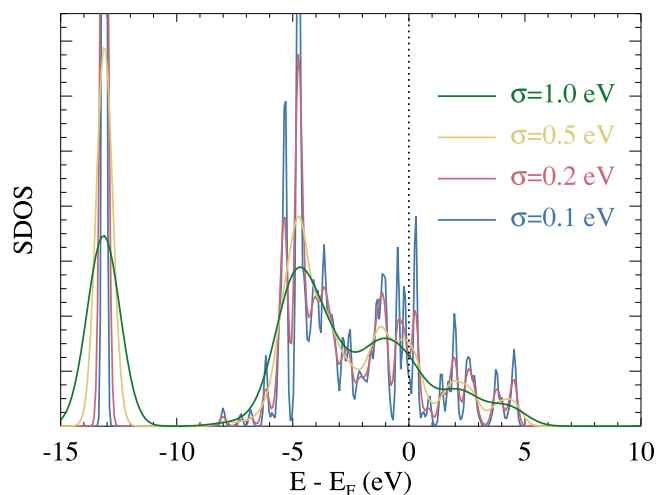


Figure 3.4 Effects of smearing widths on SDOS for an S atom on a 4fh site in a O_h^2 cluster with 91 Cu atoms. Here the energies are shown relative to the Fermi energy, in contrast to *Fig. 3.5*.

5. Discussion and Conclusion

Good agreement has been achieved between DFT codes employing plane-wave and Gaussian basis sets, regarding the adsorption of S on Cu clusters of various sizes. However, we find that the large size-dependence in the adsorption energies makes it challenging to estimate the limiting value of binding on an extended surface, and the associated delocalization makes it challenging to elucidate the nature of chemical bonds between the S adsorbate and the metal cluster. It has been long recognized that for small clusters (less than 50 atoms), the discreteness of the orbitals, especially the HOMO-LUMO gap, will lead to a

behavior quite different from their bulk counterpart. Another issue, which is familiar in condensed matter physics, is that for an isolated cluster, interference of wave functions from the boundaries will lead to corrections that do not decay exponentially. For Cu clusters, the adsorption energy can be significantly affected (up to 0.6 eV) by what happens 1.5 nm away from the adsorption site.

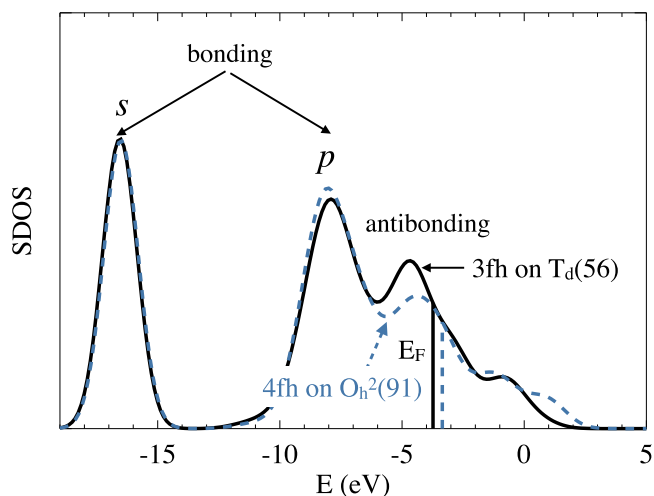


Figure 3.5 Site-projected density of states (SDOS) of a S atom on a 3fh site of a T_d cluster with 56 Cu atoms (solid line), and a S atom on a 4fh site of a O_h^2 cluster with 91 atoms (dashed line). Gaussian smearing of width 1.0 eV is used. Energy is relative to individual atoms, rather than the Fermi energies, which are plotted as two distinct vertical lines. There are two broad peaks for bonding orbitals, from the sulfur s and p electrons respectively.

A natural question is then, how can calculations on small to medium size clusters be relevant to adsorption on extended single-crystal surfaces? A simple but effective method is to average over results for clusters over a suitable range of sizes (as described in Sec. 3). One could anticipate similar results from suitably averaging over different shapes, or by performing analysis for clusters with rough side surfaces. Another strategy which is particularly efficient for plane-wave methods is to utilize the partial occupancy technique which was originally developed for numerical efficiency. By choosing an appropriate

smearing function (e.g., Gaussian), we can reliably assess binding on extended surfaces from calculations on medium size clusters.

By averaging contributions from different orbitals, we can understand the adsorption of S on metal clusters in a way that is both intuitive and also rests on firm quantitative grounds. We suggest that the stronger binding of S to 4fh sites is due to the weaker antibonding interactions compared with 3fh, while having similar bonding interactions. This interpretation of chemical bonds as a competition between bonding and antibonding interactions through interference energies, as advocated a long time ago by Ruedenberg,³⁴ is key to understanding the site preference of simple adsorbates.

Acknowledgments

J.S.B., J.L., T.L.W., J.W.E., and D.J.L. performed the computations in this work and were supported for this work by the U.S. Department of Energy (USDOE), Office of Basic Energy Sciences, Division of Chemical Sciences, Geosciences, and Biosciences through the Ames Laboratory Chemical Physics program. Use of NERSC computational resources is acknowledged. PAT provided experimental insights into key issues for S adsorption systems and was supported for this work by NSF Grant No. CHE-1507223. The work was performed at Ames Laboratory which is operated for the USDOE by Iowa State University under Contract No. DE-AC02-07CH11358.

References

1. M. Foss, R. Feidenhans'l, M. Nielsen, E. Findeisen, T. Buslaps, R. L. Johnson, and F. Besenbacher, *Surf. Sci.* **388**, 5 (1997).
2. D.-J. Liu, H. Walen, J. Oh, H. Lim, J. W. Evans, Y. Kim, and P. A. Thiel, *J. Phys. Chem. C* **118**, 29218 (2014).
3. H. Walen, D.-J. Liu, J. Oh, H. Lim, J. W. Evans, Y. Kim, and P. A. Thiel, *J. Chem. Phys.* **142**, 194711 (2015).

4. M. Foss, R. Feidenhans'l, M. Nielsen, E. Findeisen, R. L. Johnson, T. Buslaps, I. Stensgaard, and F. Besenbacher, *Phys. Rev. B* **50**, 8950 (1994).
5. S. M. Russell, Y. Kim, D.-J. Liu, J. W. Evans, and P. A. Thiel, *J. Chem. Phys.* **138**, 071101 (2013).
6. P. J. Feibelman, *Phys. Rev. Lett.* **85**, 606 (2000).
7. D. R. Alfonso, A. V. Cugnini, and D. S. Sholl, *Surf. Sci.* **546**, 12 (2003).
8. H. Walen, D.-J. Liu, J. Oh, H. Lim, J. W. Evans, C. M. Aikens, Y. Kim, and P. A. Thiel, *Phys. Rev. B* **91**, 045426 (2015).
9. D.-J. Liu, *Phys. Rev. B* **81**, 035415 (2010).
10. T. M. Soini and N. Rösch, *Phys. Chem. Chem. Phys.* **17**, 28463 (2015).
11. C. Edmiston and K. Ruedenberg, *Rev. Mod. Phys.* **35**, 457 (1963).
12. *Electronic Structure of Alloys, Surfaces, and Clusters*, edited by A. Mookerjee and D. D. Sarma (Taylor & Francis, London, 2003).
13. N. Marzari, A. A. Mostofi, J. R. Yates, I. Souza, and D. Vanderbilt, *Rev. Mod. Phys.* **84**, 1419 (2012).
14. G. Kresse and J. Hafner, *Phys. Rev. B* **47**, R558 (1993).
15. G. Kresse and J. Furthmüller, *Comput. Mater. Sci.* **6**, 15 (1996).
16. M. Valiev, E. Bylaska, N. Govind, K. Kowalski, T. Straatsma, H. van Dam, D. Wang, J. Nieplocha, E. Apra, T. Windus, and W. de Jong, *Comput. Phys. Commun.* **181**, 1477 (2010).
17. J. S. Boschen, J. Lee, T. L. Windus, J. W. Evans, and D.-J. Liu, *J. Phys. Chem. C* **120**, 10268 (2016).
18. J. P. Perdew, K. Burke, and M. Ernzerhof, *Phys. Rev. Lett.* **77**, 3865 (1996); Erratum **78**, 1396 (1997).
19. C. Adamo and V. Barone, *J. Chem. Phys.* **110**, 6158 (1999).
20. J. Heyd, G. E. Scuseria, and M. Ernzerhof, *J. Chem. Phys.* **118**, 8207 (2003); Erratum **124**, 219906 (2006).
21. G. Kresse and D. Joubert, *Phys. Rev. B* **59**, 1758 (1999).

22. P. J. Hay and W. R. Wadt, *J. Chem. Phys.* **82**, 270 (1985).
23. A. D. McLean and G. S. Chandler, *J. Chem. Phys.* **72**, 5639 (1980).
24. R. Krishnan, J. S. Binkley, R. Seeger, and J. A. Pople, *J. Chem. Phys.* **72**, 650 (1980).
25. T. Clark, J. Chandrasekhar, G. W. Spitznagel, and P. von Ragué Schleyer, *J. Comput. Chem.* **4**, 294 (1983).
26. F. Weigend and R. Ahlrichs, (2005). *Phys. Chem. Chem. Phys.* **7**, 3297
27. D. Rappoport and F. Furche, *J. Chem. Phys.* **133**, 134105 (2010).
28. F. K. Schulte, *Surf. Sci.* **55**, 427 (1976).
29. Y. Han and D.-J. Liu, *Phys. Rev. B* **80**, 155404 (2009).
30. H. Walen, D.-J. Liu, J. Oh, H. J. Yang, Y. Kim, and P. A. Thiel, *J. Phys. Chem. C* **119**, 21000 (2015).
31. C. C. Bahr, J. J. Barton, Z. Hussain, S. W. Robey, J. G. Tobin, and D. A. Shirley, *Phys. Rev. B* **35**, 3773 (1987).
32. M. Methfessel and A. T. Paxton, *Phys. Rev. B* **40**, 3616 (1989).
33. R. Dronskowski and P. E. Blöchl, *J. Phys. Chem.* **97**, 8617 (1993).
34. K. Ruedenberg, *Rev. Mod. Phys.* **34**, 326 (1962).

Appendix A. Modified Adsorption At and Near Steps

On fcc(111) surfaces, the so-called A-step creates microfacets resembling the (100) surface locally. Thus adsorption of S along an A-step may be akin to adsorption on a 4fh site. In order to study this via the cluster approach, we create steps on top of a cluster by adding an incomplete layer, or an island, on one face of the cluster. In *Fig. 3.6*, we consider two types of A-steps, one formed by an island that has its boundary as close as possible to the edge of the cluster, thus exposing a step edge with length $l - 2$ on a cluster with side length l . Note that the larger island with side length $l - 1$ consists of Cu atoms on hcp sites, rather than fcc sites. DFT-PBE results for S adsorption along this kind of step edge are shown in *Fig. 3.6*

as the black pluses. The average result for clusters with $l = 8-12$ is -2.52 eV, which is slightly lower than the equivalent value of -2.36 eV for the 4fh site on the (100) surface (Sec. 3 and *Fig. 3.1*). The other type of step has one row of Cu atoms removed from the island in the first type, thus one of the step edges is further removed from the edge of the cluster. See insets of *Fig. 3.6* for illustrations. Results for S adsorption on these types of steps are shown in *Fig. 3.6* as red asterisks. The average value for $l = 8-12$ is -2.09 eV, which lies between -1.77 eV (3fh) and -2.36 eV (4fh) obtained in Sec. 3. Therefore, the expectation that A-steps on Cu(111) are more favorable adsorption sites than flat terraces are met, although some differences are found depending on configurations further away from the step edges.

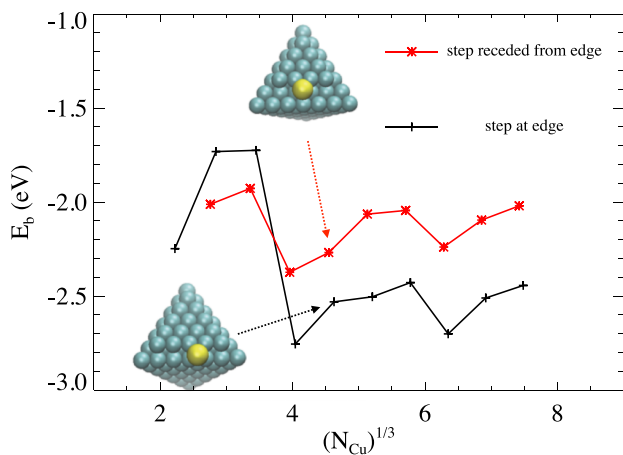


Figure 3.6 Adsorption energy E_b for S at step edges. The pluses (connected by a black line) are for steps right on the edge, and the asterisks (connected by a red line) are for steps receded from the edge by one row of atoms.

Appendix B. Dependence of The Adsorption Energy on The Slab Thickness

Here, we quantify how the S adsorption energy depends on the thickness of the slab in calculations with semi-infinite slab geometries. *Table 3.2* lists the adsorption energy E_b for S on Cu(100) and Cu(111) surfaces, calculated using slabs of different thicknesses measured by the number of layers L . All atoms are allowed to relax except for the bottom layer of Cu

atoms. Also listed are the average value $\langle E_b \rangle$ and the standard deviation δE_b for each L calculated using data up to L . For example, for $L=12$, we use data from 7 to 12. While the extent of variations using slabs is much smaller than results using clusters, the convergence to the bulk limit is also slow. Also note that variations of a few meV can be due to numerical errors.

Table 3.2 Adsorption energy E_b , average value $\langle E_b \rangle$, and standard deviation δE_b (in eV) for S on Cu(100) and Cu(111) with different slab thicknesses L , all with (2×2) supercells and $(24 \times 24 \times 1)$ k -point grid.

L		1	2	3	4	5	6	7	8	9	10	11	12
	E_b	-2.733	-2.457	-2.340	-2.450	-2.404	-2.398	-2.424	-2.406	-2.436	-2.426	-2.420	-2.429
Cu(100)	$\langle E_b \rangle$				-2.395	-2.398	-2.417	-2.419	-2.408	-2.414	-2.418	-2.418	-2.423
	δE_b				0.078	0.055	0.028	0.023	0.011	0.016	0.015	0.014	0.010
	E_b	-1.252	-1.953	-1.842	-1.871	-1.854	-1.875	-1.861	-1.859	-1.859	-1.859	-1.849	-1.860
Cu(111)	$\langle E_b \rangle$				-1.857	-1.856	-1.867	-1.866	-1.863	-1.862	-1.863	-1.861	-1.858
	δE_b				0.021	0.015	0.011	0.009	0.009	0.008	0.007	0.008	0.004

CHAPTER 4. STABILIZATION OF X–AU–X COMPLEXES ON THE Au(111) SURFACE: A THEORETICAL INVESTIGATION AND COMPARISON OF X = S, Cl, CH₃S, AND SiH₃S

A paper published in and reprinted with permission from

The Journal of Physical Chemistry C virtual special issue “Mark S. Gordon Festschrift”
2017, 121, 3870-3879

Jiyoung Lee,^{a,b} Jeffery S. Boschen,^{a,b} Theresa L. Windus,^{a,b} Patricia A. Thiel,^{a,b,c} and Da-
 Jiang Liu^{a,*}

^a*Ames Laboratory – USDOE, Iowa State University, Ames, IA 50011, USA*

^b*Department of Chemistry, Iowa State University, Ames, IA 50011, USA*

^c*Department of Materials Science & Engineering, Iowa State University, Ames, IA 50011, USA*

**Corresponding author*

Abstract

Stabilities of linear X–Au–X complexes on the Au(111) surface, with different ligands X = S, Cl, CH₃S, and SiH₃S, are studied using density functional theory (DFT). For X = CH₃S and SiH₃S, AuX₂ complexes are more stable compared with the configuration where X are individually chemisorbed and Au is incorporated into the bulk. AuS₂ complexes, however, are less stable than chemisorbed S. The relative stability of AuCl₂ complexes depends on the functionals used. Bond strengths of the X–Au–X complexes in the gas phase are calculated by using DFT and the coupled cluster method and found to be similar. This implies that the stabilities of adsorbed complexes are controlled by the bond strength of the ligand to the surface. These results explain why complexes with X = CH₃S and sometimes Cl are observed on Au(111), whereas complexes with X = S are not.

1. Introduction

The interaction between sulfur and the surface of gold is central to a major technique of surface modification that consists of anchoring organic molecules (especially alkanethiols and their derivatives) to gold surfaces through the sulfur atom.¹⁻⁴ This technique is quite versatile, and there are many applications of such functionalized surfaces, both real and potential. These range from detection of antibiotic-resistant bacteria⁵ to fabrication of thin film transistors or even as components of single-molecule transistors.^{6,7} The plasmonic properties of Au also greatly enhance the range of possible uses.⁸ At the same time, there is evidence that sulfur can form complexes with preexisting metal atoms on coinage metal surfaces.⁹⁻¹² More recently, a study with scanning tunneling microscopy (STM) has shown that S can change the surface reconstruction of Au surfaces.¹³ There is gathering evidence that alkanethiols can perturb the positions of Au atoms in the surface layer.¹⁴ There is also great interest in thiolate covered gold nanoclusters where novel catalytic properties can be found, due to either interactions between gold and sulfur or new configurations stabilized by thiolates, which are used in both synthesis and protection of the nanoclusters.¹⁵

In this paper, we focus on X–Au–X complexes on Au(111), where X can be S, Cl, CH₃S (methanethiolate), or SiH₃S (silanethiolate). Our choice is motivated by the fact that experimental data exist for the first three of these adsorbates.¹⁶⁻¹⁸ Even though the data originated from three different laboratories, the experiments were done under similar conditions and at low adsorbate coverages. Specifically, adsorption occurred at room temperature, thus ensuring dissociation of the parent gas-phase species (e.g., Cl₂ or CH₃SH), followed by cooling to 5 K for STM imaging. In all cases, local islands of adsorbate formed in which the Au(111) reconstruction was lifted, surrounded by reconstructed areas where adsorbate coverage was essentially zero. [The unit of coverage is monolayers (ML), defined

as the density of adsorbate atoms relative to the density of Au atoms in unreconstructed Au(111).] The local coverage in the adsorbate islands was 0.07 ML for S,¹⁶ 0.02 ML for Cl,¹⁷ and 0.14–0.18 ML for CH₃S.¹⁸ (The value for CH₃S is based upon evaluation of published STM images.) Under these conditions, only CH₃S forms a X–Au–X complex; S and Cl exist as atomic adsorbates. We should also note that there are extensive experiments with higher coverages.^{19–21}

Our goal in this paper is to understand why one adsorbate forms a complex, whereas the other two do not at low coverages. We ask whether this is attributable primarily to different stabilities of the isolated (gas-phase) complexes themselves or to the interactions of ligands with the surface. The comparison of different ligands allows us to comment on how the chemistry of the adsorbate determines the stability of the complex. The fourth adsorbate, SiH₃S, is added to broaden the range of comparisons. Computational details are given in section 2. Results for adsorption of ligands on the Au(111) surface are given in section 3, and the results for gas-phase AuX₂ are given in section 4. We conclude that the stability of AuX₂ complexes is determined by competition between the binding of X to the surface and the binding of AuX₂ complexes themselves. The study shows that while at the GGA level, DFT can be useful to understand the energetics, more complete agreement with experiments requires at least meta-GGA treatments.

2. Computational Details

2.1 Bulk and Surface.

DFT calculations using plane-wave basis sets are carried out using the VASP package (v5.3 and v5.4).^{22,23} The Au(111) surface is modeled by periodic slabs separated by 12 Å of vacuum. Most of the calculations are performed using the PBE functional,²⁴ with theoretical lattice constant 4.158 Å determined by quadratic fitting of bulk calculations with (24 × 24 ×

24) k-points grid and a 280 eV energy cutoff. A higher 400 eV cutoff is also used for validation. Lattice constants obtained using other functionals are reported in section 3.5. The experimental value for Au is 4.078 Å.

We systematically investigate the energetics of adsorption on unreconstructed Au(111) using the following steps. Step 1: Determine the most favorable adsorption configuration for an isolated adsorbate using a moderate size supercell so that adspecies interactions are not too significant. Step 2: Determine the “baseline” adsorption energies by placing one adsorbate in various surface supercells to form a regular hexagonal lattice. The surface area for those supercells, N_A [expressed as multiples of the primitive (1×1) unit cell], can be 1, 3, 4, 7, 9, 12, 13, etc. When N_A is a multiple of 3, we also put an extra adsorbate with a displacement of $(a_1/3 + a_2/3)$ from the original adsorbate, where a_1 and a_2 are the surface supercell lattice vectors. The extra adsorbates are on equivalent adsorption sites as the original adsorbates and together form a regular honeycomb array. See insets in *Figure 4.2* where Cl atoms form a hexagonal (at 1/3 ML) and a honeycomb (at 2/9 ML) lattice. The adsorbates and the metal substrate are allowed to relax except for the atoms at the bottom layer which are frozen. The adsorption energy E_X^b can be calculated from DFT calculations using

$$E_X^b = [E(\text{slab} + X_n) - E(\text{slab})]/n - E(X_g) \quad (1)$$

where $E(\text{slab})$ is the energy of the clean slab and $E(\text{slab} + X)$ is the energy of the slab with n X per supercell. Although in thermochemistry the convention is to use the most stable elemental form (such as $\text{Cl}_{2,g}$) as the reference energy, in this paper, to address the systematic trend between different X, we use the energy of a single ligand $E(X_g)$ in the gas phase as the reference.

In general, the adsorption energy E_X^b is sensitive to the coverage of the adsorbates θ_X . Abufager et al.²⁵ show that when E_X^b is plotted as a function of $1/\theta_X$, the straight line between any two data points represents the average adsorption energy if the system is phase separated into two regions that consist of the two phases represented by the two end points. One can then choose the baseline energy at a given coverage as the value on the convex hull on the $(E_X^b, 1/\theta_X)$ plane. It is also common in literature to define the formation energy as $E^f = \theta_s E(\theta) - (\theta_s - \theta)E(0) - \theta E(\theta_s)$ where $E(\theta)$ is the surface energy with adsorbate coverage θ [so $E(0)$ is the energy of a clean surface], and θ_s is a certain saturation coverage which is usually taken to be 1 ML.²⁶ Though plotting E^f versus θ has the advantage that different configurations can be conveniently represented in a finite domain, the physical meaning of E^f is obscured, partly due to the fact that the saturation configuration is not always well- defined. In this paper, we plot all energies in the $(E_X^b, 1/\theta_X)$ plane.

Step 3 is the calculation of Au–X complexes on the gold surface. In this paper, we only consider the linear X–Au–X complexes formed by two ligands X and a Au adatom as they are found to be the most prevalent motif. We compare the energetics with the baseline values and determine whether these structures are viable in experiments. Because these complexes involve Au adatoms, one needs to account for the energy cost of extracting them from the surface. Here we assume that there is an unlimited source of adatoms from the steps and kinks on the surface, and the free energy $E - TS$ per Au adatom μ_{Au} is the same as the bulk cohesive energy in the limit of $T \rightarrow 0$. Thus, we define the chemical potential of X in a $Au_m X_n$ complex as

$$\mu_X = [E(\text{slab} + Au_m X_n) - E(\text{slab}) - m\mu_{Au}] / n - E(X_g) \quad (2)$$

In the case of $m = 0$, i.e., no Au adatom involvement, μ_X simply reduces to E_X^b , the adsorption energy.

A note on obtaining μ_{Au} from DFT calculations: though one can use the cohesive energy E_c from bulk calculations, we find that, for relatively thin slabs, the effective μ_{Au} can be significantly different from the bulk limit. For each supercell, we use the average change in energy per metal atom, $(E_L - E_{L-1})/N_A$ (where E_L is the energy of a clean slab with L layers) as μ_{Au} . It is important to calculate individually μ_{Au} for each supercell using the same k -point grid as the one used in calculating the first two terms in eq (2). Much faster convergence can be achieved this way. Results are then averaged over $L = 4-7$ (or $L = 3-5$ for the more demanding hybrid functionals).

2.2. Gas Phase

Binding energies of isolated AuX_2 complexes are calculated using the NWChem²⁷ software at the DFT level with PBE,²⁴ PBE0,²⁸ and M06²⁹ functionals. To compare with the planewave results, geometries of the AuX_2 complexes were optimized at the PBE level using three different basis sets: DZ is the Los Alamos National Laboratory double- ζ (LANL2DZ) with effective core potentials (ECP's)³⁰⁻³² for Au, TZ is the larger def2-TZVP³³ for Au and 6-311++G(d,p)³⁴⁻³⁶ for all other atoms, and QZ is the def2-QZVP³³ basis sets for Au and def2-QZPPD for all other atoms.³⁷ The optimized geometries using these different basis sets did not change much. To understand how spin contamination can affect the geometry and energy, restricted open-shell DFT (RODFT) and unrestricted DFT (UDFT) calculations are performed with the PBE functional using the DZ/TZ (meaning DZ for Au and TZ for all other elements). Again, the geometries and relative energies changed very little. So, only RODFT was used for other levels of theory. Additional geometry and energy calculations

were performed at the PBE0 and M06 level for comparison. To benchmark the DFT results, unrestricted coupled cluster CCSD(T) (UCCSD(T))³⁸⁻⁴¹ calculations are performed with the aug-cc-pVNZ-PP⁴² basis set for Au and aug-cc-pVNZ^{43,44} (N = D, T) for S, H, C, Cl, and Si using a restricted open shell Hartree–Fock (ROHF) reference wave function. The AuS₂ and AuCl₂ structures were reoptimized using UCCSD(T) and the DZ/TZ basis set, and binding energies at those geometries are calculated also using QZ/QZ basis sets. The geometries at the PBE TZ/QZ level are used for the larger two complexes. To obtain better binding energies, a two-point extrapolation to the complete basis set (CBS) limit is performed using the simple formula obtained by Halkier et al.:⁴⁵

$$E_{xy}^{\infty} = \frac{E_x^{corr} x^3 - E_x^{corr} y^3}{x^3 - y^3} \quad (3)$$

where x and y are cardinal number of basis set (D = 2, T = 3, Q = 4, etc.), $E_{x(y)}^{corr}$ is the correlation energy with the cardinal number $x(y)$, and E_{xy}^{∞} is the large basis set limit of the correlation energy. In this work, we extrapolated UCCSD(T) results with the aug-cc-pVDZ and aug-cc-pVTZ basis sets. Ideally, one would like to use the aug-cc-pVTZ (PP) and aug-cc-pVQZ (PP) basis sets for this extrapolation, results for the latter basis set are not available due to high computational expense. It is still useful, however, to perform extrapolation using the smaller basis set.⁴⁶ Ultimately, we are interested in the trends of the binding energies and this level of theory should be good for that purpose.

All complexes are in a doublet state and their geometries are optimized with tight convergence criteria as defined in NWChem. For DFT calculations, the number of radial grid points is 99 and the number of angular points in the Lebedev grid is 590.

3. Adsorption of S, Cl, CH₃S, and SiH₃S on Au(111)

3.1. S on Au(111).

Figure 4.1 shows the chemical potential obtained using the PBE functional²⁴ for some structures of adsorbed S on Au(111), and in comparison with the baseline, which decreases significantly as the coverage decreases due to elastic interactions due to adsorbate induced distortion of the substrate.^{16,25} The only structure on this plot that shows lower chemical potential than the baseline is the row-like structure with S atoms separated by $\sqrt{3}a$ (where $a = a_0/\sqrt{2}$ is the surface lattice constant for a fcc crystal with a bulk lattice constant a_0), which are, in fact, found by low temperature STM experiments¹⁶ and will be referred to collectively as a $\sqrt{3}$ -row structure. *Figure 4.1* also shows a chemisorbed zigzagging row-like structure with periodicity $\sqrt{7}a$, but now with two S atoms in each period, one close to a fcc site, and the other close to a hcp site (denoted as $\sqrt{7}$ -row). Another structure shown in the figure is the S–Au–S complex. For S/Au(111), we find that the most stable configuration for the AuS₂ complex has the Au atom on a top site, and the two S atoms near bridge sites (hence denoted as bridge-top-bridge or b-t-b). The S chemical potentials μ_S for this configuration at various θ_S are plotted in *Figure 4.1*, and all are about 0.2 eV above the baseline, indicating that there is no thermodynamic driving force for their formation on the Au(111) surface. The AuS₂ complexes can assume other configurations, with energetics sometimes similar to those of the b-t-b configuration shown here. We will discuss those in more detail in section 3.5.

3.2. Cl on Au(111).

Figure 4.2 shows the PBE chemical potentials for Cl on Au(111). We note first that the baseline is not as deep as S/Au(111), suggesting a weaker interaction between Cl on fcc sites. Three different types of structures are found to be below the baseline when the coverage is low enough. The $\sqrt{3}$ -row and the $\sqrt{7}$ -row structures have been observed by

STM.^{17,47} The $\sqrt{3}$ -row structure is very similar to that for S/Au(111), whereas the $\sqrt{7}$ -row structure has the Cl alternately occupying fcc and bridge sites. An alternative fcc-hcp structure is unstable. This is in agreement with the conclusion Zheltov et al. drew from the STM evidence and is also consistent with their DFT study.¹⁷ As demonstrated in ref 17, the stability of the chainlike structures is due to indirect elastic interactions between adsorbates. By placing a pair of Cl in each supercell, Zheltov et al. show that there is no significant attractive pairwise interaction between Cl on fcc sites. Our own calculations confirm this conclusion. However, *Figure 4.2* shows the μ_{Cl} for infinitely long chains, both the $\sqrt{3}$ -row and the $\sqrt{7}$ -row structures are more stable than the baseline at low Cl coverage. This indicates that pairwise interactions are insufficient to describe structures of Cl on Au(111), as we have shown previously for S/Au(111),¹⁶ where trio interactions are important.

The most stable Cl–Au–Cl complex that we have found has the top-bridge-top (t-b-t) configuration (see section 3.5 for other configurations). The structure is elongated along directions 30° to the close-packed directions. The complexes are slightly energetically more favorable when they form a stripe, with 30° to the high symmetry direction. This structure is again in excellent agreement with recent STM experiments.²⁰ However, there is an apparent contradiction in the predicted coverage. The DFT-PBE results in *Figure 4.2* show AuCl₂ complexes are more stable than chemisorbed Cl at all coverages investigated, whereas experiments²⁰ show AuCl₂ complexes only at Cl coverages above 1/3 ML. One possible explanation is that the PBE functional may not be totally reliable in cases involving extraction of Au atoms from the bulk. Results with other functionals for this and other AuX₂ complexes are given in section 3.5, which show that the stability of AuCl₂ complexes is reduced with functionals that predict stronger bulk cohesive energies.

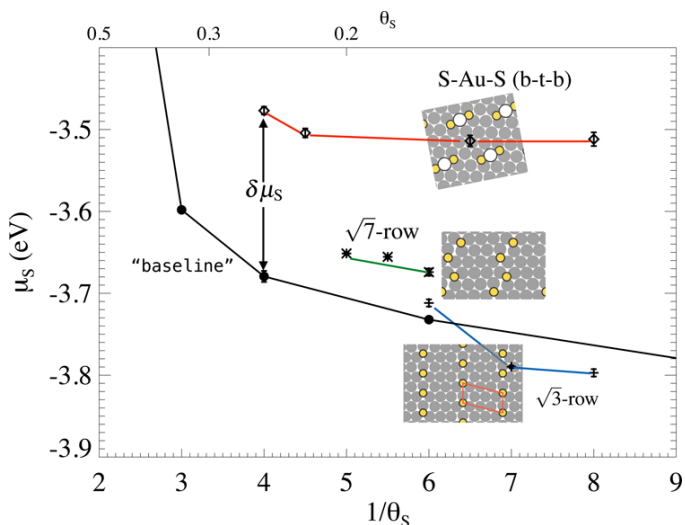


Figure 4.1 Stability as measured by the chemical potential of S of various structures on Au(111) versus the baseline. The black solid line is the baseline energetics of chemisorbed S forming triangular arrays. Representatives of the $\sqrt{3}$ -row (blue line), $\sqrt{7}$ -row (green line), and AuS₂ complexes (red line) are given as insets.

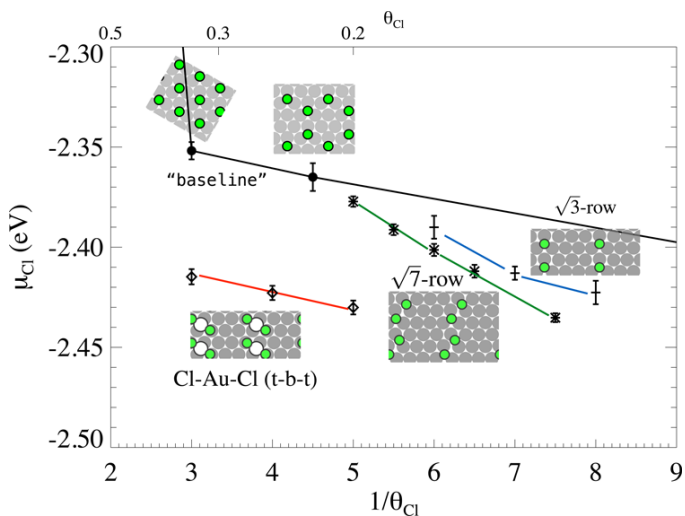


Figure 4.2 Stability as measured by the chemical potential of Cl of various structure on Au(111) versus the baseline, which consists of chemisorbed Cl at $2/3$, $1/3$, $2/9$, and $1/12$ ML for this plot (although only two data points are visible). Notations of other structures are similar to those in Figure 4.1.

3.3. CH₃S on Au(111).

Figure 4.3 shows the PBE chemical potentials for various CH₃S (denoted henceforth as RS) configurations on Au(111). The striking feature is that the RS–Au–SR complex is much more stable (over 0.2 eV per RS group) than the baseline. The RS–Au–SR complex

shown in *Figure 4.3* has a trans structure that is about 0.05 eV more favorable than the cis structure from our PBE calculations. Note that this conclusion is for well-separated stripes, and the behavior with different supercells can be different.^{48,49} The two S base atoms and the Au atom again form a linear S–Au–S motif, with a t-b-t configuration similar to that of the AuCl₂ complex rather than the b-f-b AuS₂ complex. This is consistent with the combined STM and DFT study of Maksymovych and co-workers.^{18,50,51} In ref 50 the RS in a RS–Au–SR complex is shown to bind to the surface 0.52 eV more strongly than a chemisorbed RS, which differs from our results. However, their way of determining stability does not take into account the cost of forming the Au adatom. The formation energy of a Au adatom in our DFT-PBE calculations is around 0.62 eV, or 0.31 eV per RS. After this extra energy cost is taken into account, the DFT value in ref 50 is consistent with our result here.

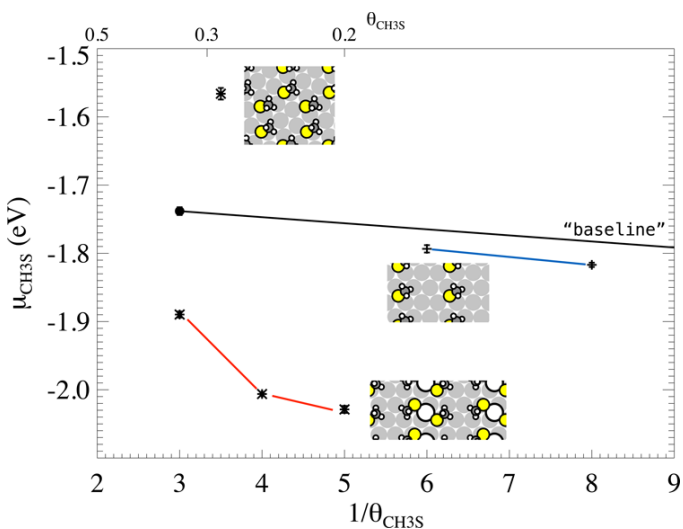


Figure 4.3 Stability as measured by the chemical potential of CH₃S of various structures on Au(111) versus the baseline.

Thus, the stability of individual RS–Au–SR complexes can be firmly established from DFT-PBE calculations. However, experiments also show that these complexes can self-organize into various patterns, among them a stripe phase with complexes separated by $\sqrt{3}a$ at low coverage.⁵¹ From PBE calculations, we cannot find any indication of significant

attractive interactions between complexes with a $\sqrt{3}a$ separation. *Table 4.1* lists the chemical potential of the RS group in a RS–Au–SR complex in various supercells. The complexes are all separated by $4a$ perpendicular to the stripe, but with different separations along the stripe direction. From *Table 4.1*, one can see that with DFT-PBE, when RS–Au–SR complexes are arranged in a row separated by $\sqrt{3}a$, they are about 0.02 eV less stable compared to more widely separated complexes. Thus, according to DFT-PBE, there is no driving force at low coverages for the complexes to form stripes, contrary to experimental evidence. We have tried other configurations by placing additional Au atoms at different places, trying to form direct links between complexes, but so far have failed to arrive at a more energetically favorable structure.

Table 4.1 Chemical potential (eV) for RS–Au–SR complexes with different spacing d along the stripe direction, calculated using PBE and the optB88-vdW functional^a

d (a)	θ (ML)	PBE	optB88-vdW
$\sqrt{3}$	1/4	-2.006(3)	-2.389(3)
$\sqrt{7}$	1/6	-2.008(3)	-2.331(3)
$2\sqrt{3}$	1/8	-2.031(3)	-2.355(2)

^aThe latter include dispersion interactions and results are obtained using PBE-optimized coordinates. Numbers in parentheses are estimates of numerical errors due to finite slab thickness and k -point grid.

As an alternative, it is widely believed that self-organization of alkanethiols is due to intermolecular interactions between the hydrocarbon tails.¹ It is therefore natural to investigate the effects of the dispersion interaction which DFT at the GGA level does not include. We choose the optB88-vdW functional,^{52,53} mainly due to the observations that it yields a lattice constant for bulk Au (4.161 Å) that is closest to experimental value (4.078 Å) among other kernel methods.⁵⁴ Due to higher computational cost of the dispersion interactions and the close match with the PBE lattice constant (4.158 Å), we fix the positions

of atoms at the PBE optimized geometries. Results are shown in *Table 4.1*. One can find that the $\sqrt{3}a$ stripes are 0.034–0.058 eV (per RS) more stable than more dilute configurations. This strongly suggests that the driving force toward formation of stripes is the dispersion interactions.

Figure 4.3 also shows the energetics of the $\sqrt{3}$ -row structure, which consists of individual CH_3S molecules rather than $\text{RS}-\text{Au}-\text{SR}$ complexes. They are slightly more stable than the baseline, similar to S and Cl on Au(111). The theoretical implication is that it might be possible to observe this structure at low temperatures as a metastable structure before the more stable $\text{RS}-\text{Au}-\text{SR}$ complexes are formed, but we are not aware of any experiment to support this possibility so far. Note that the relative stability of the $\sqrt{3}$ -row structure remains if the optB88-vdW functional is used. As for S, and Cl, the stability of this type of structure is likely caused by elastic interactions induced by adsorbates. PBE should perform reliably in this case.

We can also compare results in this subsection with a previous DFT study⁴⁹ of alkanethiolate adsorption on Au(111) in some detail. Some of their main results (e.g., with the PBE functional the $\text{Au}(\text{CH}_3\text{S})_2$ complexes are more stable than CH_3S on unreconstructed Au(111) surfaces) are consistent with the current study. In addition, their results using the M06-L meta-GGA⁵⁵ that show the stability of the complexes is much reduced compared with the stability of chemisorbed RS are also consistent with our calculations (section 3.5). However, there are also some important differences. Their results show that the cis- $\text{Au}(\text{CH}_3\text{S})_2$ complexes are more stable than the trans- $\text{Au}(\text{CH}_3\text{S})_2$ complexes at 1/3 ML RS coverage. We find that for both isolated and well-separated stripes of $\text{Au}(\text{RS})_2$ complexes, the trans structure is more stable than the cis structure. Only at the high 1/3 ML coverage,

when the CH₃ groups are forced higher above the surface, does the cis structure becomes more competitive. This is because raising the heights of the CH₃ groups while keeping the S atoms unchanged distorts the trans structure more than the less symmetrical cis structure.

From STM experiments, Voznyy et al.¹⁸ found patches of (3 × 4) phases for CH₃S on Au(111) near saturation and proposed a structure based on pairs of trans-Au(CH₃S)₂ complexes for this phase. Later experiments⁵⁶ show more extensive (3 × 4) structures. Earlier studies identify the (3 × 2√3)-rect ordering for long-chain alkanethiolate adsorption on Au(111) near saturation⁵⁷ and there is some confusion about whether it applies for methanethiolate also. DFT studies of RS–Au–SR complexes have been performed with both supercells,^{4,49,58} however, no comparison of energetics has been given to our knowledge. We will do so below.

Figure 4.4 shows four structures with three orderings. The first three [(a), (b), and (c)] correspond to structure 8, 9, and 10 in ref 49, respectively. Though (a) is the natural extension of the stripe structures (the energetics is shown in *Figure 4.3* also), it is the least stable. (b) is the cis equivalent of (a), and (c) is the structure proposed⁵⁹ for alkanethiolate with the (3 × 2√3) ordering. The relative stabilities from (a) to (c) agree quite well with ref 49. (d) is the structure proposed by Voznyy et al.¹⁸ and adopted by Tang et al.⁵⁶ for the observed (3 × 4) phase. These geometries have been studied using DFT in ref 18, and the energetics have been calculated in ref 4 recently. Here we compare it with other candidates and find it to be more stable. Note that this is not an extensive theoretical search for configurations of CH₃S on Au(111) at saturation, just a comparison between proposed structures. To facilitate comparison, we report here also energetics defined in ref 49 (dissociative adsorption energy per four CH₃SH, δE_d). The respective values are –1.20,

−1.33, −1.38, and −1.44 eV for *Figure 4.4a–d*, and ref 49 reports −0.92, −1.05, and −1.10 eV, respectively for *Figure 4.4a–c*.

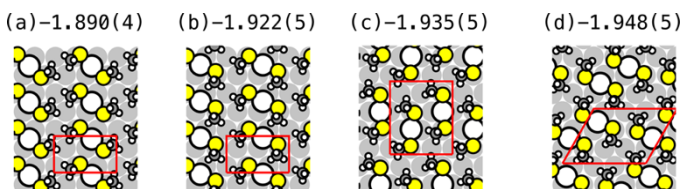


Figure 4.4 Energetics of various proposed RS–Au–SR structures at 1/3 ML for CH₃S on Au(111). Energetics (in eV) is defined in *eq (2)* and results are from PBE calculations, averaging over slab thickness L from 4 to 7. k -point grids are (8×14) for (a) and (b), (8×7) for (c), and (6 × 8) for (d). The numbers in parentheses denote the numerical uncertainties of the last digit obtained from the standard deviations of the data of different L divided by 4, the number of samples.

3.4. SiH₃S on Au(111).

Replacing the carbon atom in the methyl group by a silicon atom, the chemistry of silanethiolate should be similar to that of methanethiolate. Indeed, as shown in *Figure 4.5*, the DFT-PBE results for SiH₃S on Au(111) are very similar to those of CH₃S in *Figure 4.3*. The most stable Au(SiH₃S)₂ complexes also have the t-b-t configuration. The main difference is that there is a larger energy penalty when the stripes are 3a apart, which can be attributed to the larger size of Si than C atoms, so that repulsion between silyls is stronger than methyls at close distances.

3.5. Effects of Functionals and Dispersion Interactions.

Due to its efficiency and overall robustness, the PBE functional has been used extensively to study sulfur adsorption on, and reaction with, coinage metal surfaces.^{16,25,60,61} In previous sections, the relative stability of AuX₂ as a general trend on Au(111) is established, and excellent agreement with experiment is obtained using PBE, with the exception of $\sqrt{3}$ stripe phase of RS–Au–SR, as noted in section 3.3. However, in previous work with sulfur on Au and other coinage metal surfaces, we have noted some discrepancies

between DFT-PBE and experiments. For example, DFT-PBE predicts a Au_4S_5 complex to be more stable than the $p(2 \times 2)$ -S phase for S/Au(100), which is contradicted by STM experiments.¹² It is thus useful to compare results with various functionals in this particular situation, partly to learn the possible range of errors, and also hopefully identify a more consistent functional.

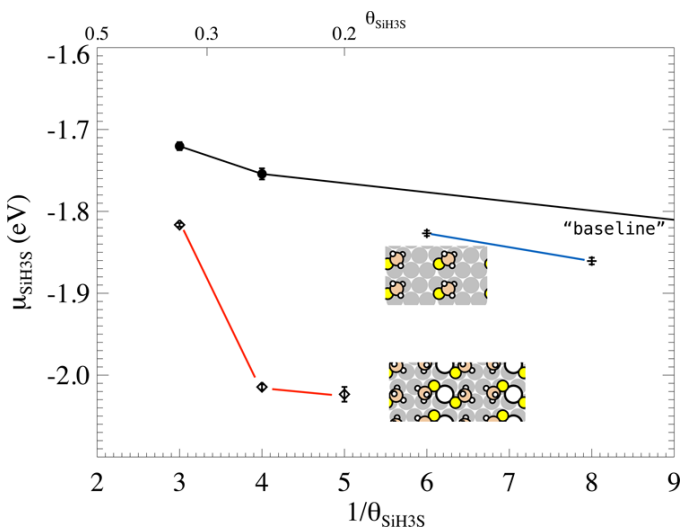


Figure 4.5 Energetics of various proposed RS–Au–SR structures at 1/3 ML for CH_3S on Au(111). Energetics (in eV) is defined in eq (2) and results are from PBE calculations, averaging over slab thickness L from 4 to 7. k -point grids are (8×14) for (a) and (b), (8×7) for (c), and (6×8) for (d). The numbers in parentheses denote the numerical uncertainties of the last digit obtained from the standard deviations of the data of different L divided by 4, the number of samples.

Among popular semilocal approximations, LDA and PBE represent two extremes in their tendencies to over- and underestimate the lattice constants, cohesive energies, etc., for bulk metals. Although the PBEsol⁶² functional greatly improves the bulk properties and surface energies of pure metals,⁶³ the description of adsorption of molecules such as CO is significantly worse than that by PBE.^{64,65} In contrast, the revTPSS⁶⁶ meta-GGA was shown to preserve both the good behavior for solids and reasonable atomization energies for molecules.

Semilocal functionals such as LDA and PBE neglect dispersion interactions. Here, the vdW-DF method by Dion et al.⁵⁴ with an optimized B88 form of exchange energy (optB88-vdW⁵²) is used to study effects of dispersion interactions. Because the prediction of a_0 for Au using optB88-vdW is very close to the PBE value, it is reasonable to expect that optimized geometries are similar too. Therefore, we fix the atoms at the PBE optimized geometries for the optB88-vdW calculations. Energetics (per ligand) obtained from optB88-vdW optimized geometries are generally only 0.01–0.02 eV lower than those obtained from PBE geometries. In contrast, the difference in the prediction of the lattice constant between LDA and PBE is large ($\sim 3\%$), and our tests show the errors using PBE geometries are also large (e.g. ~ 0.3 eV for E_b^S). The situation with revTPSS lies somewhere in between. The errors caused by using the PBE geometries are about 0.1–0.2 eV, which may be too big considering the small differences in energetics. Thus, in *Table 4.2*, we report LDA and revTPSS energetics from optimized structures obtained separately using the respective functionals.

Finally, the hybrid functional with exact exchange energy (HSE06⁶⁷) is used for selected cases, again with PBE optimized geometries. Due to the computational cost of exchange energies, we average over results with three- to five-layer slabs for HSE06, whereas for all others, results are averages of four- to seven-layer slabs. Errors due to using PBE geometries are estimated to be around 0.05–0.08 eV for the HSE06 functional.

As mentioned earlier, to assess the various bond strengths, we use the ground state energy of S, Cl, CH₃S, and SiH₃S ligands. Spurious differences arise from the approximations in DFT for the degenerate ground states of S and Cl atoms.⁶⁸ We use the one

with the lowest energy for each, which are all nonspherical except for the LDA calculations of the Cl atom.

Table 4.2 shows μ_X for various types of X–Au–X complexes calculated using different functionals, and a (3×3) supercell. For X = S and Cl, we identify four types of structures, which are illustrated in Figure 4.6 and labeled by the approximate adsorption sites of the three atoms [fcc (f), bridge (b), and top (t)]. For S, the sequence is b-t-b, b-f-b, t-b-t, and t-t-t, in decreasing stability. Note that all functionals predict essentially the same order for the complexes calculated, although with various degree of preference. The absolute binding energy is more significantly affected by functional choices. LDA predicts the strongest binding, and then optB88, PBE, and HSE06, in decreasing order. Note that the same trend holds for all other species in this study, except for SiH₃S where adsorption in HSE06 is slightly stronger than PBE.

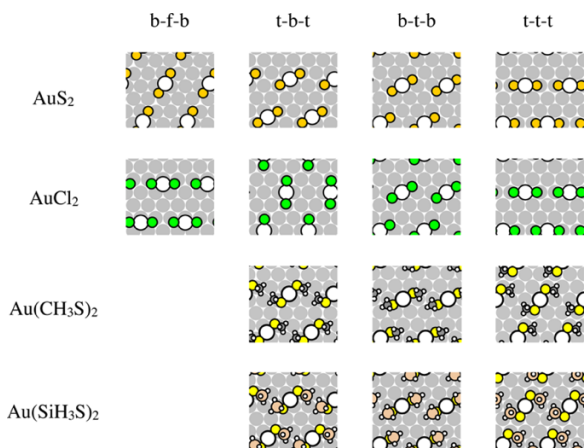


Figure 4.6 Various metastable, near linear X–Au–X complexes on Au(111), with all configurations obtained from PBE calculations in (3×3) supercells with five layer slabs.

For X = Cl, the sequence is t-b-t, t-t-t, b-f-b, and b-t-b. Note that there is no significant barrier from b-f-b to the very close and slightly more stable t-t-t configuration, so these two can be considered parts of a very broad metastable region in the energy landscape. The sequence is preserved for all functionals tested. These properties are the same for X =

CH₃S. For X = SiH₃S, t-t-t tends to be more favorable than t-b-t, but this might be due to the relatively small supercell used and the fact that repulsion between repeated complexes are stronger for the t-b-t configuration. We are also unable to produce metastable b-f-b like configurations for X = CH₃S and SiH₃S, but as noted before, the energy is close to that of t-t-t.

Although *Table 4.2* provides a summary of the energetics with different functionals, the stability can only be judged by comparison with many different configurations, as was done with the baseline configurations in previous subsections. For this purpose, in *Table 4.3* we report the difference in μ_X between the AuX₂ complexes and the baseline energetics of chemisorbed configurations. The complexes are chosen to be the most stable configuration in a $(4 \times \sqrt{3})$ -rect supercell (with $\theta_X = 1/4$ ML) (see *Figure 4.1* for an illustration). The reason for choosing a different supercell is that this is more favorable than the (3×3) supercell used earlier for t-b-t and b-t-b, the two most relevant structures. In other words, AuX₂ is more likely to form stripes than regular 2D arrays, and so results using this supercell are better suited to compare with experiments. See insets from *Figure 4.1, 2, 3, and 5* for real space representations.

Due to the larger difference in the lattice constants (also listed in *Table 4.3*), we optimized the geometries independently with LDA and revTPSS functionals and used the PBE optimized geometries for the optB88-vdW functional. Results for HSE06, however, are not reported here, because the determination of the baseline requires supercells too large for hybrid calculations. All functionals predict AuS₂ complexes are less stable than chemisorbed sulfur atoms. For AuCl₂, LDA and revTPSS functionals predict that the complexes are less stable, whereas PBE predicts they are more stable, with optB88-vdW being marginal. For

Table 4.2 Chemical potential (eV) for RS–Au–SR complexes with different spacing d along the stripe direction, calculated using PBE and the optB88-vdW functional^a

X		X-Au-X (2/9 ML)				X (1/4 ML)
		b-f-b	t-b-t	b-t-b	t-t-t	
S	LDA	-4.207	-3.869	-4.217		-4.496
	optB88-vdW	-3.451	-3.226	-3.517		-3.677
	PBE	-3.310	-3.068	-3.374	-2.934	-3.538
	revTPSS	-3.437		-3.438		-3.727
	HSE06			-3.215		-3.392
Cl	LDA		-2.869	-2.713	-2.765	-2.906
	optB88-vdW		-2.509	-2.398	-2.440	-2.449
	PBE	-2.287	-2.362	-2.244	-2.296	-2.242
	revTPSS		-2.176		-2.078	-2.257
	HSE06		-2.306			-2.223
CH ₃ S	LDA		-2.656	-2.284	-2.624	-2.545
	optB88-vdW		-2.275	-1.907	-2.279	-2.091
	PBE		-1.925	-1.583	-1.909	-1.704
	revTPSS		-1.734		-1.685	-1.666
	HSE06		-1.891			-1.645
SiH ₃ S	LDA		-2.753	-2.346	-2.864	-2.800
	optB88-vdW		-2.454	-2.131	-2.514	-2.388
	PBE		-1.904	-1.645	-1.905	-1.755
	revTPSS		-1.734		-1.741	-1.761
	HSE06		-1.911			-1.778

^aFor LDA, PBE, and revTPSS, results are obtained from fully relaxed geometries. For optB88-vdW and HSE06, the PBE optimized geometries are used. Energetics of the most stable structure for each functional are in bold, with differences less than 5 meV considered insignificant.

Au(CH₃S)₂ and Au(SiH₃S)₂, all functionals predict they are more stable than isolated ligands, but the stability is greatly reduced with revTPSS.

Table 4.3 Stability of AuX₂ complexes and properties of Bulk Au (cohesive energy E_c and lattice constant a_0) with different functionals^a

species	LDA	PBE	optB88-vdW	revTPSS
AuS ₂	0.0291	0.202	0.163	0.305
AuCl ₂	0.098	-0.062	-0.006	0.140
Au(CH ₃ S) ₂	-0.160	-0.259	-0.220	-0.113
Au(SiH ₃ S) ₂	-0.156	-0.260	-0.276	-0.111
E_c	-4.301	-3.039	-3.407	-3.621
a_0 (Å)	4.052	4.158	4.161	4.078

^aAll energies are in units of electronvolts. Stabilities are measured by difference of the chemical potential with the baseline $\delta\mu_X$, as demonstrated in *Figure 4.1*. Chemical potentials of the X–Au–X complexes are calculated with $(4 \times \sqrt{3})$ -rect supercells.

4. AuX₂ Complexes in The Gas Phase

The linear X–M–X complexes have been shown to be a prevalent building motif for several coinage metal M and ligands X on metal surfaces.^{9–12,20,51} In this section, we study the energetics and geometries of AuX₂ complexes using quantum chemistry techniques ranging from DFT to coupled cluster methods.

The binding energy per Au–X bond is calculated by $E_b = [E(\text{AuX}_2) - E(\text{Au}) - 2E(\text{X})]/2$, where $E(\text{AuX}_2)$ is the energy of an optimized small complex AuX₂, $E(\text{Au})$ is the gold atomic energy, and $E(\text{X})$ is the energy of the optimized X in the gas phase. *Table 4.4* shows the calculated binding energies using different basis sets and DFT functionals: PBE,²⁴ PBE0,²⁸ and M06.²⁹ UCCSD(T)^{38–41} results with different basis sets and extrapolations are

also shown. Unless noted otherwise, the energies are calculated using geometries optimized at the same level of theory.

4.1. AuS₂

DFT results show that the binding energy per Au–S bond in AuS₂ ranges from –1.90 to –3.00 eV depending on the functional and basis set. The extrapolated UCCSD(T) value is –2.57 eV. Compared to PBE0 and M06, PBE estimates stronger binding energy. The effect of spin contamination on the adsorption energy is small—the difference between the RODFT and UDFT type treatments are 0.03 eV. In terms of basis set dependence, both PBE and PBE0 show that the binding energy increases with larger basis sets (def2-TZVP, def2-QZVP) suggesting that more diffuse and larger basis sets are needed in this case. Likewise, the binding energy of UCCSD(T) increases with larger basis sets.

4.2. AuCl₂

DFT results show that the binding energy per Au–Cl bond in AuCl₂ ranges from –2.29 to –2.96 eV compared to an extrapolated UCCSD(T) value of –2.46 eV. The effect of size of basis set and spin contamination is similar to that for AuS₂. The difference between RODFT and UDFT types of calculations is 0.02 eV. Again, the larger basis sets for DFT calculations tend to increase the binding. The bond strength is very similar to Au–S with PBE but stronger than Au–S with PBE0 and M06. Similar to DFT, UCCSD(T) bond strength increases with larger basis sets. The extrapolated UCCSD(T) values indicate that the average Au–S bond is 0.11 eV stronger than Au–Cl.

4.3. Au(CH₃S)₂

DFT results show that the binding energy per Au–CH₃S bond in Au(CH₃S)₂ ranges from –2.08 to –2.60 eV compared to the extrapolated UCCSD(T) value of –2.48 eV. The bond strength is weaker than Au–S and Au–Cl with PBE regardless of basis set whereas it

does not have a consistent trend with PBE0 and M06: the energetic trend changes with the size of basis set. The extrapolated UCCSD(T) data show Au-CH₃S binding energy is weaker than Au-S and a little stronger than (but very similar to) Au-Cl: the trend so far is Au-S > Au-CH₃S > Au-Cl. The effect of spin contamination and basis set dependence are consistent with previous systems.

4.4. Au(SiH₃S)₂

DFT results show that the binding energy per Au-SiH₃S bond in Au(SiH₃S)₂ is from -2.18 to -2.67 eV and the extrapolated UCCSD(T) value is -2.45 eV. The bond strength is weaker than Au-S and Au-Cl but stronger than Au-CH₃S with PBE whereas it is weaker than Au-Cl but stronger than Au-S and Au-CH₃S with PBE0 and M06. The same trend remains with different basis sets. The extrapolated UCCSD(T) data, however, show that the Au-SiH₃S binding energy becomes the weakest among the four molecules.

4.5. Summary

Energetic trend according to the extrapolated UCCSD(T) value is Au-S > Au-CH₃S > Au-Cl > Au-SiH₃S. As *Table 4.4* shows, however, the difference in the binding energy of Au-X is not as significant as of adsorbates on the surface (cf. *Table 4.2*), suggesting that the interaction with the surface is the key difference in the adsorbates found on the surface.

Basis set dependence in the DFT and UCCSD(T) results show a stronger binding energy with larger basis set. Spin contamination has only a small effect on the binding energy.

5. Discussion

Metal-ligand complexes, for which AuX₂ (X = S, Cl, CH₃S, etc.) are perhaps the simplest, can sometimes form spontaneously on metal surfaces. DFT calculations with various functionals indicate that on the Au(111) surface, one should see AuX₂ complexes for

Table 4.4 Binding energy (eV) of Au–X (X = S, Cl, CH₃S, and SiH₃S) complexes in the gas phase^a

		PBE		PBE0	M06	UCCSD(T)
		RODFT	UDFT	RODFT	RODFT	ROHF
AuS ₂	DZ/TZ	-2.60	-2.57	-1.93	-1.90	-1.95
	TZ/QZ	-2.96		-2.36		
	QZ/QZ	-3.00		-2.40		-2.46 ^c
	aug-DZ/aug-DZ					-2.36 ^c
	aug-TZ/aug-TZ					-2.52 ^c
	extrapolation ^e					-2.57
AuCl ₂	DZ/TZ	-2.60	-2.58	-2.30	-2.29	-2.03
	TZ/QZ	-2.93		-2.67		
	QZ/QZ	-2.96		-2.70		-2.45 ^c
	aug-DZ/aug-DZ					-2.37 ^b
	aug-TZ/aug-TZ					-2.45 ^b
	extrapolation ^e					-2.46
Au(CH ₃ S) ₂	DZ/TZ	-2.39	-2.37	-2.14	-2.08	
	TZ/QZ	-2.60		-2.35 ^b		
	QZ/QZ	-2.60 ^b		-2.37 ^b		
	aug-DZ/aug-DZ					-2.31 ^d
	aug-TZ/aug-TZ					-2.44 ^d
	extrapolation ^e					-2.48
Au(SiH ₃ S) ₂	DZ/TZ	-2.45	-2.42	-2.23	-2.18	
	TZ/QZ	-2.65		-2.42 ^b		
	QZ/QZ	-2.67		-2.44 ^b		
	aug-DZ/aug-DZ					-2.42 ^d
	aug-TZ/aug-TZ					-2.49 ^d
	extrapolation ^e					-2.45

^aThe basis sets are listed in the second column for Au and X, with DZ = LANL2DZ (Au), TZ = def2-TZVP (Au) and 6-311++G(d,p) (X), QZ = def2-QZVP (Au) and def2-QZVPPD (X), aug-DZ = aug-cc-pVDZ-PP(Au) and aug-cc-pVDZ (X), and aug-TZ = aug-cc-pVTZ-PP (Au) and aug-cc-pVTZ (X). ^bUsing geometry optimized at the PBE DZ/TZ level. ^cUsing geometry optimized at the UCCSD(T) DZ/TZ level. ^dUsing geometry optimized at the PBE TZ/QZ level. ^eUCCSD(T) correlation energy is extrapolated with two-point aug-DZ ($x = 2$) and aug-TZ ($y = 3$) fits using *eq (3)*.

X = CH₃S and SiH₃S and not for AuS₂ complexes. The stability of the AuCl₂ complex is very close to that of chemisorbed Cl atoms, and the relative stability depends on the functional used. The stability of these complexes reflects a subtle balance between binding of ligands to the metal surfaces, binding to single metal atoms, and cohesive energy of the metal bulk. The analysis of which poses tremendous challenges, requiring both high precision (as in minimizing errors from finite k-points grid and slab thicknesses) and accuracy (as in the theoretical approximation of exchange-correlation functional). In this work, we use the overall robust and efficient PBE functional to map a more global energy landscape. Very good agreement with experiments has been achieved for the existence and detailed structure (such as adsorption sites) of AuX₂ complexes for X = Cl and CH₃S. Notably, PBE fails to predict the observed $\sqrt{3}$ stripes for CH₃S, but using a functional that includes dispersion interactions has been shown to be successful. Finally, the PBE functional predicts the stability of AuCl₂ complexes at low coverages, which is inconsistent with experimental observations.²⁰ Using functionals that predict larger cohesive energies, such as optB88-vdW^{52,53} and revTPSS,⁶⁶ the stability of AuCl₂ complexes are reduced, which is more consistent with experiments.

Higher level quantum chemistry calculations for small complexes and experimental results serve as sign posts to estimate the errors in various approximations in DFT. We find that the M06 functional improves upon PBE results for AuX₂ complexes in the gas phase, compared with the CCSD(T) results. We find that the average bond energies of various X–Au–X complexes in the gas phase are remarkably similar, whereas the adsorption energies of X to the Au(111) surface show larger variations. Stabilities of the complexes thus correlate with the adsorption energy of the ligand. The strong interactions between S and the Au(111)

surface deter the formation of Au–S complexes. Although sulfur atoms interact directly with Au atoms in chemisorption of thiolates on Au(111), surprisingly Cl atoms seem to mimic the behavior of methyl or silanethiolates better. This is reflected in both the relative stability and the most stable configuration of the AuX₂ complexes.

Finally, we mention that the linear X–M–X motif can be viewed as building blocks in proposed models for a wide variety of systems, e.g., the O/Ag(111) p(4 × 4) phase,^{69,70} the (17 × 17)R14° phase for S/Ag(111),⁷¹ and Cu₂S₃ clusters for S/Cu(111).¹¹ The mechanism and trend found here should be transferable to some extent to these system also.

Acknowledgments

J.L., J.S.B., T.L.W., and D.J.L. performed the computations in this work and were supported by the U.S. Department of Energy (USDOE), Office of Basic Energy Sciences, Division of Chemical Sciences, Geosciences, and Biosciences through the Ames Laboratory Chemical Physics program. P.A.T. advised on the analysis of energetics, provided experimental and chemical insights, and was supported by NSF Grant CHE1507223. We acknowledge use of resources at the National Energy Research Scientific Computing Center (NERSC), a DOE Office of Science User Facility supported by the Office of Science of the U.S. Department of Energy under Contract No. DE-AC02-05CH11231. The work was performed at Ames Laboratory which is operated for the USDOE by Iowa State University under Contract No. DE-AC02-07CH11358.

References

1. Ulman, A. Formation and Structure of Self-Assembled Monolayers. *Chem. Rev.* **1996**, *96*, 1533–1554.
2. Love, J. C.; Estroff, L. A.; Kriebel, J. K.; Nuzzo, R. G.; Whitesides, G. M. Self-Assembled Monolayers of Thiolates on Metals as a Form of Nanotechnology. *Chem. Rev.* **2005**, *105*, 1103–1169.

3. Pensa, E.; Cortés, E.; Corthey, G.; Carro, P.; Vericat, C.; Fonticelli, M. H.; Benítez, G.; Rubert, A. A.; Salvarezza, R. C. The Chemistry of the Sulfur-Gold Interface: In Search of a Unified Model. *Acc. Chem. Res.* **2012**, *45*, 1183–1192.
4. Vericat, C.; Vela, M. E.; Corthey, G.; Pensa, E.; Cortés, E.; Fonticelli, M. H.; Ibañez, F.; Benitez, G. E.; Carro, P.; Salvarezza, R. C. Self-assembled monolayers of thiolates on metals: a review article on sulfur-metal chemistry and surface structures. *RSC Adv.* **2014**, *4*, 27730–27754.
5. Li, X.; Robinson, S. M.; Gupta, A.; Saha, K.; Jiang, Z.; Moyano, D. F.; Sahar, A.; Riley, M. A.; Rotello, V. M. Functional Gold Nanoparticles as Potent Antimicrobial Agents against Multi-Drug-Resistant Bacteria. *ACS Nano* **2014**, *8*, 10682–10686.
6. Ma, C.-L.; Nghiem, D.; Chen, Y.-C. Alkanethiol-based single-molecule transistors. *Appl. Phys. Lett.* **2008**, *93*, 222111.
7. Venkataraman, L.; Klare, J. E.; Tam, I. W.; Nuckolls, C.; Hybertsen, M. S.; Steigerwald, M. L. Single-Molecule Circuits with Well-Defined Molecular Conductance. *Nano Lett.* **2006**, *6*, 458–462.
8. Yim, T.-J.; Wang, Y.; Zhang, X. Synthesis of a gold nanoparticle dimer plasmonic resonator through two-phase-mediated functionalization. *Nanotechnology* **2008**, *19*, 435605.
9. Shen, M.; Liu, D.-J.; Jenks, C. J.; Thiel, P. A. Novel Self-organized Structure of a Ag-S Complex on the Ag(111) Surface below Room Temperature. *J. Phys. Chem. C* **2008**, *112*, 4281–4290.
10. Russell, S. M.; Kim, Y.; Liu, D.-J.; Evans, J. W.; Thiel, P. A. Communication: Structure, formation, and equilibration of ensembles of Ag-S complexes on an Ag surface. *J. Chem. Phys.* **2013**, *138*, 071101.
11. Walen, H.; Liu, D.-J.; Oh, J.; Lim, H.; Evans, J. W.; Aikens, C. M.; Kim, Y.; Thiel, P. A. Cu₂S₃ complex on Cu(111) as a candidate for mass transport enhancement. *Phys. Rev. B: Condens. Matter Mater. Phys.* **2015**, *91*, 045426.
12. Walen, H.; Liu, D.-J.; Oh, J.; Yang, H. J.; Kim, Y.; Thiel, P. A. Identification of Au-S complexes on Au(100). *Phys. Chem. Chem. Phys.* **2016**, *18*, 4891.
13. Walen, H.; Liu, D.-J.; Oh, J.; Yang, H. J.; Kim, Y.; Thiel, P. A. Long-range Displacive Reconstruction of Au(110) Triggered by Low Coverage of Sulfur. *J. Phys. Chem. C* **2015**, *119*, 21000–20010.
14. Woodruff, D. P. The interface structure of n-alkylthiolate self-assembled monolayers on coinage metal surfaces. *Phys. Chem. Chem. Phys.* **2008**, *10*, 7211–7221.

15. Jin, R. Quantum sized, thiolate-protected gold nanoclusters. *Nanoscale* **2010**, *2*, 343.
16. Walen, H.; Liu, D.-J.; Oh, J.; Lim, H.; Evans, J. W.; Kim, Y.; Thiel, P. A. Self-organization of S adatoms on Au(111): $\sqrt{3}R30^\circ$ rows at low coverage. *J. Chem. Phys.* **2015**, *143*, 014704.
17. Zheltov, V. V.; Cherkez, V. V.; Andryushechkin, B. V.; Zhidomirov, G. M.; Kierren, B.; Fagot-Revurat, Y.; Malterre, D.; Eltsov, K. N. Structural paradox in submonolayer chlorine coverage on Au(111). *Phys. Rev. B: Condens. Matter Mater. Phys.* **2014**, *89*, 195425.
18. Voznyy, O.; Dubowski, J. J.; Yates, J. T., Jr.; Maksymovych, P. The role of Gold adatoms and Stereochemistry in Self-Assembly of Methylthiolate on Au(111). *J. Am. Chem. Soc.* **2009**, *131*, 12989–12993.
19. Yu, M.; Ascolani, H.; Zampieri, G.; Woodruff, D. P.; Satterley, C. J.; Jones, R. G.; Dhanak, V. R. The Structure of Atomic Sulfur Phases on Au(111). *J. Phys. Chem. C* **2007**, *111*, 10904–10914.
20. Andryushechkin, B. V.; Cherkez, V. V.; Gladchenko, E. V.; Pavlova, T. V.; Zhidomirov, G. M.; Kierren, B.; Didiot, C.; Fagot-Revurat, Y.; Malterre, D.; Eltsov, K. N. Self-organization of Gold Chloride Molecules on Au(111) Surface. *J. Phys. Chem. C* **2013**, *117*, 24948–24954.
21. Tang, L.; Li, F. S.; Guo, Q. Complete Structural Phases for Self-Assembled Methylthiolate Monolayers on Au(111). *J. Phys. Chem. C* **2013**, *117*, 21234–21244.
22. Kresse, G.; Hafner, J. Ab initio molecular dynamics for liquid metals. *Phys. Rev. B: Condens. Matter Mater. Phys.* **1993**, *47*, R558–R561.
23. Kresse, G.; Furthmüller, J. Efficiency of ab-initio total energy calculations for metals and semiconductors using a plane-wave basis set. *Comput. Mater. Sci.* **1996**, *6*, 15–50.
24. Perdew, J. P.; Burke, K.; Ernzerhof, M. Generalized Gradient Approximation Made Simple. *Phys. Rev. Lett.* **1996**, *77*, 3865–3868; Generalized Gradient Approximation Made Simple [Phys. Rev. Lett. *77*, 3865 (1996)]. *Phys. Rev. Lett.* **1997**, *78*, 1396.
25. Abufager, P. N.; Zampieri, G.; Reuter, K.; Martiarena, M. L.; Busnengo, H. F. Long-range periodicity of S/Au(111) structures at low and intermediate coverages. *J. Phys. Chem. C* **2014**, *118*, 290.
26. Tang, H.; der Ven, A. V.; Trout, B. L. Phase diagram of oxygen adsorbed on platinum (111) by first-principles investigation. *Phys. Rev. B: Condens. Matter Mater. Phys.* **2004**, *70*, 045420.

27. Valiev, M.; Bylaska, E.; Govind, N.; Kowalski, K.; Straatsma, T.; van Dam, H.; Wang, D.; Nieplocha, J.; Apra, E.; Windus, T.; et al. NWChem: a comprehensive and scalable open-source solution for large scale molecular simulations. *Comput. Phys. Commun.* **2010**, *181*, 1477–1489.
28. Adamo, C.; Barone, V. Toward reliable density functional methods without adjustable parameters: The PBE0 model. *J. Chem. Phys.* **1999**, *110*, 6158–6170.
29. Zhao, Y.; Truhlar, D. G. The M06 suite of density functionals for main group thermochemistry, thermochemical kinetics, non-covalent interactions, excited states, and transition elements. *Theor. Chem. Acc.* **2008**, *120*, 215–241.
30. Hay, P. J.; Wadt, W. R. *Ab initio* effective core potentials for molecular calculations. Potentials for the transition metals atoms Sc to Hg. *J. Chem. Phys.* **1985**, *82*, 270–283.
31. Wadt, W. R.; Hay, P. J. *Ab initio* effective core potentials for molecular calculations. Potentials for the main group elements Na to Bi. *J. Chem. Phys.* **1985**, *82*, 284–298.
32. Hay, P. J.; Wadt, W. R. *Ab initio* effective core potentials for molecular calculations. Potentials for K to Au including the outermost core orbitals. *J. Chem. Phys.* **1985**, *82*, 299–310.
33. Weigend, F.; Ahlrichs, R. Balanced basis sets of split valence, triple zeta valence and quadruple zeta valence quality for H to Rn: Design and assessment of accuracy. *Phys. Chem. Chem. Phys.* **2005**, *7*, 3297.
34. McLean, A. D.; Chandler, G. S. Contracted Gaussian basis sets for molecular calculations. I. Second row atoms, $Z = 11-18$. *J. Chem. Phys.* **1980**, *72*, 5639–5648.
35. Krishnan, R.; Binkley, J. S.; Seeger, R.; Pople, J. A. Self-consistent molecular orbital methods. XX. A basis set for correlated wave functions. *J. Chem. Phys.* 1980, *72*, 650–654.
36. Clark, T.; Chandrasekhar, J.; Spitznagel, G. W.; von Ragué Schleyer, P. Efficient diffuse function-augmented basis sets for anion calculations. III. The 3-21+G basis set for first-row elements, Li-F. *J. Comput. Chem.* **1983**, *4*, 294–301.
37. Rappoport, D.; Furche, F. Property-optimized Gaussian basis sets for molecular response calculations. *J. Chem. Phys.* **2010**, *133*, 134105.
38. Raghavachari, K.; Trucks, G. W.; Pople, J. A.; Head-Gordon, M. A fifth-order perturbation comparison of electron correlation theory. *Chem. Phys. Lett.* **1989**, *157*, 479.
39. Rendell, A.; Lee, T. J.; Komornicki, A.; Wilson, S. Evaluation of the contribution from triply excited intermediates to the fourth-order perturbation theory energy on Intel distributed memory supercomputers. *Theoret. Chim. Acta* **1993**, *84*, 271–287.

40. Kobayashi, R.; Rendell, A. P. A direct coupled cluster algorithm for massively parallel computers. *Chem. Phys. Lett.* **1997**, *265*, 1–11.
41. Aprà, E.; Rendell, A. P.; Harrison, R. J.; v. Tipparaju, A.; Dejong, W.; Xantheas, S. S. Liquid Water: Obtaining the Right Answer for the Right Reasons. *Proceedings of the conference on high performance computing networking, storage and analysis*; ASM: New York, 2009.
42. Peterson, K. A.; Puzzarini, C. Systematically convergent basis sets for transition metals. II. Pseudopotential-Based correlation consistent basis sets for the group 11 (Cu, Ag, Au) and 12 (Zn, Cd, Hg) elements. *Theor. Chem. Acc.* **2005**, *114*, 283–296.
43. Dunning, T. H. Gaussian basis sets for use in correlated molecular calculations. I. The atoms boron through neon and hydrogen. *J. Chem. Phys.* **1989**, *90*, 1007–1023.
44. Woon, D. E.; Dunning, T. H. Gaussian basis sets for use in correlated molecular calculations. III. The atoms aluminum through argon. *J. Chem. Phys.* **1993**, *98*, 1358–1371.
45. Halkier, A.; Helgaker, T.; Jørgensen, P.; Klopper, W.; Koch, H.; Olsen, J.; Wilson, A. K. Basis-Set convergence in correlated calculations on Ne, N₂, and H₂O. *Chem. Phys. Lett.* **1998**, *286*, 243–252.
46. Truhlar, D. G. Basis-set extrapolation. *Chem. Phys. Lett.* **1998**, *294*, 45–48.
47. Cherkez, V. V.; Zheltov, V. V.; Didiot, C.; Kierren, B.; Fagot-Revurat, Y.; Malterre, D.; Andryushechkin, B. V.; Zhidomirov, G. M.; Eltsov, K. N. Self-ordered nanoporous lattice formed by chlorine atoms on Au(111). *Phys. Rev. B: Condens. Matter Mater. Phys.* **2016**, *93*, 045432.
48. Jiang, D.; Dai, S. Cis-trans conversion of the CH₃S–Au–SCH₃ complex on Au(111). *Phys. Chem. Chem. Phys.* **2009**, *11*, 8601–8605.
49. Ferrighi, L.; Pan, Y.-X.; Grönbeck, H.; Hammer, B. Study of Alkylthiolate Self-assembled Monolayers on Au(111) Using a Semilocal meta-GGA Density Functional. *J. Phys. Chem. C* **2012**, *116*, 7374–7379.
50. Maksymovych, P.; Sorescu, D. C.; Yates, J. T., Jr. Gold-Adatom-Mediated Bonding in Self-Assembled Short-Chain Alkanethiolate Species on the Au(111) Surface. *Phys. Rev. Lett.* **2006**, *97*, 146103.
51. Maksymovych, P.; Voznyy, O.; Dougherty, D. B.; Sorescu, D. C., Jr.; Yates, J. T. Gold adatom as a key structural component in self-assembled monolayers of organosulfur molecules on Au(111). *Prog. Surf. Sci.* **2010**, *85*, 206–240.

52. Klimeš, J.; Bowler, D. R.; Michaelides, A. Chemical accuracy for the van der Waals density functional. *J. Phys.: Condens. Matter* **2010**, *22*, 022201.
53. Klimeš, J.; Bowler, D. R.; Michaelides, A. Van der Waals density functionals applied to solids. *Phys. Rev. B: Condens. Matter Mater. Phys.* **2011**, *83*, 195131.
54. Dion, M.; Rydberg, H.; Schröder, E.; Langreth, D. C.; Lundqvist, B. I. Van der Waals Density Functional for General Geometries. *Phys. Rev. Lett.* **2004**, *92*, 246401.
55. Zhao, Y.; Truhlar, D. G. A new local density functional for main-group thermochemistry, transition metal bonding, thermochemical kinetics, and noncovalent interactions. *J. Chem. Phys.* **2006**, *125*, 194101.
56. Tang, L.; Li, F.; Zhou, W.; Guo, Q. The structure of methylthiolate and ethylthiolate monolayers on Au(111): Absence of the ($\sqrt{3} \times \sqrt{3}$)R30° phase. *Surf. Sci.* **2012**, *606*, L31–L35.
57. Camillone, N., III; Chidsey, C. E. D.; Eisenberger, P.; Fenter, P.; Li, J.; Liang, K. S.; Liu, G.-Y.; Scoles, G. Structural defects in self-assembled organic monolayers via combined atomic beam and xray diffraction. *J. Chem. Phys.* **1993**, *99*, 744.
58. Vericat, C.; Vela, M. E.; Benitez, G.; Carro, P.; Salvarezza, R. C. Self-assembled monolayers of thiols and dithiols on gold: new challenges for a well-known system. *Chem. Soc. Rev.* **2010**, *39*, 1805–1834.
59. Grönbeck, H.; Häkkinen, H.; Whetten, R. L. Gold-thiolate complexes Form a Unique $c(4 \times 2)$ Structure on Au(111). *J. Phys. Chem. C* **2008**, *112*, 15940–15942.
60. Rodriguez, J. A.; Dvorak, J.; Jirsak, T.; Liu, G.; Hrbek, J.; Aray, Y.; González, C. Coverage effects and the nature of the metal-Sulfur bond in S/Au(111): High-Resolution Photoemission and Density-functional Studies. *J. Am. Chem. Soc.* **2003**, *125*, 276–285.
61. Shen, M.; Russell, S. M.; Liu, D.-J.; Thiel, P. A. Destabilization of Ag nanoislands on Ag(100) by adsorbed sulfur. *J. Chem. Phys.* **2011**, *135*, 154701.
62. Perdew, J. P.; Ruzsinszky, A.; Csonka, G. I.; Vydrov, O. A.; Scuseria, G. E.; Constantin, L. A.; Zhou, X.; Burke, K. Restoring the density-gradient expansion for exchange in solids and surfaces. *Phys. Rev. Lett.* **2008**, *100*, 136406.
63. Tran, F.; Stelzl, J.; Blaha, P. Rungs 1 to 4 of DFT Jacob's ladder: Extensive test on the lattice constant, bulk modulus, and cohesive energy of solids. *J. Chem. Phys.* **2016**, *144*, 204120.
64. Stroppa, A.; Kresse, G. The shortcomings of semi-local and hybrid functionals: what we can learn from surface science studies. *New J. Phys.* **2008**, *10*, 063020.

65. Sun, J.; Marsman, M.; Csonka, G. I.; Ruzsinszky, A.; Hao, P.; Kim, Y.-S.; Kresse, G.; Perdew, J. P. Self-consistent meta-generalized gradient approximation within the projector-augmented-wave method. *Phys. Rev. B: Condens. Matter Mater. Phys.* **2011**, *84*, 035117.
66. Perdew, J. P.; Ruzsinszky, A.; Csonka, G. I.; Constantin, L. A.; Sun, J. Workhorse Semilocal Density Functional for Condensed Matter Physics and Quantum Chemistry. *Phys. Rev. Lett.* **2009**, *103*, 026403.
67. Krukau, A. V.; Vydrov, O. A.; Izmaylov, A. F.; Scuseria, G. E. Influence of the exchange screening parameter on the performance of screened hybrid functionals. *J. Chem. Phys.* **2006**, *125*, 224106.
68. Baerends, E. J.; Branchadell, V.; Sodupe, M. Atomic reference energies for density functional calculations. *Chem. Phys. Lett.* **1997**, *265*, 481–489.
69. Schnadt, J.; Michaelides, A.; Knudsen, J.; Vang, R. T.; Reuter, K.; Lægsgaard, E.; Scheffler, M.; Besenbacher, F. Revisiting the Structure of the $p(4 \times 4)$ Surface Oxide on Ag(111). *Phys. Rev. Lett.* **2006**, *96*, 146101.
70. Schmid, M.; Reicho, A.; Stierle, A.; Costina, I.; Klikovits, J.; Kostelnik, P.; Dubay, O.; Kresse, G.; Gustafson, J.; Lundgren, E.; et al. Structure of Ag(111)- $p(4 \times 4)$ -O: No Silver Oxide. *Phys. Rev. Lett.* **2006**, *96*, 146102.
71. Russell, S. M.; Shen, M.; Liu, D.-J.; Thiel, P. A. Adsorption of sulfur on Ag(100). *Surf. Sci.* **2011**, *605*, 520–527.

CHAPTER 5. STABILITY OF M_3S_3 COMPLEXES ON FCC $M(111)$ SURFACES: $M = \text{AU, AG, CU, AND NI}$

A paper published in and reprinted with permission from

Surface Science **2018**,

Da-Jiang Liu,^{a,*} Jiyoung Lee,^{a,b} Theresa L. Windus,^{a,b} Patricia A. Thiel,^{a,b,c}
and James W. Evans^{a,d}

^a*Ames Laboratory – USDOE, Iowa State University, Ames, IA 50011, USA*

^b*Department of Chemistry, Iowa State University, Ames, IA 50011, USA*

^c*Department of Materials Science & Engineering, Iowa State University, Ames, IA 50011, USA*

^d*Department of Physics and Astronomy, Iowa State University, Ames, IA 50011, USA*

**Corresponding author*

Abstract

Density Functional Theory is utilized to assess the stability of metal (M)–sulfur (S) complexes adsorbed on fcc $M(111)$ surfaces, specifically considering S-decorated planar M trimers, M_3S_3 . Scanning Tunneling Microscopy studies have identified structures proposed to be Ni_3S_3 on $\text{Ni}(111)$, and Au_3S_3 on $\text{Au}(111)$. Also, Cu_3S_3 on $\text{Cu}(111)$ has been suggested to facilitate enhanced Cu surface mass transport. Our analysis considers M_3S_3 complexes for $M = \text{Au, Ag, Cu, and Ni}$, assessing key measures of stability on surfaces, and also comparing behavior with trends in gas-phase stability. These surface and gas-phase analyses are systematically related within the framework of Hess’s law, which allows elucidation of various contributions to the overall energetics. In all cases, the adsorbed complex is stable relative to its separated constituents adsorbed on the terrace. However, only for Ag does one find a negative energy of formation from excess S on terraces and M extracted from kink sites along step edges, implying spontaneous complex formation for this pathway. We interpret various experimental observations in the context of our results for energetics.

1. Introduction

The formation of metal-chalcogenide complexes at surfaces has been implicated in enhanced coarsening of supported metal nanoclusters,¹⁻³ and more generally in accelerated metal transport across metal surfaces.⁴⁻⁸ The latter is evidenced by more facile surface nanostructure dynamics or evolution than for the corresponding chalcogenide-free system. Our focus in this contribution is on metal (M)–sulfur (S) complexes adsorbed on various fcc $M(111)$ transition metal surfaces, and specifically on S -decorated planar M trimers, M_3S_3 . Below, for convenience, we sometimes just refer to these as trimers.

Experimental motivation for this selection comes in part from a previous Scanning Tunneling Microscopy (STM) study of the $S + Ni(111)$ system at room temperature which observed features interpreted as collections of Ni_3S_3 complexes.⁹ It was proposed that during exposure of $Ni(111)$ to a source of S , existing step edges become quickly passivated. Simultaneously or subsequently, S induces a $(5\sqrt{3} \times 2)$ rect reconstruction of portions of terraces on the surface. The reconstruction produces arrays of parallel troughs from which Ni atoms are ejected. These Ni adatoms are proposed to remain on terraces due to the passivation of steps, and to facilitate formation of complexes on non-reconstructed portions of the terraces by reaction with adsorbed S . For the coinage metals, direct STM observation of isolated complexes at room temperature is likely not viable given their expected significant mobility. However, STM imaging at liquid nitrogen temperatures of the $S + Au(111)$ system has revealed features identified as Au_3S_3 on portions of the surface where the herringbone reconstruction is lifted by S adsorption.¹⁰ For later discussion, we note that lifting this reconstruction liberates Au atoms onto the terraces. Contrasting this study, a separate STM analysis of the $S + Au(111)$ system at 5 K did not find such complexes.¹¹ STM

studies of the S + Cu(111) system at temperatures down to 50 K revealed intricate structures at step edges which were proposed to incorporate Cu_3S_3 complexes,¹² although a subsequent combined STM + Density Functional Theory (DFT) characterization of these structures at 5 K came to a different conclusion.¹³ Finally, it is appropriate to note STM studies of the S + Ag(111) system which revealed self-organized dot-row structures at 200 K.¹⁴ The separated dots were identified as likely being Ag_3S_3 complexes, with adsorbed S in the spaces between the dots presumably playing a key role in stabilizing the dot-row structure. The discussion section of this paper will provide our analysis and interpretation of several of these experimental observations.

Additional motivation for consideration of M_3S_3 trimers comes from a theoretical proposal, which has received considerable attention, that the presence of Cu_3S_3 complexes can dramatically enhance Cu surface mass transport on Cu(111) relative to the S-free surface.¹⁵ This enhancement was reflected in a dramatic increase in the rate of decay of two-dimensional (2D) Cu islands on Cu(111) exposed to trace amounts of S as observed by Low Energy Electron Microscopy (LEEM) at ~500 K, and as observed by STM at ~200 K.⁶ This proposal utilized the key observation that while the surface mobility of these complexes is well below that of Cu adatoms, the default carrier for Cu surface transport, the formation energy for the complexes is also far below that for adatoms. Thus, the equilibrium density of the complexes is far higher than that of Cu adatoms. The mass transport flux reflects the product of carrier mobility and carrier density,⁶ and the higher density of complexes more than compensates for their lower mobility. Analogous increased decay rates for 2D Ag islands on Ag(111) exposed to trace amounts of S were observed in STM studies at 300 K.¹⁶

This observation naturally also prompts consideration of Ag_3S_3 complexes as potential facilitators of Ag surface transport.

It is appropriate at this point to provide some insight into the structure of these $M_3\text{S}_3$ complexes. From previous experimental observations, and from DFT calculations in the current and previous studies, the most stable configuration for $M = \text{Cu}$, Ag, and Ni, includes a planar triangular trimer of M atoms, each of which is adsorbed at three-fold (3fh) hollow sites on the $M(111)$ surface. The triangular metal core is oriented with three edges constituting A-type (100) microfaceted steps, each of which is decorated by an S atom. One feature proposed to induce stability of these complexes is the long-suggested preference of S for four-fold hollow (4fh) sites, which are presented by the A-type steps, over 3fh sites on fcc(111) terraces.^{15,17} This preference was recently quantified by DFT analyses for both extended Cu surfaces and nanoclusters.¹⁸ For $M = \text{Au}$, on the other hand, our analysis will show that the most stable trimer structure is rotated by 30° so that Au resides on bridge sites. See *Fig. 5.1* for illustrations of these configurations.

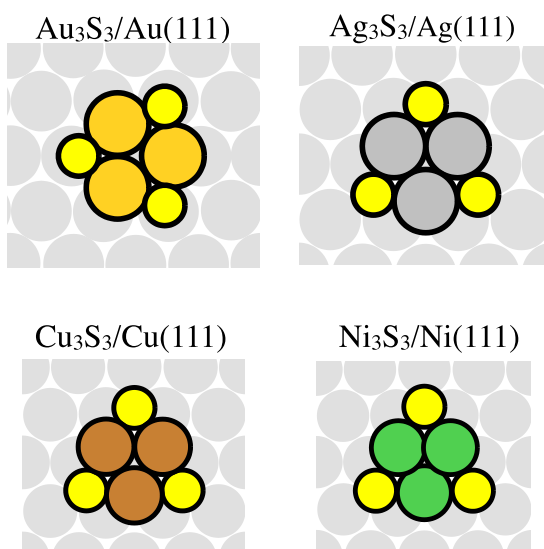


Figure 5.1 Schematics of the most stable $M_3\text{S}_3$ configuration on the $M(111)$ surface for $M = \text{Au}$, Ag, Cu, and Ni.

It should be noted that other complexes with features similar to the above M_3S_3 trimers have been identified by STM in various systems, and often also assessed by DFT analysis. Heart-shaped M_2S_3 complexes rather than trimers have been directly observed for $M = \text{Cu}$ on Cu(111) surfaces at 5 K,¹⁹ indicating at least a slight energetic preference over trimers. Furthermore, it has been suggested that these hearts, rather than trimers, could be the dominant Cu mass transport carrier in the above-mentioned accelerated decay of 2D Cu islands.¹⁹ Neither hearts nor trimers have been directly observed on Ag(111) at 5 K, but rather larger complexes.²⁰ However, the smaller complexes could exist with significant populations at higher temperatures where enhanced island decay was observed, but where direct imaging of mobile complexes is not viable. Finally, we mention that a pyramidal Co_3S_4 complexes have been observed on both Au(111) and Ag(111) surfaces.^{21,22} These complexes consist of a planar Co_3S_3 trimer with an additional S located on top at the 3rd Co site. The Co_3S_4 complexes facilitate Co surface mass transport which mediates the conversion of Co nanoclusters to a cobalt sulfide phase on the surface at 300 K.²²

Our primary interest is in the stability of adsorbed M_3S_3 complexes, and we will subsequently discuss in some detail the relevant criteria for stability. However, we suggest that it is also natural and instructive to consider the stability of the complexes in the gas-phase, anticipating that this “intrinsic” stability could be reflected in trends in stability of adsorbed complexes. Clearly gas-phase and surface stability are not directly related as one must account for differentiating factors such as adsorption energies. However, we systematically integrate all of these analyses within the framework of Hess’s law to provide a comprehensive picture of energetics in these systems.

Finally, with regard to integrating these different analyses, we mention that electronic structure analysis of gas-phase complexes is typically and naturally performed utilizing an atomic basis functions either via DFT or utilizing higher-level theory. However, analysis for adsorbed complexes on extended $M(111)$ surfaces is most naturally assessed with slab calculations using plane-wave basis DFT and periodic boundary conditions (where adsorbed complexes have negligible interaction with their periodically repeated images for a choice of sufficiently large lateral unit cell). Thus, for consistency, we will carefully compare analysis of gas-phase energetics with both localized and periodic plane-wave bases.

In Section 2, we provide a brief description of our theoretical methodology. Criteria for surface stability are briefly discussed in Section 3. Results of our analysis are presented in Section 4. In Section 5, we utilize our results to interpret various experimental observations, and also present our conclusions.

2. Methodology

The VASP package (v5.4)^{23,24} with PAW potentials^{25,26} is used for DFT calculations with Plane-Wave (PW) basis-sets and periodic boundary conditions. The PBE²⁷ functional is used for surface calculations with slab geometries. Both PBE and PBE0²⁸ functionals are used for the gas phase calculations. The energy cutoff for the plane wave analysis is 280 eV. For surface calculations, first-order Methfessel–Paxton smearing of width 0.2 eV is used. Slabs are separated by 12 Å of vacuum. S and M -S complexes are adsorbed on one side of the slab, with the bottom layer fixed. Lattice constants are selected as the DFT-PBE theoretical values, which are $a=4.151, 4.149, 3.651,$ and 3.519 Å for Au, Ag, Cu, and Ni, respectively. All surface energetics are obtained from an average over 4 to 7 layer thick slabs to mitigate quantum size effects.²⁹ The bulk cohesive energy is calculated separately for surface energetics, using a linear fit to results of slabs with various thickness as proposed by

Fiorentini and Methfessel.³⁰ For each supercell, we use a k -point grid that is closest to the equivalent of $(24 \times 24 \times 1)$ for the unit surface cell. As indicated above, plane-wave DFT calculations are also used to analyze the energetics of gas-phase complexes. In these analyses, M_3S_3 complexes are arranged in a 3D orthogonal periodic array with periods approximately $(2.8a, 2.8a, 14 \text{ \AA})$, sufficiently large to minimize interactions between complexes. Gaussian smearing of width 0.002 eV are used. Non spin polarized calculations are used for bulk and slab systems with Au, Ag, and Cu, and spin polarized calculations are used for all gas phase systems and Ni bulk and slab systems.

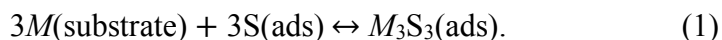
For analysis of the energetics of gas-phase complexes, DFT calculations with atomic basis sets are also naturally performed using the NWChem software package.³¹ Energetics for all complexes are analyzed using three different basis sets. For the smallest basis set, denoted by DZ/TZ, we use Los Alamos National Laboratory double- ζ (LANL2DZ) with effective core potentials (ECP's)³²⁻³⁴ for metals and 6-311++G(d,p)³⁵⁻³⁷ for S. For the intermediate basis set, denoted by TZ/TZ, we use def2-TZVP³⁸⁻³⁹ for metals and def2-TZVPPD⁴⁰ for S. For the largest basis set, denoted by QZ/QZ, we use def2-QZVP³⁸⁻³⁹ for metals and def2-QZVPPD⁴⁰ for S. In def2, all electron basis sets are used for lighter atoms such as Cu and Ni, while ECP basis sets are used for heavier atoms such as Ag and Au. Also for the QZ/QZ basis sets, we use spherical harmonic function rather than the default Cartesian Gaussian function to reduce linear dependence. For spin multiplicity, Au_3S_3 , Ag_3S_3 , Cu_3S_3 , and their M_3 trimers are doublets, while Ni_3S_3 is a quintet and the Ni_3 trimer is a triplet for PBE and a quintet for PBE0 (i.e., these have the lowest energy among the different spin states). To avoid spin contamination, restricted open-shell DFT (RODFT) is

performed with the number of radial grid points equal to 99 and the number of angular points in the Lebedev grid set to 590.

3. Criteria for Stability of Adsorbed M_3S_3 Complexes

To appropriately characterize stability of M_3S_3 trimers adsorbed on $M(111)$ surfaces, it is necessary to first specify the complex formation and dissociation process or pathway of interest. We shall show that this depends on the experimental system and conditions. This pathway in turn determines the various “competing” surface configurations for which energies should be compared. Below, we discuss two different pathways or scenarios for complex formation.

In the *first scenario*, we consider a system where “excess” adsorbed S adatoms are present on the terraces of the $M(111)$ surface, but not isolated M adatoms beyond the negligible equilibrium population (which is controlled by step-edge detachment-reattachment equilibrium). Then, these excess S adatoms can potentially combine with M atoms extracted from extended step edges on the $M(111)$ surface to form complexes. We characterize this process as



At least in some systems, S adatoms bind preferentially at step edges (e.g., at 4fh sites on A-type steps) rather than on terraces.^{9,16} Thus, for such systems, the above scenario requires that the S coverage is sufficiently high that these step edges are completely saturated, thereby resulting in excess S which can populate terraces.¹⁶ This scenario will be particularly relevant to the analysis of observed behavior on Cu(111) and Ag(111) surfaces, as discussed further in Section 5.

The relevant energy accounting for the above process might be formulated in different ways. One instructive formulation is based on a picture where all atoms involved in

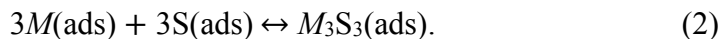
the complex formation process are in the same top layer of the system in both the initial and final configurations. This is clearly the case for the S adatoms, and one can regard the M atoms which are incorporated into the complex as being extracted from kink sites on a step edge in the same layer. Then, energy changes during the process are reasonably (but not precisely) associated with just changes in lateral interactions within that layer. During complex formation, there is an energy advantage (i.e., an energy reduction) from the formation of lateral M - M and M -S bonding within the complex, and an energy penalty from the cost of extracting the three M atoms from the step edge. The latter cost is actually equal to three times the lateral energy per M atom in a complete top layer (or in the interior of a large island) on the $M(111)$ surface. The imprecision in this picture comes from the feature that there can be difference in interlayer bonding of S and M atoms to the lower substrate layers in the initial configuration versus when they are incorporated into the complex.

The above issue suggests a more appropriate energy accounting for the complex formation process. If one still considers all species involved as residing in a single layer, then one should account for both lateral interactions within that layer, and also interlayer interactions with the lower supporting layers. In this case, the initial configuration energies will include the adsorption energy of isolated S adatoms, and the energy of M atoms to be extracted from the step edge. The latter includes both lateral bonding to other M atoms, and the energy of adsorption or bonding to the lower supporting layers. The final configuration energy will include both lateral interactions within the complex, and also its adsorption or binding to the lower supporting layers. The procedure for evaluation of all these energies within our DFT analysis is described in Section 4. A significant point is that the energy per M atom to be extracted from the step edge in this formulation is directly related to the bulk

cohesive energy, E_c . This can be regarded as reflecting the feature that the ultimate source of M atoms is the interior of the substrate. For this reason, in the representation (1) of the complex formation pathway, it is reasonable to replace $M(\text{substrate})$ with $M(\text{bulk})$, and this is done below in Section 4.

One conclusion from the above discussion is that the ease of complex formation via this pathway will be impacted by the bulk cohesive energy for the metal, higher values tending to inhibit complex formation. To this end, we note values of $E_c = 3.04, 2.52, 3.47,$ and 4.79 eV for Au, Ag, Cu, and Ni, respectively. For consistency with our subsequent energetic analysis of other quantities, here we have quoted values obtained from our DFT analysis (with the PBE functional²⁷) rather than experimental values.⁴¹

A *second scenario* might apply for far-from-equilibrium systems where a supersaturation of M adatoms is generated on terraces, which coexists with excess S adatoms also on terraces. In this case, we characterize the complex formation process as



The relevant energy accounting for this second scenario is straightforward and naturally follows the formulation used for the first pathway. The initial configuration energies will include the adsorption energy of isolated S adatoms, and the adsorption energy of isolated M . The final configuration energy will include both lateral interactions within the complex, and also its adsorption or binding to the lower supporting layers (just as for the first pathway). Analysis of these energies also follows the prescription given for the first pathway. This second pathway for complex formation avoids the energy cost of extracting metal atoms from step edges. As a result, this pathway is naturally more facile, and the associated energetics are not expected to correlate significantly with bulk cohesive energies. We will

clarify the relevance of this second pathway in our discussion in Section 5 of experimental observations. Some mechanism is needed for the generation of M adatoms on terraces, and this could potentially be provided by reconstruction of Ni(111) and Au(111) surfaces.

4. Results for Energetics of M_3S_3 Complexes

4.1. Gas-phase Complexes

First, for the gas phase complex denoted by $M_3S_3(\text{gas})$, we analyze the *atomization energy* which is determined from

$$E_{\text{at}}(\text{gas}) = 3E[M(\text{gas})] + 3E[S(\text{gas})] - E[M_3S_3(\text{gas})], \quad (3)$$

where $E[\dots]$ denotes the total energy of the indicated species. We adopt the standard convention where binding lowers energy, so binding energies are negative, and atomization energies associated with bond- breaking are positive. DFT results utilizing the PBE and PBE0 functionals are shown in *Table 5.1* where we compare results from NWChem for three different choices of localized basis set with those from VASP utilizing a plane-wave basis. For PBE, we find excellent consistency between the two approaches for $M = \text{Au}, \text{Ag},$ and Cu , provided that a sufficiently large localized basis set is utilized. The larger difference in $E_{\text{at}}(\text{gas})$ for $M = \text{Ni}$ may be caused by the ambiguity in the atomic reference energy of the Ni atom at the PBE level.^{42,43} The hybrid PBE0 values are lower than the PBE values for all basis sets (a feature which might be anticipated from previous studies⁴⁴). The agreement between energetics for atomic and plane wave basis sets for PBE0 are not as good as for the PBE functional. Nonetheless, the trend that $E_{\text{at}}(\text{gas})$ increases as M varies from Ag, Au, Cu, to Ni is the same regardless of the basis set and the functional. With regard to the high value of $E_{\text{at}}(\text{gas})$ for Ni, we note that our analysis of molecular orbital relevant for bonding shows that Ni has a particularly strong contribution from d orbitals whereas s and p orbitals are more significant for the other metals.

Table 5.1 Atomization energy $E_{at}(\text{gas})$ of M_3S_3 complexes in the gas phase in eV.

	Au ₃ S ₃	Ag ₃ S ₃	Cu ₃ S ₃	Ni ₃ S ₃
	PBE			
DZ/TZ ^a	13.40	11.33	15.38	18.42
TZ/TZ ^a	14.73	12.68	16.38	19.91
QZ/QZ ^a	14.92	12.81	16.46	19.98
PW ^b	14.92	12.69	16.63	20.32
	PBE0			
DZ/TZ ^a	11.87	9.89	13.39	14.71
TZ/TZ ^a	13.25	11.20	14.31	15.92
QZ/QZ ^a	13.44	11.34	14.41	15.95
PW ^b	13.56	11.82	15.10	17.15

^aNWChem, ^bVASP

These atomization energies include contributions associated with both M -S and M - M interactions. Thus, it is also instructive to extract just the component associated with M -S binding in order to compare the magnitudes for different M . To this end, we determine *total M-S binding* in $M_3S_3(\text{gas})$ from

$$E_{MS}(\text{gas}) = E[M_3S_3(\text{gas})] - E[M_3(\text{gas})] - 3E[S(\text{gas})], \quad (4)$$

where $M_3(\text{gas})$ is the gas-phase M_3 trimer obtained by detaching the S from M_3S_3 but maintaining the M_3 geometry. PBE results in *Table 5.2* again show the need for high-quality localized atomic basis sets for agreement of NWChem results with VASP values. Since the atomic reference energy of the Ni atom is not needed in the calculation of $E_{MS}(\text{gas})$, good agreement for $M = \text{Ni}$ has also been achieved between NWChem and VASP. Trends in E_{MS} mimic those for $E_{at}(\text{gas})$ comparing behavior for different M . Again, with the hybrid PBE0, the binding between M and S becomes weaker for all M , and the agreement between NWChem and VASP are not as satisfactory, even using the largest basis sets.

Finally, from the above results, we can also extract the total M - M binding within the complexes from

$$E_{MM}(\text{gas}) = E[M_3(\text{gas})] - 3E[M(\text{gas})] = -E_{\text{at}}(\text{gas}) - E_{MS}(\text{gas}). \quad (5)$$

Using results from the PBE VASP analysis, this yields $E_{MM}(\text{gas}) = -3.20, -2.39, -3.39,$ and -5.24 eV, for $M = \text{Au}, \text{Ag}, \text{Cu},$ and Ni , respectively. The relative magnitude follows the same trend as the bulk cohesive energy (with Ag having the weakest binding, and Ni the strongest).

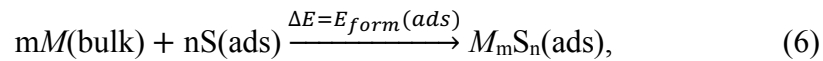
Table 5.2 Total M -S binding energy $E_{MS}(\text{gas})$ of M -S complex in the gphase in eV.

	Au ₃ S ₃	Ag ₃ S ₃	Cu ₃ S ₃	Ni ₃ S ₃
	PBE			
DZ/TZ ^a	-10.51	-9.08	-11.94	-13.71
TZ/TZ ^a	-11.67	-10.18	-13.14	-14.99
QZ/QZ ^a	-11.75	-10.29	-13.22	-15.04
PW ^b	-11.72	-10.31	-13.24	-15.08
	PBE0			
DZ/TZ ^a	-9.42	-8.02	-10.75	-12.02
TZ/TZ ^a	-10.65	-9.15	-11.77	-13.31
QZ/QZ ^a	-10.73	-9.27	-11.87	-13.37
PW ^b	-10.83	-9.78	-12.42	-14.14

^aNWChem, ^bVASP

4.2. Adsorbed Complexes

In the *first pathway* for complex formation described in Section 3, the complexes are created from excess S adatoms on terraces and from M extracted from kink sites at extended step edges, where we have argued in Section 3 that the source of this M can be regarded as the bulk substrate. Thus, the process is described schematically by



the corresponding *formation energy* is given by

$$E_{\text{form}}(\text{ads}) = E[M_m S_n(\text{ads})] - 3E[S(\text{ads})] - 3E[M(\text{bulk})]. \quad (7)$$

Here $E[X(\text{ads})] = E[X(\text{ads}) + \text{slab}] - E(\text{slab})$ is the energy difference between a system with a X adsorbed on the surface and the clean surface. $E[M(\text{bulk})]$ is the energy per M atom in the bulk fcc metal.

Some further discussion is needed to relate the quantities in eq. (7) to the various contributing energies described in Section 3. To this end, it is appropriate to define the following quantities. The adsorption energy for S is given by $E_{ad}(\text{S}) = E[\text{S}(\text{ads})] - E[\text{S}(\text{gas})]$. The combined adsorption plus internal lateral interaction energy for the complex is given by $E_{ad} + \text{int}(M_3S_3) = E[M_3S_3(\text{ads})] - 3E[M(\text{gas})] - 3E[\text{S}(\text{gas})]$, which should be contrasted with the adsorption energy for the complex of $E_{ad}(M_3S_3) = E[M_3S_3(\text{ads})] - E[M_3S_3(\text{gas})]$. All of these energies are negative. Finally, $E[M(\text{bulk})]$ is simply related to the bulk cohesive energy, $E_c(M) \geq 0$, through $-E_c(M) = E[M(\text{bulk})] - E[M(\text{gas})]$. From these definitions, it immediately follows that

$$E_{form}(\text{ads}) = E_{ad+\text{int}}(M_3S_3) - 3E_{ad}(\text{S}) + 3E_c(M) \quad (8)$$

which is consistent with the description in Section 3. Further details on the slab calculations performed with VASP with the PBE functional to determine these different components is also provided in Section 2. The corresponding results are presented in *Table 5.3*.

Table 5.3 Formation energy, $E_{form}(\text{ads})$, and binding energy, $E_{bind}(\text{ads})$, for the adsorbed complex from PBE in eV.

	Au ₃ S ₃	Ag ₃ S ₃	Cu ₃ S ₃	Ni ₃ S ₃
VASP $E_{form}(\text{ads})$	+0.29	-0.15	+0.12	+0.90
VASP $E_{bind}(\text{ads})$	-1.59	-1.91	-2.31	-2.56

$E_{form}(\text{ads})$ is only negative for Ag corresponding to spontaneous complex formation in the presence of excess adsorbed S (but not M) on terraces. Such Ag₃S₃ complexes are stable

against dissociation and reincorporation of M into the bulk. In all other cases with positive $E_{form}(\text{ads})$, the equilibrium population of complexes is determined by the Boltzmann factor $\exp[-E_{form}(\text{ads})/(k_B T)]$. Given the small value for $E_{form}(\text{ads})$ for Au, and especially for Cu, these populations will be sufficiently large around room temperature to potentially enhance surface mass transport.

The complex formation energy for the *second pathway* described in Section 3, where the complexes are formed from excess S adatoms on terraces and isolated M adatoms on terraces corresponds to the *binding energy* for adsorbed complexes, $E_{bind}(\text{ads})$. This quantity is the surface analogue of the gas-phase binding energy, $E_{bind}(\text{gas}) = -E_{at}(\text{gas})$, which is just the negative of the gas-phase atomization energy. $E_{bind}(\text{ads})$ is defined by

$$E_{bind}(\text{ads}) = E[M_3S_3(\text{ads})] - 3E[S(\text{ads})] - 3E[M(\text{ads})] \quad (9)$$

Denoting $E_{ad}(M) = E[M(\text{ads})] - E[M(\text{gas})]$ as the adsorption energy for an M adatom, which is negative, it is straightforward to show that

$$E_{bind}(\text{ads}) = E_{ad}(M_3S_3) - 3E_{ad}(S) - 3E_{ad}(M) + E_{bind}(\text{gas}) \quad (10)$$

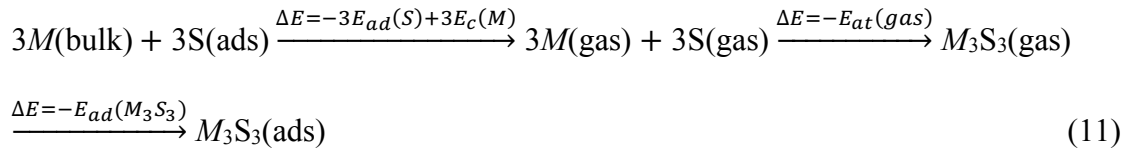
PBE results from VASP analysis are also presented in Table 3. In all cases, one has that $E_{bind}(\text{ads}) < 0$ which implies that the complexes are stable against dissociation into S adatoms and M adatoms residing on the terrace.

Finally, we note that the difference between $E_{form}(\text{ads})$ and $E_{bind}(\text{ads})$ corresponds to the energy cost to extract three M atoms from (kink sites) at the step edge and to locate them on the terrace. From the above results, the corresponding energy cost per atom is $E_{extract}(\text{ads}) = 0.63, 0.59, 0.81,$ and 1.18 eV for Au, Ag, Cu, and Ni, respectively. In a model for energetics of metal adlayers with just nearest-neighbor lateral attractive interactions of strength $\phi(\text{surf}) > 0$, one has that $E_{extract}(\text{ads}) = 3\phi(\text{surf})$. Note that while such simplified

models can be quite effective,⁴⁵ $\phi(\text{surf})$ is quite different from the effective pair interaction, $\phi(\text{bulk})$, obtained from the bulk energetics via $\phi(\text{bulk}) = E_c/6$. Using $\phi(\text{bulk})$, one would obtain $E_{\text{extract}}(\text{ads}) = 1.52, 1.26, 1.74, 2.40$ eV, respectively.

4.3. Analysis of Energetics within the Framework of Hess's Law

Hess's law in thermochemistry decomposes an overall reaction into several elemental steps, which allows the total enthalpy change to be obtained from the sum of contributions from the individual steps. There is considerable flexibility in choosing the steps, and here we decompose the process of complex formation on the surface into desorption, gas-phase complex formation, and adsorption steps:



These steps are also illustrated in *Fig. 5.2*. In the first step, ΔE is positive, and in the second and third steps, ΔE is negative. With regard to the energetics associated with the above steps, DFT values for the cohesive energy are reported in Section 3, and DFT values for the gas-phase atomization energy are reported in Section 4.1. Thus, it remains only to determine the adsorption energies for S adatoms and for M_3S_3 complexes. DFT results from VASP are given in *Table 5.4*. The adsorption energy of M_3S_3 is calculated using (4×4) supercells, corresponding to $\theta_S = 3/16$ ML, sufficiently low so that interactions between complexes are negligible. For consistency, the corresponding $E_{ad}(S)$ at the same coverage is estimated by interpolating results for the S adsorption energy obtained using a $(\sqrt{7} \times \sqrt{7})$ supercell (where $\theta_S = 1/7$ ML) and a (2×2) supercell (where $\theta_S = 1/4$ ML). With these results, one can reconstruct the surface formation energy, $E_{\text{form}}(\text{ads})$, for formation of

complexes from excess adsorbed S and bulk M from adding energies for the three steps indicated above. See *Table 5.5*.

Table 5.4 Adsorption energies $E_{ad}(S)$ and $E_{ad}(M_3S_3)$ in eV from PBE in both cases with $\theta_S = 3/16$ ML.

	Au	Ag	Cu	Ni
$E_{ad}(S)$	-3.58	-3.61	-4.37	-5.12
$E_{ad}(M_3S_3)$	-4.65	-5.84	-6.76	-8.52

Table 5.5 Decomposition of $E_{form}(ads)$ corresponding to Hess's law using PBE energies in eV.

M	$ E_{ad}(S) $	$E_c(M)$	E_{dest}	$E_{at}(gas)$	$ E_{ad}(M_3S_3) $	E_{stab}	$E_{form}(ads)$
Au	3.58	3.04	19.86	14.92	4.65	19.57	+0.29
Ag	3.61	2.52	18.40	12.69	5.84	18.54	-0.15
Cu	4.37	3.47	23.52	16.63	6.77	23.40	+0.12
Ni	5.12	4.79	29.75	20.33	8.52	28.85	+0.90

It is already clear from comparing the results in *Tables 5.1* and *5.3* that trends with varying M in the stability of gas-phase complexes are not well-correlated with those of adsorbed complexes as determined by $E_{form}(ads)$. To understand these differing trends, within a Hess's law framework, one can regard $E_{form}(ads) = E_{dest} - E_{stab}$ as coming from the difference between a positive destabilizing contribution, $E_{dest} = 3|E_{ad}(S)| + 3E_c(M)$, and a positive stabilizing contribution, $E_{stab} = E_{at}(gas) + |E_{ad}(M_3S_3)|$. The former is the energy cost of extracting three S from surface and three M from the bulk into the gas phase (the left step for the Hess cycle in *Fig. 5.2*). The latter is the energy gained from forming the complex in the gas-phase from constituent atoms and adsorption of that complex on the surface (a combination of the top step and the right step for the Hess cycle in *Fig. 5.2*). Both E_{dest} and E_{stab} are far larger than the magnitude of $E_{form}(ads)$ (see *Table 5.5*) in part explaining the lack of correlation between this quantity and $E_{at}(gas)$.

For example, the complex in the gas phase is most (least) stable for Ni (Ag) with the largest (smallest) E_{at} . In contrast, the adsorbed complex formed from bulk M and adsorbed S is least (most) stable for Ni (Ag) with the most positive (negative) $E_{form}(ads)$. Indeed, both components of the stabilizing term E_{stab} are larger for Ni than for other metals including Ag. However, with regard to the behavior of $E_{form}(ads)$, this effect is more than offset by the large cohesive energy for Ni and the large adsorption energy for S on Ni(111) (which are both larger than for other metals).

Finally, we remark that there is a reasonable correlation between trends in $E_{bind}(gas) = -E_{at}(gas)$ and the corresponding surface binding energy, $E_{bind}(ads)$. Ni has the largest values, then Cu, with both Ag and Au smaller (and with the order for Ag and Au switching between gas and adsorbed phases).

5. Discussion and Conclusions

We now exploit results from the previous section to interpret experimental STM observations related to adsorbed metal-sulfur trimers in various systems. First, for the S + Ni(111) system, $E_{form}(ads) = 0.98$ eV is so large that the equilibrium population of Ni_3S_3 complexes (formed from terrace S and bulk Ni) is negligible even at temperatures well above 300 K. Despite this result, as noted in Section 1, STM studies at 300 K did observe features which were interpreted as Ni_3S_3 complexes.⁹ However, the situation in this S + Ni(111) system is special in the sense that in the early stages of S adsorption steps are passivated, and S-induced reconstruction of portions of the terraces leads to ejection of metal atoms on to the terrace which cannot readily incorporate into step edges according to Ref. (9). Thus, it is plausible that the associated supersaturation of Ni adatoms on terraces can lead to facile formation of complexes given that the binding energy, $E_{bind}(ads) = -2.56$ eV is strongly negative.

Next, we consider the S + Au(111) system. In this case, $E_{form}(ads) = 0.30$ eV is moderately large, so the equilibrium population of Au_3S_3 complexes (formed from terrace S and bulk Au) is fairly low at 10^{-5} per surface site at 300 K. Such complexes are presumably quite mobile at 300 K, and thus could not be directly imaged (which in any case would be challenging given their low density). Furthermore, lowering the temperature in order to freeze the complexes on the surface would result in a dramatically lower density (assuming that freeze-in occurred well below 300 K). Thus, direct observation at lower temperature should also not be viable. Nonetheless, features were observed at liquid nitrogen temperature which were interpreted as Au_3S_3 complexes.¹⁰ A possible explanation relates to the feature that S adsorption on Au(111) lifts the herringbone reconstruction of the surface resulting in ejection of Au atoms onto the terrace. Plausibly, the presence of such Au adatoms could facilitate the formation of complexes for which $E_{bind}(ads) = -1.59$ eV. However, this is a non-equilibrium process, the ejected Au atoms needing to be captured by S rather than by step edges. It should be noted that a recent detailed STM study of this system found only Au adatoms at 5 K.¹¹ However, it is likely that parameters including S flux and coverage, and importantly cooling rate, differed between the studies. (Note that in Ref. (10), the two Au_3S_3 configurations identified are actually 0.39 and 0.33 eV *less* stable than the configuration in *Fig. 5.1*, according to our calculations using PBE functional.)

For S + $M(111)$ with $M = Cu$ or Ag , M_3S_3 complexes have not been observed in STM studies at 5 K in either system,^{19,20} despite the expectation that this might be possible at least for Cu.¹⁵ For Cu, Cu_2S_3 hearts rather than Cu_3S_3 trimers were in fact observed at 5 K.¹⁹ This can be understood given that DFT analysis in that study indicated that the hearts had a lower chemical potential (and lower formation energy) than trimers. Consequently, the quasi-

equilibrium population of hearts would dominate that of trimers at the (unknown) freeze-in temperature where complexes were immobilized. For Ag, larger complexes rather than hearts or dimers were observed in STM studies at 5 K.²⁰ The chemical potential of such larger complexes must be lower than that for trimers or other small clusters (which otherwise should form spontaneously). This does not exclude the possibility of a significant population of Ag_3S_3 complexes at, say, around 300 K.

In conclusion, our DFT analyses have provided a comprehensive picture of the energetics related to the stability of M_3S_3 complexes. Significantly, these results enable an appropriate interpretation of experimental observations in several $S + M(111)$ systems. Recent studies suggest that the formation of not just M_3S_3 trimers, but a variety of other metal-S complexes, on surfaces is unexpectedly common, and can play an important role in the dynamics of such surface systems.

Acknowledgments

D.-J.L., J.L., T.L.W. and J.W.E. performed the theoretical analysis and computations in this work, and were supported by the U.S. Department of Energy (US DOE), Office of Basic Energy Sciences, Division of Chemical Sciences, Geosciences, and Biosciences through the Ames Laboratory Chemical Physics program. We acknowledge use of resources of the National Energy Research Scientific Computing Center, a DOE Office of Science User Facility supported by the Office of Science of the U.S. DOE under Contract No. DE-AC02-05CH11231. P.A.T. contributed to the formulation of this project and provided experimental insights, and was supported for this work by NSF Grant no. CHE-1507223. The work was performed at Ames Laboratory which is operated for the USDOE by Iowa State University under Contract no. DE-AC02-07CH11358.

References

1. P.J.F. Harris, Growth and structure of supported metal catalyst particles, *Int. Mater. Rev.* 40 (1995) 97–115.
2. S. Porsgaard, L.R. Merte, L.K. Ono, F. Behafarid, J. Matos, S. Helveg, M. Salmeron, B.R. Cuenya, F. Besenbacher, Stability of platinum nanoparticles supported on SiO₂/Si(111): a high-pressure x-ray photoelectron spectroscopy study, *ACS Nano* 6 (12) (2012) 10743–10749.
3. P.N. Plessow, F. Abild-Pedersen, Sintering of Pt nanoparticle via volatile PtO₂: simulation and comparison with experiments, *ACS Catal.* 6 (2016) 7098–7108.
4. J. Perdereau, G.E. Rhead, LEED studies of adsorption on vicinal copper surfaces, *Surf. Sci.* 24 (1971) 555–571.
5. J.S. Ozcomert, W.W. Pai, N.C. Bartelt, J.E. Reutt-Robey, Kinetics of oxygen-induced faceting of vicinal Ag(110), *Phys. Rev. Lett.* 72 (1994) 258.
6. W.L. Ling, N.C. Bartelt, K. Pohl, J. de la Figuera, R.Q. Hwang, K.F. McCarty, Enhanced self-diffusion on Cu(111) by trace amounts of S: chemical-reaction-limited kinetics, *Phys. Rev. Lett.* 93 (2004) 166101.
7. M. M. Biener, J. Biener, C. M. Friend, Sulfur-induced mobilization of Au surface atoms on Au(111) studied by real-time STM, *Surf. Sci.* 601 (2007) 1659–1667.
8. P.A. Thiel, M. Shen, D.J. Liu, J.W. Evans, Adsorbate-enhanced transport of metals on metal surfaces: oxygen and sulfur on coinage metals, *J. Vac. Sci. Technol. A* 28 (2010) 1285.
9. M. Yamada, H. Hirashima, A. Kitada, K. Izumi, J. Nakamura, Three-Ni-atom cluster formed by sulfur adsorption on Ni(111), *Surf. Sci.* 602 (2008) 1659–1668.
10. S. Kurokawa, Y. Miyawaki, A. Sakai, Scanning tunneling microscopy observation of sulfur adsorbates on Au(111) at liquid nitrogen temperature, *Jpn. J. Appl. Phys.* 48 (2009) 08JB12.
11. H. Walen, D.J. Liu, J. Oh, H. Lim, J.W. Evans, Y. Kim, P.A. Thiel, Self-organization of S adatoms on Au(111): $\sqrt{3}R30^\circ$ rows at low coverage, *J. Chem. Phys.* 143 (2015) 014704.
12. E. Wahlström, I. Ekvall, T. Kihlgren, H. Olin, S.A. Lindgren, L. Walldén, Low-temperature structure of S/Cu(111), *Phys. Rev. B* 64 (2001) 155406.
13. H. Walen, D.J. Liu, J. Oh, H. Lim, J.W. Evans, Y. Kim, P.A. Thiel, Reconstruction of steps on the Cu(111) surface induced by sulfur, *J. Chem. Phys.* 142 (2015) 194711.

14. M. Shen, D.J. Liu, C.J. Jenks, P.A. Thiel, Novel self-organized structure of a Ag-S complex on the Ag(111) surface below room temperature, *J. Phys. Chem. C* 112 (2008) 4281–4290.
15. P. J. Feibelman, Formation and diffusion of S-decorated Cu clusters on Cu(111), *Phys. Rev. Lett.* 85 (2000) 606.
16. M. Shen, D. J. Liu, C. J. Jenks, P. A. Thiel, J. W. Evans, Accelerated coarsening of Ag adatom islands on Ag(111) due to trace amounts of S: mass-transport mediated by Ag-S complexes, *J. Chem. Phys.* 130 (2009) 094701.
17. M. Foss, R. Feidenhans'l, M. Nielsen, E. Findeisen, T. Buslaps, R.L. Johnson, F. Besenbacher, Sulfur induced Cu₄ tetramers on Cu(111), *Surf. Sci.* 388 (1997) 5–14.
18. J.S. Boschen, J. Lee, T.L. Windus, J.W. Evans, P.A. Thiel, D.J. Liu, Comparison of S-adsorption on (111) and (100) facets of Cu nanoclusters, *J. Chem. Phys.* 145 (2016) 164312.
19. H. Walen, D. J. Liu, J. Oh, H. Lim, J. W. Evans, C. M. Aikens, Y. Kim, P. A. Thiel, Cu₂S₃ complex on Cu(111) as a candidate for mass transport enhancement, *Phys. Rev. B* 91 (2015) 045426.
20. S.M. Russell, Y. Kim, D.J. Liu, J.W. Evans, P.A. Thiel, Communication: Structure, formation, and equilibration of ensembles of Ag-S complexes on an Ag surface, *J. Chem. Phys.* 138 (2013) 071101.
21. K. Morgenstern, E. Lægsgaard, F. Besenbacher, Sintering of cobalt nanoclusters on Ag(111) by sulfur: formation of one-, two-, and three-dimensional cobalt sulfide, *Surf. Sci.* 602 (2008) 661–670.
22. J. Kibsgaard, K. Morgenstern, E. Lægsgaard, J.V. Lauritsen, F. Besenbacher, Restructuring of cobalt nanoparticles induced by formation and diffusion of monodisperse metal-sulfur complexes, *Phys. Rev. Lett.* 100 (2008) 116104.
23. G. Kresse, J. Hafner, *Ab initio* molecular dynamics for liquid metals, *Phys. Rev. B* 47 (1993) R558–R561.
24. G. Kresse, J. Hafner, *Ab initio* molecular-dynamics simulations of the liquid-metal-amorphous-semiconductor transition in germanium, *Phys. Rev. B* 49 (1994) 14251.
25. P.E. Blöchl, Projector augmented-wave method, *Phys. Rev. B* 50 (1994) 17953–17979.
26. G. Kresse, D. Joubert, From ultrasoft pseudopotentials to the projector augmented-wave method, *Phys. Rev. B* 59 (1999) 1758–1775.

27. J. P. Perdew, K. Burke, M. Ernzerhof, Generalized gradient approximation made simple, *Phys. Rev. Lett.* 77 (1996) 3865–3868. Erratum-ibid. 78, 1396 (1997).
28. C. Adamo, V. Barone, Toward reliable density functional methods without adjustable parameters: the PBE0 model, *J. Chem. Phys.* 110 (1999) 6158–6170.
29. D.J. Liu, DFT analysis of key energetics in metal homoepitaxy: quantum size effects in periodic slab calculations, *Phys. Rev. B* 81 (2010) 035415.
30. V. Fiorentini, M. Methfessel, Extracting convergent surface energies from slab calculations, *J. Phys. Conds. Matter* 8 (1996) 6525–6529.
31. M. Valiev, E. Bylaska, N. Govind, K. Kowalski, T. Straatsma, H. van Dam, D. Wang, J. Nieplocha, E. Apra, T. Windus, W. de Jong, NWChem: a comprehensive and scalable open-source solution for large scale molecular simulations, *Comput. Phys. Commun.* 181 (2010) 1477–1489.
32. P.J. Hay, W.R. Wadt, *Ab initio* effective core potentials for molecular calculations. potentials for the transition metals atoms Sc to Hg, *J. Chem. Phys.* 82 (1985) 270–283.
33. W.R. Wadt, P.J. Hay, *Ab initio* effective core potentials for molecular calculations. potentials for the main group elements Na to Bi, *J. Chem. Phys.* 82 (1985) 284–298.
34. P.J. Hay, W.R. Wadt, *Ab initio* effective core potentials for molecular calculations. potentials for K to Au including the outermost core orbitals, *J. Chem. Phys.* 82 (1985) 299–310.
35. A.D. McLean, G.S. Chandler, Contracted Gaussian basis sets for molecular calculations. i. second row atoms, $Z=11-18$, *J. Chem. Phys.* 72 (1980) 5639–5648.
36. R. Krishnan, J.S. Binkley, R. Seeger, J.A. Pople, Self-consistent molecular orbital methods. xx. a basis set for correlated wave functions, *J. Chem. Phys.* 72 (1980) 650–654.
37. T. Clark, J. Chandrasekhar, G.W. Spitznagel, P. von Ragué Schleyer, Efficient diffuse function-augmented basis sets for anion calculations. iii. the 3-21+G basis set for first-row elements, Li-F, *J. Comput. Chem.* 4 (1983) 294–301.
38. F. Weigend, R. Ahlrichs, Balanced basis sets of split valence, triple zeta valence and quadruple zeta valence quality for H to Rn: design and assessment of accuracy, *Phys. Chem. Chem. Phys.* 7 (2005) 3297.
39. D. Andrae, U. Häußermann, M. Dolg, H. Stoll, H. Preuß, Energy-adjusted *Ab initio* pseudopotentials for the second and third row transition elements: molecular test for $m2$ ($m=ag, au$) and MH ($m=ru, os$), *Theor. Chim. Acta* 78 (1991) 247–266.

40. D. Rappoport, F. Furche, Property-optimized Gaussian basis sets for molecular response calculations, *J. Chem. Phys.* 133 (2010) 134105.
41. Experimental $E_c = 3.81, 2.95, 3.49,$ and 4.44 eV for Au, Ag, Cu, and Ni, respectively, in: C. Kittel (Ed.), *Introduction to Solid State Physics*, Wiley, New York, 2004.
42. E.J. Baerends, V. Branchadell, M. Sodupe, Atomic reference energies for density functional calculations, *Chem. Phys. Lett.* 265 (1997) 481–489.
43. E.R. Johnson, R.M. Dickson, A.D. Becke, Density functionals and transition-metal atoms, *J. Chem. Phys.* 126 (2007) 184104.
44. K.P. Jensen, B.O. Roos, U. Ryde, Performance of density functionals for first row transition metal systems, *J. Chem. Phys.* 126 (2007) 014103.
45. P.A. Thiel, M. Shen, D.J. Liu, J.W. Evans, Coarsening of two-dimensional nanoclusters on metal surfaces, *J. Phys. Chem. C* 113 (2009) 5047–5067.

CHAPTER 6. QUANTUM CHEMISTRY COMMON DRIVER AND DATABASES (QCDB): NWCHEM INTERFACE

Abstract

Quantum Chemistry Common Driver and DataBases (QCDB) is a program that contains generalized built-in interfaces of multiple codes (PSI4, GAMESS, NWChem, CFOUR, etc) allowing any of these quantum chemistry programs to be driven in a common manner. Before generalizing, interfaces for NWChem, GAMESS, and CFOUR were built in the existing driver in PSI4 and specifically the detail of the NWChem interface (composition of the interface, building procedures, functionalities, and so on) is described in this Chapter. The successfully built-in interfaces in PSI4 supports the future work of generalizing to the independent program, QCDB.

1. Introduction

Computational quantum chemistry has been very popular not only in chemistry but also in broad science areas. With this demand, high accuracy and diverse functionalities of quantum chemistry software becomes important and are requested by many users. Each quantum chemistry software is mostly developed independently so that it has different focuses and features in development. Even though a program has unique features in a certain area, sometimes it does not have needed functionalities in another area; although another program has that functionality. In this case, users need to choose what to sacrifice - either being satisfied with available capabilities of the program they use or spending time to learn another program that meets their needs. Since it is not possible that a program has all of the capabilities that other programs have, building interfaces that allow connections between different programs is more effective than solving the unending dilemma. There have been efforts to create such libraries or interfaces. For instance, GAMESS^{1,2} has interfaces with the

Martinez FMS and the Lischka Newton-X codes³ that can be called through GAMESS.

Another example is the PSI4⁴ driver that is interfaced with CFOUR.⁵

The initial idea of this research was started from the latter example. Not only the interface with CFOUR is of interest, but PSI4 also has a lot of built-in interfaces and packages that allow one to interact with methods in other programs. It is also user-friendly and easy-to-use since it is mostly written in Python.⁶ One of my collaborators, Lori Burns, succeeded in building the interface of CFOUR in the PSI4 driver. Through the interface, PSI4 users are able to use theories and functionalities not existing in PSI4 but that are in the CFOUR program, such as second-order Vibrational Perturbation Theory (VPT2) and open-shell coupled-cluster (CC) gradients and frequencies. The interface also supports flexibility for input file formats. More detail regarding the flexibility is discussed below.

The fundamental goal of my research is to separate the driver containing built-in interfaces out from PSI4 and generalize it to an independent program – the so-called quantum chemistry common driver and databases (QCDB). QCDB will use a common format for input and output as *Figure 6.1* shows. QCDB will contain built-in interfaces for multiple quantum chemistry programs (such as CFOUR, GAMESS, NWChem, etc.) and be able to generate input files for multiple computational codes using a common input. Also, it will be able to parse the output of those codes to produce a common output. The flexibility of the input and output format reduces extra work for users to execute programs and manage data regardless of program. A more advantageous feature is that users are able to perform calculations across multiple programs such as mixing theories existing in different codes and performing tasks (energy, geometry optimization, etc.) through different programs.

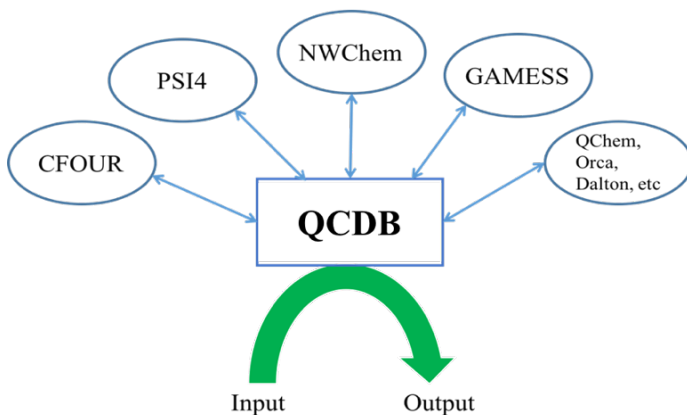


Figure 6.1 Schematic diagram of quantum chemistry common driver and databases (QCDB).

Before generalizing the PSI4 driver, adding interfaces for NWChem and GAMESS (worked by Nuwan de Silva) similar to that for CFOUR to the PSI4 driver were performed. As *Figure 6.2* shows, the scheme of the NWChem⁷ and GAMESS interfaces is similar to that for CFOUR. This Chapter mainly discusses about the first step to build an NWChem interface in PSI4 focusing on describing how the built-in NWChem interface works in PSI4 and what functionalities are available.

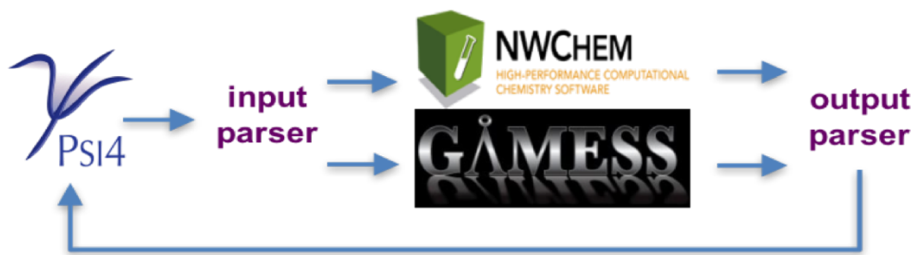


Figure 6.2 Schematic diagram of NWChem and GAMESS interfaces in PSI4.

2. NWChem Interface

The NWChem interface built in PSI4 can be divided into four parts: input parser, NWChem translator, output parser, and data management. As *Figure 6.2* shows, PSI4 first calls an input parser once a job is submitted. To start a job, three different input formats are readable: pure PSI4, pure NWChem, and mixed. Pure means the program's own input format

and mixed means coexistence of two different input formats. Pure NWChem keywords are exactly the same keywords for NWChem but should be listed inside of an ‘nwchem’ bracket (nwchem { ... }). This bracket indicates keywords inside do not need a translator. The great advantage of this is every NWChem keyword is available. Pure PSI4 keywords follow the PSI4 input format. However to drive an NWChem calculation, the keywords from PSI4 are sent to the NWChem translator to be translated into NWChem-speak. The compatible PSI4 keywords are listed in *Table 6.2 of the Appendix B*.

After parsing and translating the input are done, the code is run to produce the output and the output parser starts to harvest data such as calculated energies, nuclear repulsion energy, gradients, and so on. Lastly, all parsed information is saved for data management. Currently, harvested information is saved in a python dictionary format under the name ‘NWCHEM’. In this section, more detail will be provided on how different input formats work according to the keywords with examples.

2.1. Molecules

Molecule keywords include information for charge, multiplicity, geometry, geometry units, and symmetry. All keywords can be set by three ways (pure PSI4, pure NWChem, and mixed). The molecule keywords in PSI4 and NWChem are mostly in common (having similar names and meanings), so pure PSI4 keywords in molecule {} can be fully translated into NWChem keywords. In other words, the keywords are set to PSI4 defaults if not specified. The available pure PSI4 keywords are listed in *Table 6.2 of the Appendix B*. Note that the symmetry is also detected by PSI4 when pure PSI4 molecule keywords are used. Pure PSI4 molecule keywords have to be used if a calculation is using PSI4 functionality such as the PSI4 geometry optimization module (i.e. optimize (‘nwc-method’)). This is necessary because of the difference in the orientation of coordinates between PSI4 and

NWChem. The following is an example of molecule keywords written in the PSI4 input format actually used for a calculation.

```
molecule {  
O  
H 1 R  
H 1 R 2 A  
R=0.958  
A=104.5 }
```

This molecule block is sent to the input parser to generate an input for NWChem and the following is the part of the NWChem input generated by the interface.

```
geometry noautosym nocenter units Angstrom  
O 0.000000000000 0.000000000000 -0.065638538099  
H 0.000000000000 -0.757480611647 0.520865616174  
H 0.000000000000 0.757480611647 0.520865616174  
symmetry c2v  
end  
charge 0  
scf  
nopen 0  
end
```

As shown in the examples, ‘noautosym’ and ‘nocenter’ keywords are turned on to avoid reorientation of coordinates and to use the symmetry that the PSI4 driver detected. Since units for the coordinates are not specified in the first sample above, the default unit of PSI4, Angstrom, is printed. Likewise, charge and spin multiplicity are also translated into default values, ‘charge 0’ and ‘nopen 0’. In terms of spin multiplicity, NWChem has different keywords depending on which theory is used. The example above is an Hartree-Fock (HF) calculation so the (default) multiplicity keyword of PSI4 is translated into the ‘nopen’ keyword. If the calculation was a DFT calculation, the ‘mult’ keyword would be generated inside the dft block. The translation is automatically performed by the NWChem interface so no extra work has to be done by the user.

To set different values for symmetry, unit, charge, and multiplicity, the user could use the usual PSI4 input file. For NWChem users who are not familiar with PSI4, they could add ‘nwchem_’ before nwchem keywords (such as nwchem_charge, nwchem_scf_nopen, nwchem_dft_mult) with the value for the keyword or they could use the nwchem bracket, ‘nwchem {...}’, as a pure NWChem-speak (such as nwchem {charge 0}, nwchem {scf; nopen; 0}, nwchem {dft; mult; 1}).

2.2. Basis Sets

Flexibility in basis set keywords is very important to improve interoperability between different programs. The current default is to read basis sets in the PSI4 library and translate into an NWChem readable basis set format. If a user wants to call basis sets in the NWChem library, the user must specify the basis set inside the nwchem bracket, ‘nwchem {...}’. For instance, one can use ‘set basis cc-pvdz’ to use the PSI4 cc-pvdz basis set (for every atom) or ‘nwchem {* library cc-pvdz}’ to use the NWChem basis set. To assign different basis sets for different atoms, one could use the usual PSI4 input format,

```
basis {
  assign aug-cc-pvdz
  assign H cc-pvdz
}
```

using aug-cc-pvdz for all atoms but cc-pvdz for H atoms. Then, the corresponding basis set is pulled from the library in PSI4 and translated into the NWChem basis set format as the interface always does. If one wanted to use the NWChem basis sets, the input would be like the following.

```
nwchem {
basis
* library aug-cc-pvdz except H
H library cc-pvdz
end
}
```

The completely transformed NWChem input is always echoed by default so one could see the transformed basis sets from the NWChem output.

2.3. Theories

Current available theories are Hartree-Fock (HF), 2nd-order Møller–Plesset perturbation theory (non-density-fitting) (MP2), Direct MP2, resolution of the identity approximation MP2 (RIMP2), density functional theory (DFT), coupled cluster (CC) theories such as CCSD, CCSD(T), etc and time dependent DFT (TDDFT). Higher level theories (CCSDT, CCSDTQ, CCSDT(Q), CISD, CISDT, EOM-CCSD, etc.) are also available through the TCE keyword. Available keywords for each theory is also listed in the *keyword section of the Appendix B*.

One of the advantageous features of the current version of the interface is excited state calculations, EOM-CC, are available. Since NWChem has varieties of EOM-CC that most programs do not have yet, it is very exciting to add these functionalities into the interface. For example, users could optimize the geometry of a molecule using EOM-CCSDTQ energies and gradients computed by NWChem and the PSI4 geometry optimizer. More detail is discussed in the Conclusion section since this is a part of the potential application for future works.

Another feature is that the interface has a map of DFT functionals between PSI4 and other programs. Most names of DFT functionals are in common regardless of the program, but some functionals are defined as different names or have the same name but are actually different. Currently, most of the DFT functionals in PSI4 are mapped to NWChem DFT functionals so the names of PSI4 functionals are translated into the corresponding functionals

of NWChem. Here is an example of input for a DFT energy calculation for water using B2PLYP functional.

```
memory 300 mb
molecule h2o {
0 1
O
H 1 1.0
H 1 1.0 2 104.5
}
set {
basis cc-pvdz
df_scf_guess false
scf_type direct
dft_spherical_points 302
dft_radial_points 99
reference rks
}
energy('nwc-b2plyp')
```

DFT functionals can be set by keyword 'dft_functional' as well but the argument of energy must be 'nwc-dft' in that case. Once this input file is sent to the input parser, the following NWChem input is generated.

```
echo
geometry noautosym nocenter units Angstrom
O 0.000000000000 0.000000000000 -0.068516219310
H 0.000000000000 -0.790689573744 0.543701060724
H 0.000000000000 0.790689573744 0.543701060724
symmetry c2v
end
basis spherical
* library cc-pvdz
end
charge 0
memory 300 mb
dft
convergence density 1e-08 energy 1e-08
grid lebedev 99 11
direct
xc HFexch 0.53 becke88 0.47 lyp 0.73 mp2 0.27
end
task dft energy
```

For more detail, a list of mapped PSI4 DFT functionals and their corresponding values for NWChem is available in *Table 6.3 of the Appendix B*. Even if the functional does not exist in NWChem, it can be customized using the NWChem `dft xc` keyword. The values for `dft xc` keyword must be an array type such as `'nwchem_dft_xc [HFexch, 0.53, becke88, 0.47, lyp, 0.73, mp2, 0.27]'`.

2.4. Tasks

The available tasks of the NWChem interface are energy, gradient, and geometry optimization. Geometry optimization means calculating an NWChem energy and gradient at each iteration but using the PSI4 geometry optimizer. In other words, the geometry of each step in the optimization is determined by PSI4 based on energy and gradient results computed by NWChem.

Computed energies and gradients are saved in a dictionary so all values are easily callable through `'get_variable'`. For example, one can get the value of variables such as `'hf total energy'`, `'ccsd(t) total energy'`, `'ccsd(t) correlational energy'`, and so on for CCSD(T) calculations. To test and evaluate computed values through the interface, one could use `'compare_values'` to compare with values computed from pure NWChem such as

```
compare_values(-76.026760737445, get_variable('hf total energy'), 6, 'HF')
compare_values(-76.230777733749719, get_variable('mp2 total energy'), 6, 'MP2')
compare_values(-76.240102010002232, get_variable('ccsd total energy'), 6, 'CCSD')
compare_values(-0.213341272556766, get_variable('ccsd correlation energy'), 6, 'CCSD
corl')
compare_values(-76.243161551653742, get_variable('ccsd(t) total energy'), 6,
'CCSD(T)')
compare_values(-0.2164008142, get_variable('ccsd(t) correlation energy'), 6, 'CCSD(T)
corl')
```

The first value is one the users want to compare with, the second is the computed value, the third is how many decimal points of accuracy for the comparison, and the last is a name of the value. The last one is to indicate what the value is once the comparison results are printed

out in the output; so it can be customized by users. A list of available values of 'get_variables' is found in the *Section A.6 of the Appendix A*.

2.5. Additional Functionalities

One of the potential functionalities to add is interoperability of molecular orbitals between programs. As one of the efforts to achieve that, Transforming NWChem molecular orbitals to PSI4-readable molecular orbitals have been worked. NWChem generates a Fortran binary file (.movecs) which contains information on molecular orbitals and energies. Since the NWChem interface is present in the PSI4 driver currently, there are a couple of things to be done to make the file readable. First, the NWChem interface has to read the movecs file using Python. Second, the NWChem molecular orbital information needs to be transformed to a .180.npz file (compressed numpy binary file) that PSI4 actually reads as a molecular orbital initial guess. Currently, PSI4 can use NWChem molecular orbitals of both closed and open-shell systems (including unrestricted) as an initial guess when Cartesian functions are used. The following is an input example where PSI4 reads previously obtained NWChem molecular orbitals.

```
# nwchem hf/6-31g* water energy calculation
print ('NWChem execution')
memory 400 mb
molecule {
O
H 1 R
H 1 R 2 A

R=0.958
A=104.5
}
set basis 6-31g*
scf_e, scf_wfn = energy('nwc-hf', return_wfn=True)

# psi4 HF/6-31g* on water energy calculation reading previously computed nwchem
MOs
print ('psi4 execution')
```

```

memory 400 mb
molecule {
O
H 1 R
H 1 R 2 A

R=0.958
A=104.5
symmetry c1
}
#To get the same energy from psi4, add commands below
set df_scf_guess false
set scf_type direct
#
set scf_guess read
set basis 6-31g*
energy ('scf')

```

And the following is part of the PSI4 output reading NWChem molecular orbitals as a SCF guess.

SCF Guess: Orbitals guess was supplied from a previous computation.

==> Iterations <==

	Total Energy	Delta E	RMS [F,P]
@RHF iter 0:	-76.01049622577717	-7.60105e+01	8.49127e-09
@RHF iter 1:	-76.01049630405174	-7.82746e-08	1.19276e-09
...			

Energy converged.

The example above used the same basis set for both NWChem and PSI4, but PSI4 can also successfully read molecular orbitals computed by NWChem using different basis set (mostly smaller basis set). The .180.npz file contains the information on the basis set used for the original NWChem calculation. So if one uses the cc-pvdz basis set for the PSI4 calculation instead of 6-31g*, the PSI4 output would be

==> Primary Basis <==

Basis Set: CC-PVDZ
Blend: CC-PVDZ
Number of shells: 12
Number of basis function: 24
Number of Cartesian functions: 25
Spherical Harmonics?: true
Max angular momentum: 2

Reading orbitals from file 180, projecting to new basis.

=> Loading Basis Set <=

Name: 6-31G*
Role: ORBITAL
Keyword: BASIS
atoms 1 entry O line 137 file /psi4/objdir/stage/usr/local/psi4/share/psi4/basis/6-31gs.gbs
atoms 2-3 entry H line 36 file /psi4/objdir/stage/usr/local/psi4/share/psi4/basis/6-31gs.gbs

Computing basis projection from 6-31G* to CC-PVDZ

The .180.npz file of NWChem molecular orbitals is created in the SCRATCH dictionary of PSI4 by default unless spherical functions are used. For spherical function, reordering of molecular orbitals must still be completed, which can be a potential development in the future.

3. Conclusion

We have built the NWChem and GAMESS (completed by Dr. de Silva) interfaces successfully in the PSI4 driver that contains the input and output parser that allows flexibility in their formats. Also, unique theories/methods of each program, such as EOM-CC in NWChem and effective fragment potential (EFP) or effective fragment molecular orbital (EFMO) methods in GAMESS, can be driven through the PSI4 driver.

Before the driver is generalized to the common driver, there will be a couple of

applications to show how the common driver can be utilized. As shortly mentioned in Section 2.3, geometry optimization can be performed in PSI4 using EOM-CCSDTQ of NWChem. After the optimized geometry is found, we could perform additional corrections using the diagonal Born-Oppenheimer capability of CFOUR and possible analysis of GAMESS such as DK3 relativistic corrections. Since EFMO is one of the unique methods in GAMESS, we could also combine the method for more accurate but efficient computation for large systems such as proteins, DNA, and so on.

To achieve the fundamental goal, the most important remaining work is to generalize the driver and separate it out from the PSI4. This is work that is being carried out by my collaborator Lori Burns. Additionally, there are still theories and keywords not added yet, so improving capabilities in those remain for the future work. Also, providing interoperability to computed molecular orbitals regardless of whether one is using Cartesian or spherical function can be further developed.

Acknowledgements

This work was supported by a Software Infrastructure (SI2) grant from the National Science Foundation (ACI-1047772).

References

1. Schmidt, M. W.; Baldridge, K. K.; Boatz, J. A.; Elbert, S. T.; Gordon, M. S.; Jensen, J. H.; Koseki, S.; Matsunaga, N.; Nguyen, K. A.; Su, S.; Windus, T. L.; Dupuis, M.; Montgomery, J. A. *Journal of Computational Chemistry* **1993**, *14* (11), 1347–1363.
2. Gordon, M. S.; Schmidt, M. W. *Theory and Applications of Computational Chemistry* **2005**, 1167–1189.
3. Barbatti, M.; Ruckebauer, M.; Plasser, F.; Pittner, J.; Granucci, G.; Persico, M.; Lischka, H. *Wiley Interdisciplinary Reviews: Computational Molecular Science* **2013**, *4* (1), 26–33.

4. Turney, J. M.; Simmonett, A. C.; Parrish, R. M.; Hohenstein, E. G.; Evangelista, F. A.; Fermann, J. T.; Mintz, B. J.; Burns, L. A.; Wilke, J. J.; Abrams, M. L.; Russ, N. J.; Leininger, M. L.; Janssen, C. L.; Seidl, E. T.; Allen, W. D.; Schaefer, H. F.; King, R. A.; Valeev, E. F.; Sherrill, C. D.; Crawford, T. D. *Wiley Interdisciplinary Reviews: Computational Molecular Science* **2011**, 2 (4), 556–565.
5. CFOUR, a quantum chemical program package written by J.F. Stanton, J. Gauss, L. Cheng, M.E. Harding, D.A. Matthews, P.G. Szalay with contributions from A.A. Auer, R.J. Bartlett, U. Benedikt, C. Berger, D.E. Bernholdt, Y.J. Bomble, O. Christiansen, F. Engel, R. Faber, M. Heckert, O. Heun, M. Hilgenberg, C. Huber, T.-C. Jagau, D. Jonsson, J. Jusélius, T. Kirsch, K. Klein, W.J. Lauderdale, F. Lipparini, T. Metzroth, L.A. Mück, D.P. O'Neill, D.R. Price, E. Prochnow, C. Puzzarini, K. Ruud, F. Schiffmann, W. Schwalbach, C. Simmons, S. Stopkowicz, A. Tajti, J. Vázquez, F. Wang, J.D. Watts and the integral packages *MOLECULE* (J. Almlöf and P.R. Taylor), *PROPS* (P.R. Taylor), *ABACUS* (T. Helgaker, H.J. Aa. Jensen, P. Jørgensen, and J. Olsen), and ECP routines by A. V. Mitin and C. van Wüllen. For the current version, see <http://www.cfour.de>.
6. Parrish, R. M.; Burns, L. A.; Smith, D. G. A.; Simmonett, A. C.; Deprince, A. E.; Hohenstein, E. G.; Bozkaya, U.; Sokolov, A. Y.; Remigio, R. D.; Richard, R. M.; Gonthier, J. F.; James, A. M.; McAlexander, H. R.; Kumar, A.; Saitow, M.; Wang, X.; Pritchard, B. P.; Verma, P.; Schaefer, H. F.; Patkowski, K.; King, R. A.; Valeev, E. F.; Evangelista, F. A.; Turney, J. M.; Crawford, T. D.; Sherrill, C. D. *Journal of Chemical Theory and Computation* **2017**, 13 (7), 3185–3197.
7. Kendall, R. A.; Aprà, E.; Bernholdt, D. E.; Bylaska, E. J.; Dupuis, M.; Fann, G. I.; Harrison, R. J.; Ju, J.; Nichols, J. A.; Nieplocha, J.; Straatsma, T.; Windus, T. L.; Wong, A. T. *Computer Physics Communications* **2000**, 128 (1-2), 260–283.

Appendix A. Interface to NWChem

A.1. Installation

1) PSI4

Follow the instruction provided in PSI4 GitHub (<https://github.com/psi4/psi4.git>) to get source and website (http://psicode.org/psi4manual/master/build_planning.html) to compile and install the source.

2) NWChem

Follow the instructions provided with the NWChem download or website (<http://www.nwchem-sw.org/index.php/Download>) to compile the source. To call NWChem

successfully, users must set NWChem executable (*nwchem*) to PATH or PSIPATH.

A.2. NWChem for PSI4 Users

Setting NWChem keywords (memory, molecule, basis set, etc.) are same as usual PSI4 if not specified below.

1) Memory can be specified to stack, heap, global through “nwchem_memory” keyword.

2) Symmetry of molecule is detected by PSI4. If one wants to use NWChem symmetry detector, use *nwchem {...}* and write geometry input in pure NWChem format inside the bracket.

3) Basis sets are loaded from the PSI4 library by default.

4) Set NWChem keywords just like PSI4 keywords. The general format of keywords follows “nwchem_theory_the name of keyword”. The names of keywords are the same as the usual NWChem keywords, except ‘NWCHEM_TCE’ and NWCHEM_TCE_MODULE’. For more detail of keywords, check Section B.2 in *Appendix B*. Detailed information for each keyword can be also found from the NWChem documentation (http://www.nwchem-sw.org/index.php/Release66:NWChem_Documentation). Or check the test cases at {top-level-psi4-dir}/psi4/tests/nwchem/

5) To specify task, prepend “nwc-” to the method argument such as energy (‘nwc-hf’). Available methods are listed in the *Table 7.1*.

A.3. PSI4 for NWChem Users

Set all of keywords as usual NWChem input format but write them inside the NWChem curly bracket *nwchem {...}* as the following example shows.

```
nwchem {
memory 400 mb
geometry
```

```

O  0.000000000000  0.000000000000 -0.065638538099
H  0.000000000000 -0.757480611647  0.520865616174
H  0.000000000000  0.757480611647  0.520865616174
end
basis spherical
* library cc-pvdz
end
scf
  rhf
  thresh 1.0e-8
  nopen 0
end
task scf energy
}
energy('nwchem')

```

The rest of the process for the calculation is similar to the PSI4/CFOUR interface (<http://www.psicode.org/psi4manual/1.1/cfour.html>). For more detail, see examples at `/psi4/tests/nwchem/`. If task command is specified in `nwchem {...}` as the sample above, the argument of `energy ()` has to be 'nwchem'.

A.4. Basic Rules for NWChem Values

1) Array type

If a value type is array, write values the same way as NWChem but as an array type.

For instance, NWChem-speak values for keyword “vectors” are written as:

```
vectors input try1.movecs swap 173 175 174 176 output try2.movecs
```

This must be written as an array type either inside a set of `{...}` or with the set command:

```
set {
nwchem_method_vectors [input, try1.movecs, swap, 173, 175, 174, 176, output,
try2.movecs]
}
```

```
set nwchem_method_vectors [input, try1.movecs, swap, 173, 175, 174, 176, output,
try2.movecs]
```

All array types follow this rule. In other words, use comma instead of space.

2) String type, True/False

NWChem has keywords that have no values, such as “diis” and “direct” in the SCF module. The value type is string but the role is the same as boolean. To use, set the value as “true”. Here is an example:

```
set nwchem_scf_direct true
set nwchem_scf_diis true
```

These will be printed out as

```
scf
direct
diis
end
```

A.5. Capabilities

The current available tasks are energy, gradient, and geometry optimization. To perform geometry optimization, use “optimize”. Currently, optimized geometries are performed using NWChem gradient calculations. *Table 6.1* describes the methods that are available through the interface.

1) Tensor contraction engine (TCE) module

As the Table 6.1 describes, CCSD, EOM-CCSD and CCSD(T) in NWChem can be driven either through TCE module or its own module. If a method is specified as either ‘nwc-ccsd’ or ‘nwc-ccsd(t)’, the NWChem interface would drive a calculation using its own module (‘task ccsd’ or ‘task ccsd(t)’ in NWChem-speak) by default. To use TCE module for those methods, ‘NWCHEM_TCE’ keyword must be set ‘ON’. Since other CC theories, such as CCSDT and CCSDTQ, can be driven only by TCE module in NWChem, TCE will be used by default (i.e., nwchem_tce on by default). For example, if a user wants to perform nwc-ccsd(t), there are two ways to write an input. One is to use CCSD(T) module instead of TCE and the input can be written as an example below.

Table 6.1 List of available methods for energy, gradient, and geometry optimization.

name	available NWChem methods
nwc-hf	Hartree-Fock (HF) (non-density-fitting)
nwc-dft	Density functional theory (DFT)
<i>nwc-name of functional</i>	Density functional theory (DFT) using the functional (e.g nwc-pbe). Available options are listed in the <i>Table 7.3</i> .
nwc-mp2	2nd-order Møller–Plesset perturbation theory (non-density-fitting) (MP2)
nwc-ccsd	Coupled-cluster singles and doubles (CCSD) or Tensor Contraction Engine (TCE)
nwc-ccsd(t)	CCSD with perturbative triples (CCSD(T)) or Tensor Contraction Engine (TCE)
nwc-ccsdt	coupled-cluster singles, doubles, and triples (CCSDT) driven through Tensor Contraction Engine (TCE)
nwc-ccsdtq	coupled-cluster singles, doubles, triples, and quadruples (CCSDTQ) driven through Tensor Contraction Engine (TCE)
nwc-eom-ccsd	Unrestricted equation-of-motion coupled-cluster singles and doubles (EOM-CCSD) or Tensor Contraction Engine (TCE)
nwc-eom-ccsdt	Unrestricted equation-of-motion coupled-cluster singles, doubles, and triples (EOM-CCSDT) driven through Tensor Contraction Engine (TCE)
nwc-eom-ccsdtq	Unrestricted equation-of-motion coupled-cluster singles, doubles, triples, and quadruples (EOM-CCSDTQ) driven through Tensor Contraction Engine (TCE)
nwc-tddft	Time dependent density functional theory (TDDFT)
nwchem	expert full control over nwchem program

```

molecule {
O
H 1 R
H 1 R 2 A

R=0.958
A=104.5
}
set {
basis cc-pvdz
reference rhf
nwchem_scf_thresh 1.0e-12
nwchem_ccsd_thresh 1.0e-12

```

```

}
energy('nwc-ccsd(t)')

```

If 'NWChem_TCE' keyword is not specified in the input as the example above, 'energy('nwc-ccsd(t)')' will drive the CCSD(T) module by default so the task command will be written as 'task ccsd(t) energy'. The other way is to use TCE module for CCSD(T) by setting 'nwchem_tce on' and the input would be

```

molecule {
O
H 1 R
H 1 R 2 A

R=0.958
A=104.5
}
set {
basis cc-pvdz
reference rhf
nwchem_scf_thresh 1.0e-12
nwchem_tce_thresh 1.0e-12
nwchem_tce on
}
energy('nwc-ccsd(t)')

```

In this case, the interface would specify the CC theory inside of NWChem tce block, 'tce; ccsd(t); end', and write task command, 'task tce energy', on the translated NWChem input.

For other theories, (EOM-)CCSDT and (EOM-)CCSDTQ, TCE module is the only option so the keyword 'NWChem_TCE' is always set 'ON' by default and the task command would start with 'task tce'. For instance, to perform EOM-CCSDTQ energy calculation, the input

```

set {
reference rhf
e_convergence 10 #or nwchem_scf_thresh 1.0e-10
nwchem_scf_tol2e 1.0e-10
nwchem_memory [total, 1500, stack, 400, heap, 400, global, 700, mb]
}

```

```

set {
nwchem_tce_nroots 1
}
energy ('nwc-eom-ccsdTq')

```

would be translated into

```

scf
RHF
thresh 1e-10
tol2e 1e-10
end

```

```

tce
ccsdTq
nroots 1
end

```

task tce energy

Note that TCE module is used by default though 'NWCHEM_TCE' keyword is not specified on the original input, different from 'nwc-(eom-)ccsd' and 'nwc-ccsd(t)'.

A.6. List of Available PSI Variables for NWChem Interface

HF TOTAL ENERGY

NUCLEAR REPULSION ENERGY

DFT TOTAL ENERGY

MP2 CORRELATION ENERGY

MP2 SAME-SPIN CORRELATION ENERGY

MP2 OPPOSITE-SPIN CORRELATION ENERGY

MP2 TOTAL ENERGY

CCSD CORRELATION ENERGY

CCSD TOTAL ENERGY

CCSDT CORRELATION ENERGY

CCSDT TOTAL ENERGY

CCSDTQ CORRELATION ENERGY

CCSDTQ TOTAL ENERGY

(T) CORRECTION ENERGY

CCSD(T) CORRELATION ENERGY

CCSD(T) TOTAL ENERGY

EOM-CCSD ROOT 0 -> ROOT %(number) EXCITATION ENERGY - %(symmetry)

SYMMETRY

EOM-CCSD ROOT 0 -> ROOT %(number) TOTAL ENERGY - %(symmetry)

SYMMETRY

TDDFT ROOT %(number) %(singlet or triplet) %(symmetry) EXCITATION ENERGY

TDDFT ROOT %(number) %(singlet or triplet) %(symmetry) EXCITED STATE ENERGY

TDDFT ROOT %(number) DIPOLE X

TDDFT ROOT %(number) DIPOLE Y

TDDFT ROOT %(number) DIPOLE Z

TDDFT ROOT %(number) QUADRUPOLE XX

TDDFT ROOT %(number) QUADRUPOLE XY

TDDFT ROOT %(number) QUADRUPOLE XZ

TDDFT ROOT %(number) QUADRUPOLE YY

TDDFT ROOT %(number) QUADRUPOLE YZ

TDDFT ROOT %(number) QUADRUPOLE ZZ

CURRENT DIPOLE X

CURRENT DIPOLE Y

CURRENT DIPOLE Z

CURRENT REFERENCE ENERGY (available for HF, MP2, DFT, CCSD, CCSDT, CCSDTQ, CCSD(T))

CURRENT CORRELATION ENERGY (available for CCSD, CCSDT, CCSDTQ, CCSD(T))

NWCHEM ERROR CODE

Appendix B. Keywords

B.1. Compatible Pure PSI4 Keywords

Commonly used HF and DFT PSI4 keywords are automatically translated into nwchem-speak without prepending the 'nwchem_' before the NWChem keywords. For instance, one can use either 'set multiplicity 1' (pure PSI4) or 'set nwchem_scf_nopen 0' ('nwchem_' prepended keyword) to set the multiplicity for the NWChem SCF calculation. The NWChem interface can recognize both keywords and translate into the adequate NWChem-speak, 'scf; nopen 0; end'. Available PSI4 keywords listed in the *Table 6.2*. Note that keywords shared by more than two methods in PSI4 (e.g. maxiter, multiplicity, etc.) are translated into the corresponding method counterparts.

1) Molecule keywords

Charge, multiplicity, geometry units are set from the active molecule. For multiplicity, the PSI4-NWChem interface is able to distinguish SCF and DFT multiplicity keywords by the method argument. All units (angstroms, bohr, a.u.) are available.

2) Basis set keywords

Set basis set as usual with PSI4 basis set commands. Basis sets are loaded from the PSI4 basis set library by default and printed out to NWChem-readable basis sets. To use spherical function, GLOBALS PUREAM keyword is available. If not specified, the value is determined by PSI4 basis set.

Table 6.2 List of compatible pure PSI4 keywords in the NWChem interface.

PSI4 keywords	'nwchem_' prepended keywords
memory	nwchem_memory
charge	nwchem_charge
multiplicity	nwchem_scf_nopen
	nwchem_dft_mult
reference	nwchem_scf
	nwchem_dft
d_convergence, e_convergence	nwchem_scf_thresh
	nwchem_dft_convergence
scf_type	nwchem_scf_direct
	nwchem_dft_direct
maxiter	nwchem_scf_maxiter
	nwchem_dft_iterations
dft_radical points, dft_spherical points	nwchem_dft_grid
dft_functional	nwchem_dft_xc

3) Map of DFT functionals

The listed DFT functionals in *Table 6.3* are available to drive NWChem DFT calculation. Either set keyword “dft_functional” or use method “nwc-name of functional”. Other functionals not listed must be specified through the keyword “nwchem_dft_xc [array type]”.

B.2. NWChem Input Keywords for the NWChem Interface

Available keywords for the NWChem interface are listed below with type and comments from interfaces if needed. Comments from the PSI4 interface might be more useful for original PSI4 users to understand how the NWChem keywords are used in PSI4. For NWChem users, NWChem comments would help to know how the keywords need to be used in PSI4. For more detail on the NWChem keyword descriptions, including defaults, check the NWChem website (http://www.nwchem-sw.org/index.php/Release66:NWChem_Documentation) or the NWChem 6.6 manual. If

Table 6.3 List of available DFT functionals through PSI4 keywords.

dft functional	nwchem dft xc
B1B95	B1B95
B1LYP	[HFexch, 0.25, becke88, 0.75, lyp]
B1PW91	[HFexch, 0.25, becke88, 0.75, perdew91]
B2PLYP	[HFexch, 0.53, becke88, 0.47, lyp, 0.73, mp2, 0.27]
B3LYP	B3LYP
B3LYP5	[vwn_5, 0.19, lyp, 0.81, HFexch, 0.20, slater, 0.8, becke88, nonlocal, 0.72]
B86BPBE	[becke86b, cpbe96]
B97	[becke97, HFexch, 0.1943]
B97-0	[becke97, HFexch, 0.1943]
B97-1	[becke97-1]
B97-1P	[becke97gga1, HFexch, 0.1500]
B97-2	[becke97-2]
B97-3	[becke97-3, HFexch, 0.2693]
B97-GGA1	[becke97gga1]
BHANDH	[beckehandh]
BHANDHLYP	[becke88, 0.500, HFexch, 0.500, lyp]
BHHLYP	[becke88, 0.500, HFexch, 0.500, lyp]
BLYP	[becke88, lyp]
BOP	BOP
BP86	[becke88, perdew86]
CAM-B3LYP	[xcamb88, 1.00, lyp, 0.81, vwn_5, 0.19, hfexch, 1.00\n, cam, 0.33, cam_alpha, 0.19, cam_beta, 0.46]
dIDF	dIDF
FT97	FT97
HCTH	HCTH
HCTH120	HCTH120
HCTH407P	HCTH407P
HCTHP14	HCTHP14
LRC-WPBE	[xwpbe, 1.00, cpbe96, 1.0, hfexch, 1.00\n, cam, 0.3, cam_alpha, 0.00, cam_beta, 1.00]
LRC-WPBEH	[xwpbe, 0.80, cpbe96, 1.0, hfexch, 1.00\n, cam, 0.2, cam_alpha, 0.20, cam_beta, 0.80]
M05	M05
M05-2X	M05-2X
M06	M06
M06-2X	M06-2X
M06-HF	M06-HF
M08-HX	M08-HX
M08-SO	M08-SO
M11	M11
M11-L	M11-L
MPW1B95	MPW1B95
MPW1K	MPW1K

Table 6.3 (continued).

dft functional	nwchem dft xc
MPW1PW	[mpw91, 0.75, HFexch, 0.25, perdew91]
MPWB1K	MPWB1K
MPWLYP1M	[mpw91, 0.95, HFexch, 0.05, lyp]
MPWLYP1W	[mpw91, vwn_5, 0.12, lyp, 0.88]
PBE	[xpbe96, cpbe96]
PBE0	PBE0
PBE0-13	[mpw91, 0.95, HFexch, 0.05, lyp]
PBEH	[xpbe96, 0.75, HFexch, 0.25, cpbe96]
PBELYP1W	[xpbe96, vwn_5, 0.26, lyp, 0.74]
PW6B95	PW6B95
PW86PBE	[xperdew86, cpbe96]
PW91	[xperdew91, perdew91]
PWB6K	PWB6K
TPSSH	[xctpssh]
TPSSLYP1W	[xtpss03, vwn_5, 0.26, lyp, 0.74]
WPBE	[xwpbe, 1.0, cpbe96, 1.0, HFexch, 1.0\n, cam, 0.40, cam_alpha, 0.0, cam_beta, 1.0]
XLYP	[slater, -0.0690, becke88, 0.722, xperdew91, 0.347, lyp]

keywords are GLOBALS, please refer to PSI4 keywords website

(http://www.psicode.org/psi4manual/1.1/autodoc_glossary_options_c.html).

1) NWChem internal

NWCHEM_CHARGE

- Type: integer

NWCHEM_MEMORY

PSI4 interface: Memory can be specified by stack, heap, and global. Follow the NWChem manual but write in array type. If not specified, memory is allocated according to installation-dependent defaults.

- Type: array

NWCHEM_RELATIVISTIC

- Type: array

PUREAM (GLOBALS)

GLOBALS – If true, spherical basis functions are used. The value is set from the PSI4 basis set database by default.

- Type: boolean

LITERAL_NWCHEM (GLOBALS)

GLOBALS – Similar to LITERAL_CFOUR. Text inside of *nwchem* {...} will be passed to NWChem program without translation.

- Type: string

2) SCF Keywords

NWCHEM_SCF

PSI4 interface: counterpart of PSI4 keyword REFERENCE (counterpart values: RHF, UHF, ROHF).

- Type: string

NWCHEM_SCF_NOPEN

PSI4 interface: counterpart of PSI4 keyword MULTIPLICITY.

- Type: integer

NWCHEM_SCF_SYM

PSI4 interface: current specification of the geometry is the symmetry detected by PSI4 to prevent reorientation.

- Type: string
- Possible Values: ON, OFF

NWCHEM_SCF_ADAPT

- Type: string

- Possible Values: ON, OFF

NWCHEM_SCF_TOL2E

- Type: double

NWCHEM_SCF_VECTORS

- Type: array

NWCHEM_SCF_THRESH

PSI4 interface: counterpart of PSI4 keyword E_CONVERGENCE and D_CONVERGENCE.

- Type: double

NWCHEM_SCF_MAXITER

PSI4 interface: counterpart of PSI4 keyword MAXITER.

- Type: integer

NWCHEM_SCF_PROFILE

- Type: string
- Possible Values: TRUE, FALSE

NWCHEM_SCF_DIIS

- Type: string
- Possible Values: TRUE, FALSE

NWCHEM_SCF_DIRECT

- Type: string
- Possible Values: TRUE, FALSE

NWCHEM_SCF_SEMIDIRECT

- Type: array

NWCHEM_SCF_NR

- Type: double

NWCHEM_SCF_LEVEL

- Type: array

NWCHEM_SCF_PRINT

- Type: array

NWCHEM_SCF_NOPRINT

- Type: array

3) DFT Keywords

NWCHEM_DFT

PSI4 interface: counterpart of reference (counterpart values: RKS, UKS). To perform RODFT calculation using PSI4 keyword, set ‘reference RKS’ and multiplicity as usual. If molecule is not singlet but the reference is RKS, interface recognizes it as NWChem RODFT calculation. Keyword NWCHEM_DFT_CGMIN is necessary for RODFT so the keyword is automatically set.

- Type: string
- Possible values: RODFT, ODFT

NWCHEM_DFT_VECTORS

- Type: array

NWCHEM_DFT_MAX_OVL

- Type: string
- Possible values: TRUE, FALSE

NWCHEM_DFT_XC

PSI4 interface: Check the map of available PSI4 DFT functionals.

- Type: array

NWCHEM_DFT_ITERATIONS

PSI4 interface: counterpart of PSI4 keyword MAXITER.

- Type: integer

NWCHEM_DFT_CONVERGENCE

PSI4 interface: counterpart of PSI4 keywords E_CONVERGENCE and D_CONVERGENCE.

- Type: array

NWCHEM_DFT_GRID

PSI4 interface: counterpart of PSI4 keywords DFT_RADIAL_POINTS and DFT_SPHERICAL_POINTS.

- Type: array

NWCHEM_DFT_DISP

PSI4 interface: this keyword can be part of counterpart of DFT_FUNCTIONAL in PSI4.

- Type: array

NWCHEM_DFT_DIRECT

- Type: string
- Possible Values: TRUE, FALSE

NWCHEM_DFT_SEMIDIRECT

- Type: array

NWCHEM_DFT_MULT

PSI4 interface: Keyword set from active molecule.

- Type: integer

NWCHEM_DFT_SMEAR

- Type: double

NWCHEM_DFT_CGMIN

- Type: string
- Possible Values: TRUE, FALSE

NWCHEM_DFT_MULLIKEN

- Type: string
- Possible Values: TRUE, FALSE

NWCHEM_DFT_FUKUI

- Type: string
- Possible Values: TRUE, FALSE

NWCHEM_DFT_PRINT

- Type: array

NWCHEM_DFT_NOPRINT

- Type: array

4) MP2 Keywords

NWCHEM_MP2_FREEZE

- Type: array

NWCHEM_MP2_TIGHT

- Type: string
- Possible Values: TRUE, FALSE

NWCHEM_MP2_SCS

PSI4 interface: NWCHEM_MP2_SCS, NWCHEM_MP2_FSS and NWCHEM_MP2_FOS

keywords must set in order.

- Type: string
- Possible Values: TRUE, FALSE

NWCHEM_MP2_FSS

PSI4 interface: NWCHEM_MP2_SCS, NWCHEM_MP2_FSS and NWCHEM_MP2_FOS

keywords must set in order.

- Type: double

NWCHEM_MP2_FOS

PSI4 interface: NWCHEM_MP2_SCS, NWCHEM_MP2_FSS and NWCHEM_MP2_FOS

keywords must set in order.

- Type: double

5) CCSD Keywords

NWCHEM_CCSD_THRESH

- Type: double

NWCHEM_CCSD_MAXITER

- Type: integer

6) TCE (Tensor contraction engine) keyword: CI, MBPT, and CC

NWCHEM_TCE_DFT

PSI4 interface: To control options of the DFT modules, use DFT keywords.

- Type: string
- Possible Values: TRUE, FALSE

NWCHEM_TCE

PSI4 interface: This option is to turn ON/OFF the TCE module. For CCSD and CCSD(T), default is OFF. For others, default is ON. **NWChem interface:** This is a different keyword from the tce block in NWChem.

- Type: string
- Possible Values: TRUE, FALSE

NWCHEM_TCE_MODULE

PSI4 interface: Currently available TCE modules are limited. Any TCE module in NWChem is available but results may not be harvested properly if the model is not listed in the possible values below. **NWChem interface:** Keyword ‘module’ does not exist in NWChem. This is the same as specifying the tce theory inside the tce block.

- Type: string
- Possible Values: CCSD, CCSDT, CCSDTQ, CCSD(T), CCSDT(Q)

NWCHEM_TCE_THRESH

- Type: double

NWCHEM_TCE_MAXITER

- Type: integer

NWCHEM_TCE_IO

- Type: string
- Possible values: fortran, eaf, ga, sf, replicated, dra, ga_eaf

NWCHEM_TCE_DIIS

- Type: integer

NWCHEM_TCE_FREEZE

- Type: array

NWCHEM_TCE_NROOTS

- Type: integer

NWCHEM_TCE_TARGET

- Type: integer

NWCHEM_TCE_TARGETSYM

- Type: string

NWCHEM_TCE_2EORB

- Type: string
- Possible Values: TRUE, FALSE

NWCHEM_TCE_DIPOLE

- Type: string
- Possible Values: TRUE, FALSE

7) TDDFT Keywords

NWCHEM_TDDFT

- Type: string
- Possible Values: RPA, CIS

NWCHEM_TDDFT_NROOTS

- Type: integer

NWCHEM_TDDFT_TARGET

- Type: integer

NWCHEM_TDDFT_THRESH

- Type: double

NWCHEM_TDDFT_MAXITER

- Type: integer

NWCHEM_TDDFT_CIVECS

- Type: string
- Possible Values: TRUE, FALSE

NWCHEM_TDDFT_NOTRIPLET

- Type: string
- Possible Values: TRUE, FALSE

8) TASK keywords

The task keyword is NOT recommended to use. Rather use the method argument (such as nwc-scf, nwc-dft, etc.). If specified, however, the method MUST be ‘nwchem’. The type for all keywords listed in this section is string and the possible values are energy, gradient, and optimize.

NWCHEM_TASK_SCF

NWCHEM_TASK_DFT

NWCHEM_TASK_MP2

NWCHEM_TASK_DIRECT_MP2

NWCHEM_TASK_RIMP2

NWCHEM_TASK_CCSD

NWCHEM_TASK_CCSD(T)

NWCHEM_TASK_TCE

NWCHEM_TASK_TDDFT

CHAPTER 7. CONCLUSION

Chapters 2 and 3 present density functional theory (DFT) studies on the site preference of S adsorbate on different facets of Cu nanoclusters. Chapter 2 specifically describes the size dependence of the S adsorption energy on up to ~300 atoms of Cu(111) clusters with analysis of molecular orbitals (MOs), site projected density of states (SDOS), and crystal orbital Hamiltonian population (COHP). Gaussian basis set calculations were performed using the NWChem and GAMESS codes and plane wave basis set calculations were through VASP. A great agreement between Gaussian and plane-wave basis set energy results were achieved.

The S binding energies on different sizes of Cu(111) clusters was calculated using different DFT functionals in Chapter 2. Compared to other clusters, Cu₂₀, considered to be a magic number, has a larger HOMO-LUMO gap, which can be correlated to the weaker binding energy with S. Also, the binding energy has strong variation in adsorbed sites. The hcp sites at the edge, which were found to have more concentrated molecular orbital density, are preferred over the fcc sites.

Also, the strong oscillatory behavior of S adsorption energies reflects quantum size effects (QSE) and is consistent with SDOS and COHP plots which show clear bonding interactions below the Fermi-level and antibonding close to the Fermi-level. Generally, the discrete energy level of small clusters, considered to be a significant factor in the strong size dependence of chemisorption, was not applied for the system in Chapter 2. However, S adsorption is not favorable on the closed-shell cluster and the energy varies at different sites.

In Chapter 3, comparison between three-fold-hollow (3fh) and four-fold-hollow (4fh) sites are discussed. The results in the Chapter also achieved a great agreement between

Gaussian and plane wave basis sets and found a similar size dependence of Cu(100) with relatively small clusters. The site preference of S on extended Cu surfaces were described by averaging results for clusters over suitable ranges of size. To consider randomization for medium size clusters, the energies with smearing was also reported. As a result, it is found that S binds ~ 0.6 eV stronger at 4fh sites than 3fh sites. This site preference is supported by the SDOS plots showing that 3fh and 4fh sites have very similar bonding interactions while the antibonding interaction at 4fh sites is weaker than 3fh.

Chapter 4 discusses the formation of AuX_2 ($\text{X}=\text{S}, \text{Cl}, \text{CH}_3\text{S}, \text{SiH}_3\text{S}$) complexes on Au(111) surface. This study was motivated by the Scanning Tunneling Microscopy (STM) observations; AuS_2 is not found on the Au(111) surface, while AuCl_2 is found sometimes at a high coverage of Cl and $\text{Au}(\text{CH}_3\text{S})_2$ is found even at low coverage. To explain why AuS_2 is not observed, the stability of AuX_2 complexes and those on the surface were calculated using DFT with different basis sets, Gaussian and plane wave, respectively. For the gas-phase, both DFT and benchmarked binding energies of Au-X are also presented.

The results of the gas-phase AuX_2 investigation show that the stability of the complexes are very similar energetically regardless of the ligand X. On the other hand, plane wave results show that the stability of the adsorbed complexes on the surface is different from that of chemisorbed X; AuS_2 is less stable than chemisorbed S, AuCl_2 is more or less stable depending on the DFT functional used, and $\text{Au}(\text{CH}_3\text{S})_2$ and $\text{Au}(\text{SiH}_3\text{S})_2$ are more stable. For AuCl_2 , PBE failed to approximate the consistent results with experimental observations but optB88-vdW and revTPSS succeeded.

Although the bond strength of Au-X of the gas-phase complexes is similar, S has stronger binding to Au than other ligands, which helps chemisorbed S to be stable on the

surface. From this observation, one can insist that the similarity of the gas phase stability and larger variation of AuX_2 stability on the surface support the hypothesis that the AuX_2 stability is more related to the ligand adsorption on the surface. In other words, the strength of the ligand to the surface is more significant in determining the formation of the complex on the surface.

In Chapter 5, we specifically focused on the complex M_3S_3 ($\text{M}=\text{Ni}, \text{Cu}, \text{Ag}, \text{Au}$) identified on fcc $\text{M}(111)$ surfaces by STM. To study the stability of adsorbed M_3S_3 complexes, Chapter 5 provides comprehensive energetics of the gas-phase and adsorbed complexes on surfaces and interprets the results within the frame of Hess's law. Hess's law was used to elucidate the energetic contributions in the process of forming complexes on the surface by decomposing an overall reaction into several steps.

The results show that all M_3S_3 complexes are stable on the terrace while the only formation of Ag_3S_3 is found to be spontaneous on the terrace. The complex is formed by extracting Ag from kink sites along the step edges and from excess S on the terraces. Within this context, actual experimental observations are also discussed and successfully explained using the theoretically computed energetics as to why the M_3S_3 complex can be observed under the actual experimental conditions.

Chapter 6 introduces a different topic from the previous Chapters; developing a program called the quantum chemistry common driver and databases (QCDB). The Chapter describes the overall concepts of the program and a strategy for development, but specifically focuses on the detail of the built-in NWChem interface. The NWChem interface is successfully built in a driver existing in PSI4 using the Python language. The interface provides a more flexible input format (both PSI4 and NWChem-speak can be used), sharing

capabilities between two programs and data communication through the common dictionary of PSI4.

PSI4 currently has the built-in CFOUR and NWChem interfaces, and the driver portion of PSI4 is pulled out by one of our collaborators, Lori Burns. One of the future works is to add interfaces of other programs (such as GAMESS), and further develop each interface, adding more functionalities and keywords as described in the Conclusion of Chapter 6. A more developed QCDB will allow users of all quantum chemistry programs to drive multiple codes that they want to use with one common input and obtain data printed on one common output.